



International Committee for Future Accelerators

Sponsored by the Particles and Fields Commission of IUPAP

Beam Dynamics Newsletter

No. 42

**Issue Editor:
Y. Cai**

**Editor in Chief:
W. Chou**

April 2007

Contents

1	FOREWORD	6
1.1	FROM THE CHAIRMAN.....	6
1.2	FROM THE EDITOR.....	6
2	INTERNATIONAL LINEAR COLLIDER (ILC).....	7
2.1	ILC REFERENCE DESIGN REPORT – ACCELERATOR EXECUTIVE SUMMARY.....	7
2.1.1	Superconducting RF.....	9
2.1.2	The ILC Baseline Design.....	11
2.1.2.1	<i>Beam Parameters</i>	12
2.1.2.2	<i>Electron Source</i>	14
2.1.2.3	<i>Positron Source</i>	15
2.1.2.4	<i>Damping Rings</i>	17
2.1.2.5	<i>Ring to Main Linac (RTML)</i>	18
2.1.2.6	<i>Main Linacs</i>	19
2.1.2.7	<i>Beam Delivery System</i>	22
2.1.3	Sample Sites.....	23
2.1.4	Value Estimate.....	26
2.1.5	R&D and the Engineering Design Phase.....	27
2.1.6	References.....	28
2.2	SECOND INTERNATIONAL ACCELERATOR SCHOOL FOR LINEAR COLLIDERS.....	29
2.2.1	Committees.....	30
2.2.2	Lecturers.....	30
2.2.3	Curriculum.....	31
2.2.4	Program.....	32
3	FREE-ELECTRON LASER.....	34
3.1	BEAM DYNAMICS AT FLASH AND THE EUROPEAN XFEL.....	34
3.1.1	Introduction.....	34
3.1.2	Bunch Compression and Start-to-End Simulations.....	36
3.1.3	Measurements and Simulation of Beam Slice Properties.....	39
3.1.4	Simulations of Micro-Bunching Instability and Possible Measurements.....	42
3.1.5	References.....	45
3.2	FREE ELECTRON LASER R&D AT THE NSLS SDL.....	46
3.2.1	Introduction.....	46
3.2.2	The NSLS Source Development Laboratory (SDL).....	46

3.2.3	Recent SDL FEL Experiments.....	47
3.2.3.1	<i>Laser Seeded FEL Amplifier and Femto-second FEL Pulse Evolution in the Superradiance Regime</i>	48
3.2.3.2	<i>Laser Seeded FEL - 4th harmonic HGHG and ESASE</i>	49
3.2.3.3	<i>FEL Light for Chemical Dynamics</i>	49
3.2.4	Future FEL R&D at the NSLS SDL.....	50
3.2.5	Acknowledgement.....	50
3.3	FEL DESIGN STUDIES AT LBNL: ACTIVITIES AND PLANS.....	51
3.3.1	Introduction.....	51
3.3.2	A High Repetition Rate FEL Facility.....	52
3.3.3	Current R&D Activities.....	53
3.3.3.1	<i>VHF Photo-gun</i>	53
3.3.3.2	<i>Photocathode Design</i>	54
3.3.3.3	<i>Electron Beam Delivery Systems</i>	54
3.3.3.4	<i>FEL Design</i>	55
3.3.3.5	<i>Timing and Synchronization Systems</i>	56
3.3.4	LBNL Support for the FERMI@Elettra Project.....	57
3.3.5	References.....	57
3.4	FERMI@ELETTRA.....	58
3.4.1	Introduction.....	58
3.4.2	Overall Layout.....	59
3.4.3	Linear Accelerator and FEL's.....	60
3.4.3.1	<i>The Photo-Injector</i>	60
3.4.3.2	<i>Main Linac and Beam Transport</i>	60
3.4.4	Photon Production.....	61
3.4.4.1	<i>Principle of Operation</i>	61
3.4.4.2	<i>Undulators and Beamlines</i>	62
3.4.5	Design Studies.....	62
3.4.6	Status.....	64
3.4.7	References.....	64
4	SINGLE-PARTICLE BEAM DYNAMICS.....	65
4.1	COMPUTATION OF TRANSFER MAPS FROM MAGNETIC FIELD DATA IN WIGGLERS AND UNDULATORS.....	65
4.1.1	Introduction.....	65
4.1.2	Transfer Maps.....	66
4.1.3	Fitting the Wiggler Field.....	66
4.1.4	Benchmarks.....	68
4.1.5	Smoothing.....	69
4.1.6	Generalization to Other Domains.....	69
4.1.7	References.....	70
4.1.8	Figures.....	70
4.2	STORAGE RING OPTICS MEASUREMENT, MODEL, AND CORRECTION.....	71
4.2.1	Introduction.....	71
4.2.2	Geometric and Chromatic Orbit Measurement with a Model-Independent Analysis... 4.2.2.1 <i>Geometric Orbit Measurement</i> 4.2.2.2 <i>Chromatic Orbit Measurement</i> 4.2.2.3 <i>Response Quantities</i> 4.2.2.4 <i>Phase Advances</i>	73 73 74 74 75

4.2.2.5	<i>Linear Green's Functions</i>	75
4.2.2.6	<i>Coupling Ellipses</i>	76
4.2.2.7	<i>Dispersions</i>	77
4.2.3	SVD-Enhanced Least-Squares Fitting.....	77
4.2.4	Application for PEP-II Measurements.....	78
4.2.5	Application to PEP-II Optics Improvement - Examples.....	81
4.2.5.1	<i>Beta Beat Fix</i>	81
4.2.5.2	<i>Dispersion Beat Fix</i>	82
4.2.5.3	<i>Dramatic Change of Machine Working Tunes</i>	83
4.2.5.4	<i>Optics Fix after Major Orbit Steering</i>	83
4.2.5.5	<i>Virtual Emittance and Virtual Luminosity</i>	84
4.2.6	Conclusions.....	87
4.2.7	Acknowledgement.....	87
4.2.8	References.....	87
5	RECENT DOCTORIAL THESES.....	88
5.1	EMITTANCE EVOLUTION PROCESS IN HIGH BRIGHTNESS PHOTO-CATHODE RF GUN WITH FOCUSING SOLENOIDS.....	88
5.2	STUDY ON THE LATTICE AND BEAM COLLECTIVE EFFECTS OF HIGH ENERGY ELECTRON STORAGE RING.....	89
5.2.1	Introduction.....	89
5.2.2	On BEPCII Lattice.....	89
5.2.3	On ILC Damping Ring Alternative Lattice.....	90
5.2.4	Beam Collective Effects.....	92
5.2.5	References.....	93
6	FORTHCOMING BEAM DYNAMICS EVENTS.....	94
6.1	INTERNATIONAL EUROPHYSICS CONFERENCE ON HIGH ENERGY PHYSICS (HEP 2007).....	94
6.2	LARP MINI-WORKSHOP ON BEAM-BEAM COMPENSATION 2007.....	95
6.3	LOW LEVEL RADIO FREQUENCY WORKSHOP (LLRF 2007).....	95
6.3.1	Announcement.....	95
7	ANNOUNCEMENTS OF THE BEAM DYNAMICS PANEL.....	96
7.1	ICFA BEAM DYNAMICS NEWSLETTER.....	96
7.1.1	Aim of the Newsletter.....	96
7.1.2	Categories of Articles.....	96
7.1.3	How to Prepare a Manuscript.....	96
7.1.4	Distribution.....	97
7.1.5	Regular Correspondents.....	97
7.2	ICFA BEAM DYNAMICS PANEL MEMBERS.....	99

1 Foreword

1.1 From the Chairman

Weiren Chou, Fermilab
Mail to: chou@fnal.gov

A joint ICFA – Laboratory Directors meeting was held at the Institute of High Energy Physics (IHEP) in Beijing, China from February 8 to 9, 2007. The first half-day was a joint meeting with the ILCSC for discussions on the ILC Reference Design Report (RDR) and costing. Barry Barish, Director of the GDE, gave a detailed report. The estimated cost of the ILC is 6.7 billion U.S. dollars plus 13,000 person-years. (The currency exchange rate assumed in the cost estimate was: 1 U.S. dollar = 117 Japanese Yen = 0.83 Euro.) ICFA approved the release of the RDR and costing. Both were announced at a press conference at noontime February 8. This is an important milestone on the ILC roadmap. The next phase is to finish a construction-ready Engineering Design Report (EDR) in about 3 years. The plan is to divide the work into tens of work packages, which will be distributed to various institutions around the world and coordinated by a Project Manager.

The ICFA meeting also heard a number of reports from the ICFA Chair, C11 Chair, InterAction team, ICFA panel chairs and a dozen laboratory directors. The meeting minutes can be found on the web at: <http://www.fnal.gov/directorate/icfa/meetings.html>

There was a discussion at the meeting on Open Access (OA) publishing. At this time OA has mostly been European-driven, with CERN a main proponent of this initiative. It was noted that making the transition to OA is an unresolved question. There will be an ICFA position paper prepared for discussion at the next ICFA meeting.

The meeting also approved the 41st ICFA Advanced Beam Dynamics Workshop *ERL07*, which will take place May 21 - 25, 2007 at Daresbury Laboratory, U.K. (<http://www.erl07.dl.ac.uk/>)

The Second International Accelerator School for Linear Colliders, which is a continuation of the first school held last year in Japan, will take place at the Ettore Majorana Center, Erice (Sicily), Italy from October 1 – 10, 2007. The school web site is: <http://www.linearcollider.org/school/2007/>. Readers are referred to Section 2 of this newsletter for the present status of the school.

The editor of this issue is Dr. Yunhai Cai, a panel member and a scientist from SLAC. I'd like to express my sincere gratitude to him for having collected a number of nicely written articles and having produced a well-organized, fine Newsletter.

1.2 From the Editor

Yunhai Cai, SLAC,
2575 Sand Hill Road, Menlo Park, CA 94025, USA
Mail to: yunhai@slac.stanford.edu

The Global Design Effort released the ILC Reference Design Report (RDR) in Beijing, China, February 2007. This reached another extremely important milestone since the recommendations from the International Technology Recommendation Panel

more than two year ago. In this issue, we have the opportunity to publish the executive summary of the accelerator in the RDR. I would like to thank Nan Phinney, Tor Raubenheimer, Nick Walker, and Barry Barish for the earlier release of the document.

As the first sight of an electron beam has just been seen from the LCLS injector, we dedicate this issue to the subject of Free-Electron Lasers (FEL). Several articles range from summaries of recent achievements, reviews of important beam dynamics problems, and visions of future directions. The article by Decking and Limberg highlights the most recent comparisons between measurement and simulation at FLASH facility at DESY. The article by Corlett and his collaborators at LBNL outlines a vision of a high repetition rate FEL facility that could be operated in a large range of parameters.

Finally, in the beam dynamics section, we have two nicely written articles of how to integrate a charged particle through three-dimensional magnetic devices like wigglers and how to construct a precision model of circular accelerators.

Lastly, I would like to thank Sharon West who did a professional job of editing and formatting this issue and created a general template for our Beam Dynamics Newsletter in its future publications.

2 International Linear Collider (ILC)

2.1 ILC Reference Design Report – Accelerator Executive Summary

Nan Phinney, SLAC
Editor on behalf of the ILC Global Design Effort
Mail to: nan@slac.stanford.edu

The International Linear Collider (ILC) is a 200-500 GeV center-of-mass high-luminosity linear electron-positron collider, based on 1.3 GHz superconducting radio-frequency (SCRF) accelerating cavities. The use of the SCRF technology was recommended by the International Technology Recommendation Panel (ITRP) in August 2004 [1], and shortly thereafter endorsed by the International Committee for Future Accelerators (ICFA). In an unprecedented milestone in high-energy physics, the many institutes around the world involved in linear collider R&D united in a common effort to produce a global design for the ILC. In November 2004, the 1st International Linear Collider Workshop was held at KEK, Tsukuba, Japan. The workshop was attended by some 200 accelerator physicists from around the world, and paved the way for the 2nd ILC Workshop in August 2005, held at Snowmass, Colorado, USA, where the ILC Global Design Effort (GDE) was officially formed. The GDE membership reflects the global nature of the collaboration, with accelerator experts from all three regions (Americas, Asia and Europe). The first major goal of the GDE was to define the basic parameters and layout of the machine – the Baseline Configuration. This was achieved at the first GDE meeting held at INFN, Frascati, Italy in December 2005 with the creation of the Baseline Configuration Document (BCD). During the next 14 months, the BCD was used as the basis for the detailed design work and value estimate (as described in section 1.6) culminating in the completion of the second major milestone, the publication of the draft ILC Reference Design Report (RDR).

The technical design and cost estimate for the ILC is based on two decades of world-wide Linear Collider R&D, beginning with the construction and operation of the SLAC Linear Collider (SLC). The SLC is acknowledged as a proof-of-principle machine for the linear collider concept. The ILC SCRF linac technology was pioneered by the TESLA collaboration*, culminating in a proposal for a 500 GeV center-of-mass linear collider in 2001 [2]. The concurrent (competing) design work on a normal conducting collider (NLC with X-band [3] and GLC with X- or C-Band [4]), has advanced the design concepts for the ILC injectors, Damping Rings (DR) and Beam Delivery System (BDS), as well as addressing overall operations, machine protection and availability issues. The X- and C-band R&D has led to concepts for the RF power source that may eventually produce either cost and/or performance benefits. Finally, the European XFEL [5] to be constructed at DESY, Hamburg, Germany, will make use of the TESLA linac technology, and represents a significant on-going R&D effort which remains of great benefit for the ILC.

The current ILC baseline assumes an accelerating gradient of 31.5 MV/m to achieve a centre-of-mass energy of 500 GeV. The high luminosity requires the use of high power and small emittance beams. The choice of 1.3 GHz SCRF is well suited to the requirements, primarily because the very low power loss in the SCRF cavity walls allows the use of long RF pulses, relaxing the requirements on the peak-power generation, and ultimately leading to high wall-plug to beam transfer efficiency.

The primary cost drivers are the SCRF Main Linac technology and the Conventional Facilities (including civil engineering). The choice of gradient is a key cost and performance parameter, since it dictates the length of the linacs, while the cavity *quality factor* (Q_0) relates to the required cryogenic cooling power. The achievement of 31.5 MV/m as the baseline average operational accelerating gradient – requiring a minimum performance of 35 MV/m during cavity mass-production acceptance testing – represents the primary challenge to the global ILC R&D

With the completion of the RDR, the GDE will shortly begin an engineering design study, closely coupled with a prioritized R&D program. The goal is to produce an Engineering Design Report (EDR) demonstrating readiness for construction by 2010, followed by start of construction in 2012. A seven-year construction phase is currently assumed, allowing operations to begin in 2019. This is consistent with a technically driven schedule for this international project.



Figure 2.1: A TESLA nine-cell 1.3 GHz superconducting niobium cavity.

* Now known as the TESLA Technology Collaboration (TTC); see <http://tesla.desy.de>.

2.1.1 Superconducting RF

The primary cost driver for the ILC is the superconducting RF technology used for the Main Linacs, bunch compressors and injector linacs. In 1992, the TESLA Collaboration began R&D on 1.3 GHz technology with a goal of reducing the cost per MeV by a factor of 20 over the then state-of-the-art SCRF installation (CEBAF). This was achieved by increasing the operating accelerating gradient by a factor of five from ~ 5 MV/m to ~ 25 MV/m, and reducing the cost per meter of the complete accelerating module by a factor of four for large-scale production.

The TESLA cavity R&D was based on extensive existing experience from CEBAF (TJNAF), CERN, Cornell University, KEK, Saclay and Wuppertal. The basic element of the technology is a nine-cell 1.3 GHz niobium cavity, shown in Figure 2.1. Approximately 160 of these cavities have been fabricated by industry as part of the ongoing R&D program at DESY; some 17,000 will be needed for the ILC.

A single cavity is approximately 1 m long. The cavities must be operated at 2 K to achieve their performance. Eight cavities are mounted together in a *string* and assembled into a common low-temperature cryostat or *cryomodule* (Figure 2.2), the design of which is already in the third generation. Ten cryomodules have been produced to-date, five of which are currently installed in the in the VUV free-electron laser (FLASH)[†] at DESY, where they are routinely operated. DESY is currently preparing for the construction of the European XFEL facility, which will have a ~ 20 GeV superconducting linac containing 116 cryomodules.

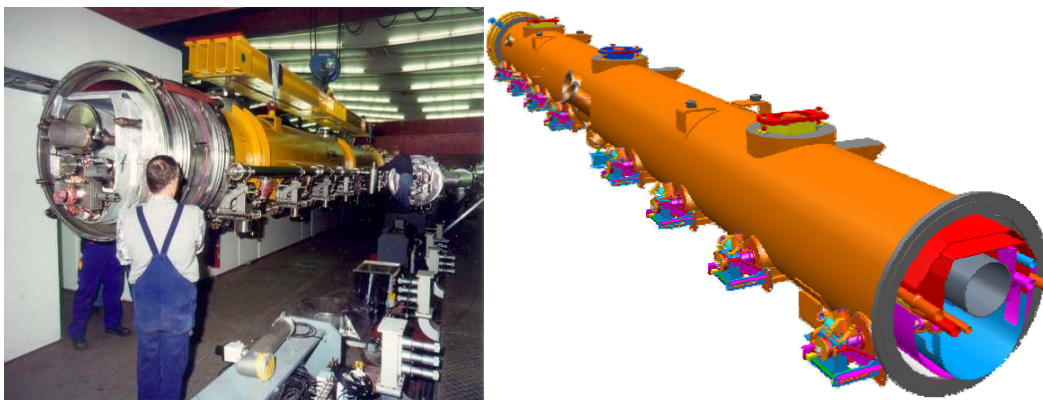


Figure 2.2: SCRF Cryomodules. Left: an 8 cavity TESLA cryomodule is installed into the FLASH linac at DESY. Right: design for the 4th generation ILC prototype cryomodule, due to be constructed at Fermilab National Laboratory.

The ILC community has set an aggressive goal of routinely achieving[‡] 35 MV/m in nine-cell cavities, with a minimum production yield of 80%. Several cavities have already achieved these and higher gradients (see Figure 2.3), demonstrating proof of principle. Records of over 50 MV/m have been achieved in single-cell cavities at KEK and Cornell [7]. However, achieving the desired production yield at the mass-production levels ($\sim 17,000$ cavities) required for nine-cell cavities remains a challenge.

[†] Originally known as the TESLA Test Facility (TTF).

[‡] Acceptance test.

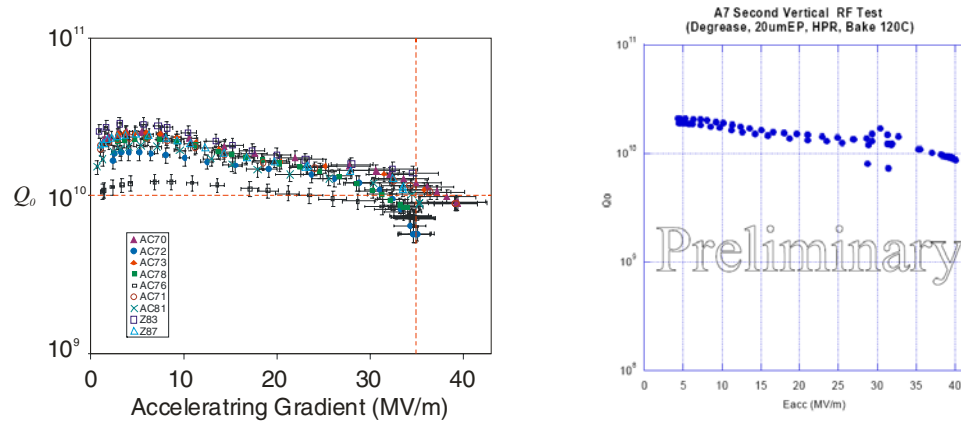


Figure 2.3: High-performance nine-cell cavities. Left: Examples of DESY nine-cell cavities achieving ≥ 35 MV/m. Right: Recent result from JLAB of nine-cell cavity achieving ~ 40 MV/m.



Figure 2.4: Clean room environments are mandatory. Left: the assembly of eight nine-cell TESLA cavities into a cryomodule string at DESY. Right: an ICHIRO nine-cell cavity is prepared for initial tests at the Superconducting RF Test Facility (STF) at KEK.

The key to high-gradient performance is the ultra-clean and defect-free inner surface of the cavity. Both cavity preparation and assembly into cavity strings for the cryomodules must be performed in clean-room environments (Figure 2.4). The best cavities have been achieved using *electropolishing*, a common industry practice which was first developed for use with superconducting cavities by CERN and KEK. Over the last few years, research at Cornell, DESY, KEK and TJNAF has led to an agreed standard procedure for cavity preparation, depicted in Figure 2.5. The focus of the R&D is now to optimize the process to guarantee the required yield. The ILC SCRF community has developed an internationally agreed-upon plan to address the priority issues.

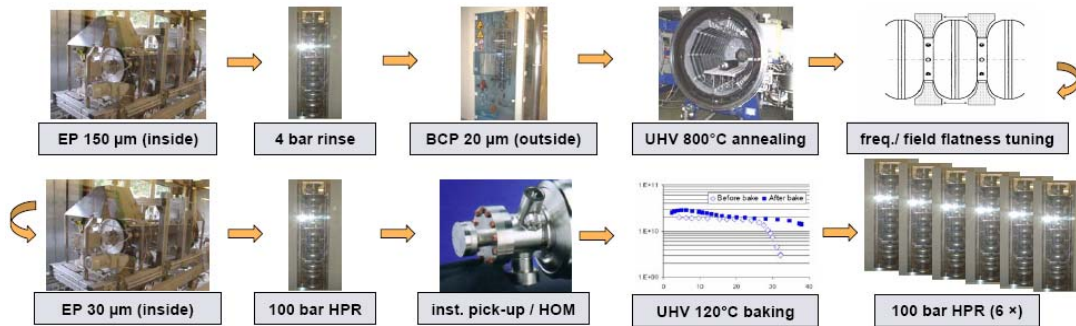


Figure 2.5: Birth of a nine-cell cavity: basic steps in surface treatment needed to achieve high-performance superconducting cavities.
(EP = electropolishing; HPR = high-pressure rinsing.)

The high-gradient SCRF R&D required for ILC is expected to ramp-up world-wide over the next years. The U.S. is currently investing in new infrastructure for nine-cell cavity preparation and string and cryomodule assembly. These efforts are centered at Fermilab (ILC Test Accelerator, or ILCTA), together with ANL, Cornell University, SLAC and TJNAF. In Japan, KEK continues to ramp up its Superconducting RF Test Facility (STF). In Europe, the focus of R&D at DESY has shifted to industrial preparation for construction of the XFEL. There is continued R&D to support the high-gradient program, as well as other critical ILC-related R&D such as high-power RF couplers (LAL, Orsay, France) and cavity tuners (CEA Saclay, France; INFN Milan, Italy).

The quest for high-gradient and affordable SCRF technology for high-energy physics has revolutionized accelerator applications. In addition to the European XFEL, many linac-based projects utilizing SCRF technology are being developed, including 4th-generation light sources such as single-pass FELs and energy-recovery linacs, and the Spallation Neutron Source (SNS) in Oak Ridge, Tennessee. For the large majority of new accelerator-based projects, SCRF has become the technology of choice.

2.1.2 The ILC Baseline Design

The overall system design has been chosen to realize the physics requirements with a maximum CM energy of 500 GeV and a peak luminosity of $2 \times 10^{34} \text{ cm}^{-2} \text{ s}^{-1}$. Figure 2.6 shows a schematic view of the overall layout of the ILC, indicating the location of the major sub-systems:

- A polarized electron source based on a photocathode DC gun.
- An undulator-based positron source, driven by a 150 GeV electron beam.
- 5 GeV electron and positron damping rings (DR) with a circumference of 6.7 km, housed in a common tunnel at the center of the ILC complex.
- Beam transport from the damping rings to the main linacs, followed by a two-stage bunch compressor system prior to injection into the main linac.
- Two 11 km long main linacs, utilizing 1.3 GHz SCRF cavities, operating at an average gradient of 31.5 MV/m, with an RF pulse length of 1.6 ms.

- A 4.5 km long Beam Delivery System (BDS), which brings the two beams into collision with a 14 mrad crossing angle, at a single interaction point which can be shared by two detectors.

The total foot-print is ~ 31 km. The electron source, the damping rings, and the positron auxiliary ('keep-alive') source are centrally located around the interaction region (IR). The plane of the damping rings is elevated by ~ 10 m above that of the BDS to avoid interference.

To upgrade the machine to $E_{cms}=1$ TeV, the linacs and the beam transport lines from the damping rings would be extended by another ~ 11 km each. Certain components in the beam delivery system would also need to be replaced.

2.1.2.1 Beam Parameters

The nominal beam parameter set in Table 2.1, corresponding to the design luminosity of $2 \times 10^{34} \text{ cm}^{-2} \text{ s}^{-1}$ at $E_{cms} = 500$ GeV, has been chosen to meet known accelerator physics and technology challenges throughout the whole accelerator complex. Examples of such challenges are:

- beam instability and kicker hardware constraints in the damping rings;
- beam current, beam power, and pulse length limitations in the main linacs;
- emittance preservation requirements, in the main linacs and the beam delivery system;
- background control and kink instability issues in the interaction region.

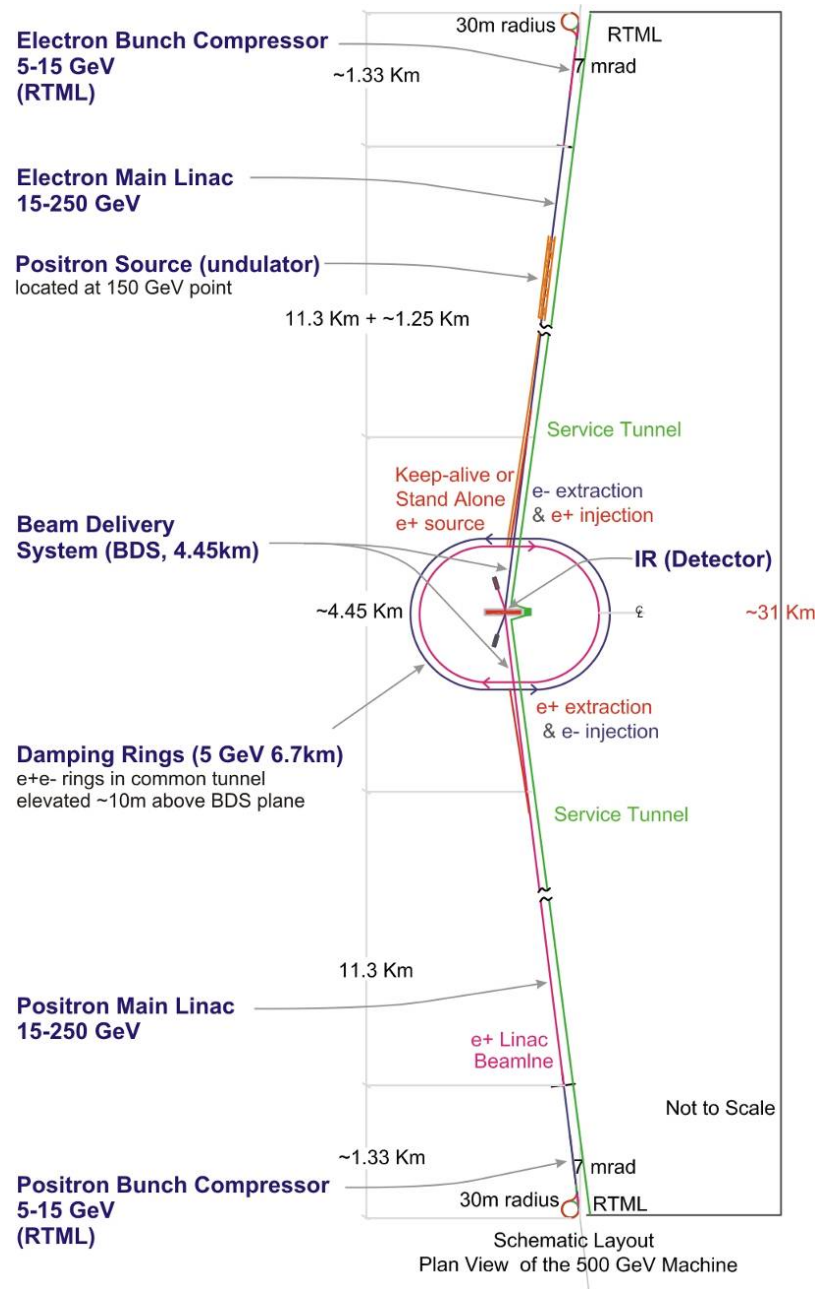


Figure 2.6: Schematic layout of the ILC complex for 500 GeV CM

Nearly all high-energy physics accelerators have shown unanticipated difficulties in reaching their design luminosity. The ILC design specifies that each subsystem support a range of beam parameters. The resulting flexibility in operating parameters will allow identified problems in one area to be compensated for in another. The nominal IP beam parameters and design ranges are presented in Table 2.2.

Table 2-1: Basic design parameters for the ILC

Center-of-mass energy range	200–500	GeV
Peak luminosity ¹	2×10^{34}	$\text{cm}^{-2} \text{s}^{-1}$
Beam current	9.0	mA
Pulse rate	5.0	Hz
Pulse length (beam)	~1	ms
Accelerating gradient ^a	31.5	MV/m
RF pulse length	1.6	ms
Beam power (per beam) ^a	10.8	MW
Total AC Power consumption ^a	230	MW

a) at 500 GeV center-of-mass energy

Table 2.2: Nominal and design range of beam parameters at the IP. The min. and max. columns do not represent consistent sets of parameters, but only indicate the span of the design range for each parameter. (Nominal vertical emittance assumes a 100% emittance dilution budget from the damping ring to the IP.)

	<i>min.</i>	<i>nominal</i>	<i>max.</i>	
Bunch population	1	2	2	$\times 10^{10}$
Number of bunches	1260	2670	5340	
Linac bunch interval	180	369	500	ns
RMS bunch length at IP	200	300	500	μm
Normalized horizontal emittance at IP	10	10	12	mm-mrad
Normalized vertical emittance at IP	0.02	0.04	0.08	mm-mrad
Horizontal beta function at IP	10	20	20	mm
Vertical beta function at IP	0.2	0.4	0.6	mm
RMS horizontal beam size at IP	474	640	640	nm
RMS vertical beam size at IP	3.5	5.7	9.9	nm
Vertical disruption parameter	14	19.4	26.1	
Fractional RMS energy loss to beamstrahlung	1.7	2.4	5.5	%

2.1.2.2 *Electron Source*

Functional requirements

The ILC polarized electron source must:

- generate the required bunch train of polarized electrons (>80% polarization)
- capture and accelerate the beam to 5 GeV;
- transport the beam to the electron damping ring with minimal beam loss, and perform an energy compression and spin rotation prior to injection.

System Description

The polarized electron source is located on the positron linac side of the damping rings. The beam is produced by a laser illuminating a photocathode in a DC gun. Two independent laser and gun systems provide redundancy. Normal-conducting structures are used for bunching and pre-acceleration to 76 MeV, after which the beam is accelerated to 5 GeV in a superconducting linac. Before injection into the damping ring, superconducting solenoids rotate the spin vector into the vertical, and a separate superconducting RF structure is used for energy compression. The layout of the polarized electron source is shown in Figure 2.7.

Challenges

The SLC polarized electron source already meets the requirements for polarization, charge and lifetime. The primary challenge for the ILC electron source is the ~ 1 ms long bunch train, which demands a laser system beyond that used at any existing accelerator.

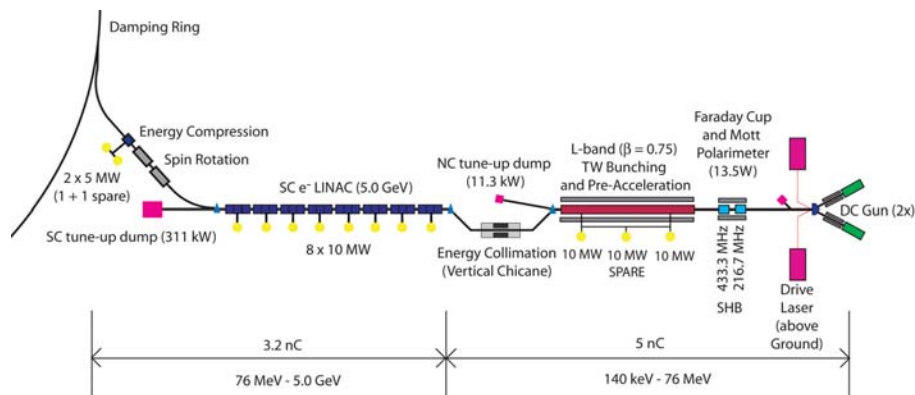


Figure 2.7: Schematic View of the Polarized Electron Source

2.1.2.3 Positron Source

Functional requirements

The positron source must perform several critical functions:

- generate a high-power multi-MeV photon production drive beam in a suitably short-period, high K -value helical undulator;
- produce the needed positron bunches in a metal target that can reliably deal with the beam power and induced radioactivity;
- capture and accelerate the beam to 5 GeV;
- transport the beam to the positron damping ring with minimal beam loss, and perform an energy compression and spin rotation prior to injection.

System Description

The major elements of the ILC positron source are shown in Figure 2.8. The source uses photoproduction to generate positrons. After acceleration to 150 GeV, the electron beam is diverted into an offset beamline, transported through a 150-meter helical undulator, and returned to the electron linac. The high-energy (~ 10 MeV) photons from the undulator are directed onto a rotating 0.4 radiation-length Ti-alloy target ~ 500 meters downstream, producing a beam of electron and positron pairs. This beam is then matched using an optical-matching device into a normal conducting (NC) L-band RF and solenoidal-focusing capture system and accelerated to 125 MeV. The electrons and remaining photons are separated from the positrons and dumped. The positrons are accelerated to 400 MeV in a NC L-band linac with solenoidal focusing. The beam is transported ~ 5 km through the rest of the electron main linac tunnel, brought to the central injector complex, and accelerated to 5 GeV using superconducting L-band RF. Before injection into the damping ring, superconducting solenoids rotate the spin vector into the vertical, and a separate superconducting RF structure is used for energy compression.

The baseline design is for unpolarized positrons, although the beam has a polarization of 30%, and beamline space has been reserved for an eventual upgrade to 60% polarization.

To allow commissioning and tuning of the positron systems while the high-energy electron beam is not available, a low-intensity auxiliary (or “keep-alive”) positron source is provided. This is a conventional positron source, which uses a 500 MeV electron beam impinging on a heavy-metal target to produce $\sim 10\%$ of the nominal positron beam. The keep-alive and primary sources use the same linac to accelerate from 400 MeV to 5 GeV.

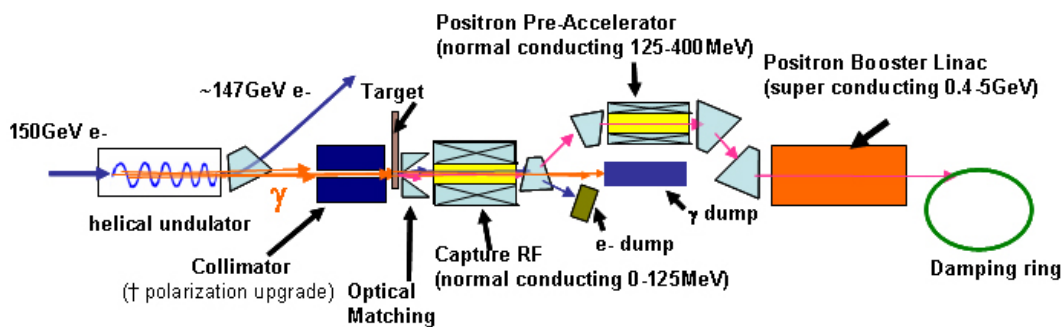


Figure 2.8: Overall Layout of the Positron Source.

The most challenging elements of the positron source are:

- the 150 m long superconducting helical undulator, which has a period of 1.15 cm and a K -value of 0.92, and a 6 mm inner diameter vacuum chamber;
- the Ti-alloy target, which is a cylindrical wheel 1.4 cm thick and 1 m in diameter, which must rotate at 100 m/s in vacuum to limit damage by the photon beam;
- the normal-conducting RF system which captures the positron beam, which must sustain high accelerator gradients during millisecond-long pulses in a strong magnetic field, while providing adequate cooling in spite of high RF and particle-loss heating.

The target and capture sections are also high-radiation areas which present remote handling challenges.

2.1.2.4 *Damping Rings*

Functional requirements

The damping rings must perform four critical functions:

- accept e^- and e^+ beams with large transverse and longitudinal emittances and damp to the low emittance beam required for luminosity production (by five orders of magnitude for the positron vertical emittance), within the 200 ms between machine pulses.
- inject and extract individual bunches without affecting the emittance or stability of the remaining stored bunches;
- damp incoming beam jitter (transverse and longitudinal) and provide highly stable beams for downstream systems;
- delay bunches from the source to allow feed-forward systems to compensate for pulse-to-pulse variations in parameters such as the bunch charge.

System Description

The ILC damping rings include one electron and one positron ring, each 6.7 km long, operating at a beam energy of 5 GeV. The two rings are housed in a single tunnel near the center of the site, with one ring positioned directly above the other. The plane of the DR tunnel is located ~10 m higher than that of the beam delivery system. This elevation difference gives adequate shielding to allow operation of the injector system while other systems are open to human access.

The damping ring lattice is divided into six arcs and six straight sections. The arcs are composed of TME cells; the straight sections use a FODO lattice. Four of the straight sections contain the RF systems and the superconducting wigglers. The remaining two sections are used for beam injection and extraction. Except for the wigglers, all of the magnets in the ring, are normal-conducting. Approximately 200 m of superferric wigglers are used in each damping ring. The wigglers are 2.5 m long devices, operating at 4.5K, with a peak field of 1.67 T.

The superconducting RF system is operated CW at 650 MHz, and provides 24 MV. The frequency is chosen to be half the linac RF frequency to easily accommodate different bunch patterns. The single-cell cavities operate at 4.5 K and are housed in eighteen 3.5 m long cryomodules. Although a number of 500 MHz CW RF systems are currently in operation, development work is required for this 650 MHz system, both for cavities and power sources.

The momentum compaction of the lattice is relatively large, which helps to maintain single bunch stability, but requires a relatively high RF voltage to achieve the design RMS bunch length (9 mm). The dynamic aperture of the lattice is sufficient to allow the large emittance injected beam to be captured with minimal loss.

Challenges

The principal challenges in the damping ring are:

- Control of the electron cloud effect in the positron damping ring. This effect, which can cause instability, tune spread, and emittance growth, has been seen in

a number of other rings and is relatively well understood. Simulations indicate that it can be controlled by proper surface treatment of the vacuum chamber to suppress secondary emission, and by the use of solenoids and clearing electrodes to suppress the buildup of the cloud.

- Control of the fast ion instability in the electron damping ring. This effect can be controlled by limiting the pressure in the electron damping ring to below 1 nTorr, and by the use of short gaps in the ring fill pattern.
- Developing a very fast rise and fall time kicker for single bunch injection and extraction in the ring. For the most demanding region of the beam parameter range, the bunch spacing in the damping ring is ~ 3 ns, and the kicker must have a rise plus fall time no more than twice this. Short stripline kicker structures can achieve this, but the drive pulser technology still needs development.

2.1.2.5 *Ring to Main Linac (RTML)*

Functional requirements

The RTML must perform several critical functions for each beam:

- transport the beam from the damping ring to the upstream end of the linac;
- collimate the beam halo generated in the damping ring;
- rotate the polarization from the vertical to any arbitrary angle required at the IP;
- compress the long Damping Ring bunch length by a factor of 30~45 to provide the short bunches required by the Main Linac and the IP;

System Description

The layout of the RTML is identical for both electrons and positrons, and is shown in Figure 2.9. The RTML consists of the following subsystems:

- ~ 15 km long 5 GeV transport line;
- betatron and energy collimation systems;
- 180° turn-around, which enables feed-forward beam stabilization;
- spin rotator to orient the beam polarization to the desired direction;
- 2-stage bunch compressor to compress the beam bunch length from several millimeters to a few hundred microns as required at the IP.

The bunch compressor includes acceleration from 5 GeV to 13-15 GeV in order to limit the increase in fractional energy spread associated with bunch compression.

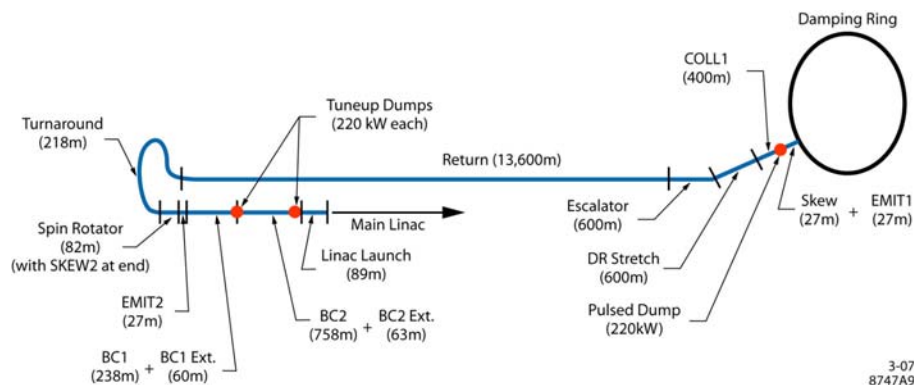


Figure 2.9: Schematic of the RTML

Challenges

The principal challenges in the RTML are:

- Control of emittance growth due to static misalignments, resulting in dispersion and coupling. Simulations indicate that the baseline design for beam-based alignment can limit the emittance growth to tolerable levels.
- Suppression of phase and amplitude jitter in the bunch compressor RF, which can lead to timing errors at the IP. RMS phase jitter of 0.24° between the electron and positron RF systems results in a 2% loss of luminosity. Feedback loops in the bunch compressor low-level RF system should be able to limit the phase jitter to this level.

2.1.2.6 Main Linacs

Functional requirements

The two main linacs accelerate the electron and positron beams from their injected energy of 15 GeV to the final beam energy of 250 GeV, over a combined length of 23 km. The main linacs must:

- accelerate the beam while preserving the small bunch emittances, which requires precise orbit control based on data from high resolution beam position monitors, and also requires control of higher-order modes in the accelerating cavities;
- maintain the beam energy spread within the design requirement of $\sim 0.1\%$ at the IP;
- not introduce significant transverse or longitudinal jitter, which could cause the beams to miss at the collision point.

System Description

The ILC Main Linacs accelerate the beam from 15 GeV to a maximum energy of 250 GeV at an average accelerating gradient of 31.5 MV/m. The linacs are composed of RF units, each of which are formed by three contiguous SCRF cryomodules containing

26 nine-cell cavities. The layout of one unit is illustrated in Figure 2.10. The positron linac contains 278 RF units, and the electron linac has 282 RF units[§].

Each RF unit has a stand-alone RF source, which includes a conventional pulse-transformer type high-voltage (120 kV) modulator, a 10 MW multi-beam klystron, and a waveguide system that distributes the RF power to the cavities (see Figure 2.10). It also includes the low-level RF (LLRF) system to regulate the cavity field levels, interlock systems to protect the source components, and the power supplies and support electronics associated with the operation of the source.

The cryomodule design is a modification of the Type-3 version developed and used at DESY. Within the cryomodules, a 300 mm diameter helium gas return pipe serves as a strongback to support the cavities and other beam line components. The middle cryomodule in each RF unit contains a quad package that includes a superconducting quadrupole magnet at the center, a cavity BPM, and superconducting horizontal and vertical corrector magnets. The quadrupoles establish the main linac magnetic lattice, which is a weak focusing FODO optics with an average beta function of ~ 80 m. All cryomodules are 12.652 m long, so the active length to actual length ratio in a nine-cavity cryomodule is 73.8%. Every cryomodule also contains a 300 mm long high-order mode beam absorber assembly that removes energy through the 40-80 K cooling system from beam-induced higher-order modes above the cavity cutoff frequency.

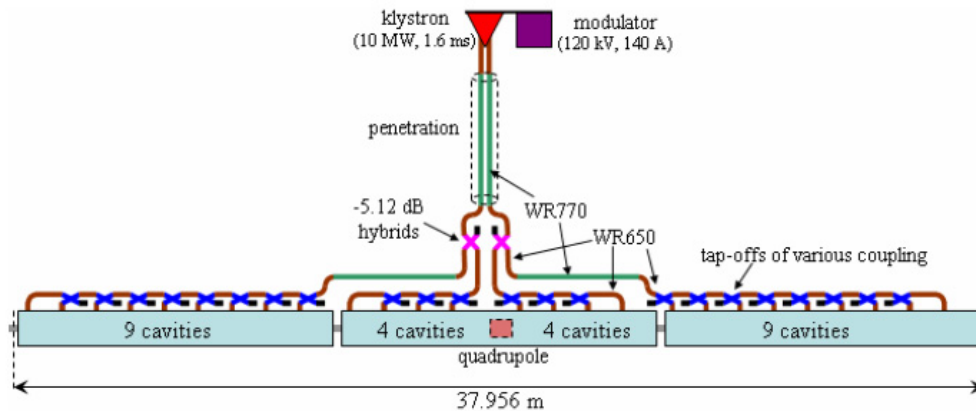


Figure 2.10: RF unit layout.

To operate the cavities at 2 K, they are immersed in a saturated He II bath, and helium gas-cooled shields intercept thermal radiation and thermal conduction at 5-8 K and at 40-80 K. The estimated static and dynamic cryogenic heat loads per RF unit at 2 K are 5.1 W and 29 W, respectively. Liquid helium for the main linacs and the RTML is supplied from 10 large cryogenic plants, each of which has an installed equivalent cooling power of ~ 20 kW at 4.5 K. The main linacs follow the average Earth's curvature to simplify the liquid helium transport.

[§] Approximate 3 GeV of extra energy is required in the electron linac to compensate for positron production.

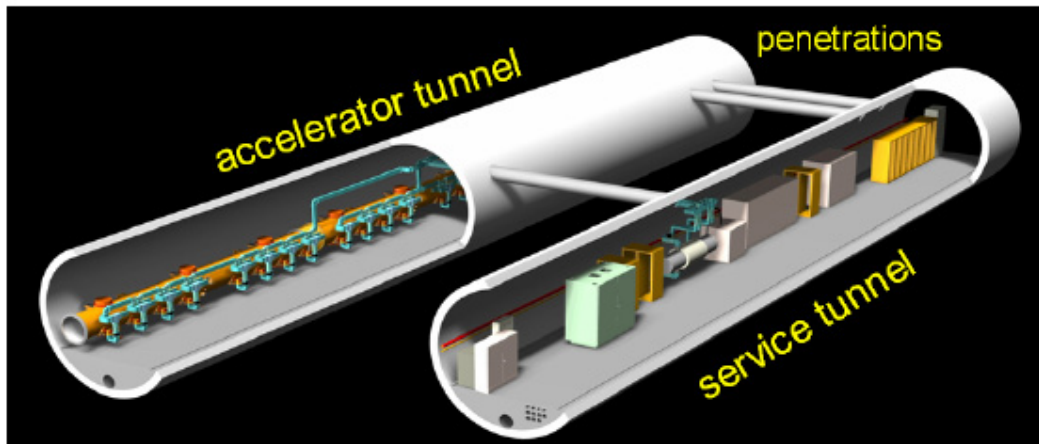


Figure 2.11: Cutaway view of the linac dual-tunnel configuration.

The Main Linac components are housed in two tunnels, an accelerator tunnel and a service tunnel, each of which has an interior diameter of 4.5 meters. To facilitate maintenance and limit radiation exposure, the RF source is housed mainly in the service tunnel as illustrated in Figure 2.11.

The tunnels are typically hundreds of meters underground and are connected to the surface through vertical shafts^{**}. Each of the main linacs includes three shafts, roughly 5 km apart as dictated by the cryogenic system. The upstream shafts in each linac have diameters of 14 m to accommodate lowering cryomodules horizontally, and the downstream shaft in each linac is 9 m in diameter, which is the minimum size required to accommodate tunnel boring machines. At the base of each shaft is a 14,100 cubic meter cavern for staging installation and housing utilities and parts of the cryoplant, most of which are located on the surface.

Challenges

The principal challenges in the main linac are:

- Realizing the design average accelerating gradient of 31.5 MV/m. This operating gradient is higher than that typically achievable today and assumes further progress will be made during the next few years in the aggressive program that is being pursued to improve cavity performance.
- Control of emittance growth due to static misalignments, resulting in dispersion and coupling. Beam-based alignment techniques should be able to limit the single-bunch emittance growth. Long-range multibunch effects are mitigated via HOM damping ports on the cavities, HOM absorbers at the quadrupoles, and HOM detuning. Coupling from mode-rotation HOMs is limited by splitting the horizontal and vertical betatron tunes.
- Control of the beam energy spread. The LLRF system monitors the vector sum of the fields in the 26 cavities of each RF unit and makes adjustments to flatten the energy gain along the bunch train and maintain the beam-to-RF phase

^{**} Except for the Asian sample site: see Section 1.4.

constant. Experience from FLASH and simulations indicate that the baseline system should perform to specifications.

2.1.2.7 *Beam Delivery System*

Functional requirements

The ILC Beam Delivery System (BDS) is responsible for transporting the e^+e^- beams from the exit of the high energy linacs, focusing them to the sizes required to meet the ILC luminosity goals, bringing them into collision, and then transporting the spent beams to the main beam dumps. In addition, the BDS must perform several other critical functions:

- measure the linac beam and match it into the final focus;
- protect the beamline and detector against mis-steered beams from the main linacs;
- remove any large amplitude particles (beam-halo) from the linac to minimize background in the detectors;
- measure and monitor the key physics parameters such as energy and polarization before and after the collisions.

System Description

The layout of the beam delivery system is shown in Figure 2.12. There is a single collision point with a 14 mrad total crossing angle. The 14 mrad geometry provides space for separate extraction lines but requires crab cavities to rotate the bunches in the horizontal plane for effective head-on collisions. There are two detectors in a common interaction region (IR) hall in a so-called “push-pull” configuration. The detectors are pre-assembled on the surface and then lowered into the IR hall when the hall is ready for occupancy.

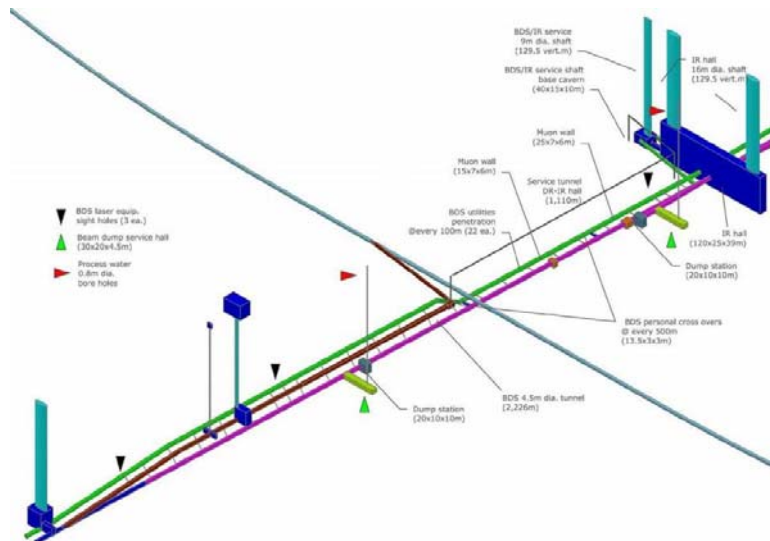


Figure 2.12: BDS layout, beam and service tunnels (shown in magenta and green), shafts, experimental hall. The line crossing the BDS beamline at right angles is the damping ring, located 10 m above the BDS tunnels.

The BDS is designed for 500 GeV center-of-mass energy but can be upgraded to 1 TeV with additional magnets.

The main subsystems of the beam delivery, starting from the exit of the main linacs, are:

- A section containing post-linac emittance measurement and matching (correction) sections, trajectory feedback, polarimetry and energy diagnostics.
- A fast pulsed extraction system used to extract beams in case of a fault, or to dump the beam when not needed at the IP.
- A collimation section which removes beam halo particles that would otherwise generate unacceptable background in the detector, and also contains magnetized iron shielding to deflect muons.
- The final focus (FF) which uses strong compact superconducting quadrupoles to focus the beam at the IP, with sextupoles providing local chromaticity correction.
- The interaction region, containing the experimental detectors. The final focus quadrupoles closest to the IP are integrated into the detector to facilitate detector “push-pull”.
- The extraction line, which has a large enough bandwidth to cleanly transport the heavily disrupted beam to a high-powered water-cooled dump. The extraction line also contains important polarization and energy diagnostics.

Challenges

The principal challenges in the beam delivery system are:

- Tight tolerances on magnet motion (down to tens of nanometers), which make the use of fast beam-based feedbacks systems mandatory, and may well require mechanical stabilization of critical components (e.g. final doublets).
- Uncorrelated relative phase jitter between the crab cavity systems, which must be limited to the level of tens of femtoseconds.
- Control of emittance growth due to static misalignments, which requires beam-based alignment and tuning techniques similar to the RTML.
- Control of backgrounds at the IP via careful tuning and optimization of the collimation systems and the use of the tail-folding octupoles.
- Clean extraction of the high-powered disrupted beam to the dump. Simulations indicate that the current design is adequate over the full range of beam parameters.

2.1.3 Sample Sites

CFS (Conventional Facilities and Siting) is responsible for civil engineering, power distribution, water cooling and air conditioning systems. The value estimate (see Section 2.5 below) for the CFS is approximately 38% of the total estimated project value.

In the absence of a single agreed-upon location for the ILC, a sample site in each region was developed. Each site was designed to support the ILC baseline design described in Section 1.3. Although many of the basic requirements are identical, differences in geology, topography and local standards and regulations lead to different construction approaches, resulting in a slight variance in value estimates across the three

regions. Although many aspects of the CFS (and indeed machine design) will ultimately depend on the specific host site chosen, the approach taken here is considered sufficient for the current design phase, while giving a good indication of the influence of site-specific issues on the project as a whole.

All three sites satisfied a matrix of criteria agreed upon by the regional CFS groups early in the RDR process, including the mandatory requirement that all sites can support the extension to the 1 TeV center-of-mass machine.

The three sample sites have the following characteristics:

- The Americas sample site lies in Northern Illinois near the existing Fermilab. The site provides a range of locations to position the ILC in a north-south orientation. The site chosen has approximately one-quarter of the machine on the Fermilab site. The surface is primarily flat. The long tunnels are bored in a contiguous dolomite rock strata ('Galena Platteville'), at a typical depth of 30-100 m below the surface.
- The Asian site has been chosen from several possible ILC candidate sites in Japan. The sample site has a uniform terrain located along a mountain range, with a tunnel depth ranging from 40 m to 600 m. The chosen geology is uniform granite highly suited to modern tunneling methods. One specific difference for the Asian site is the use of long sloping access tunnels instead of vertical shafts, the exception being the experimental hall at the Interaction Region, which is accessed via two 112 m deep vertical shafts. The sloping access tunnels take advantage of the mountainous location of the sample site.
- The European site is located at CERN, Geneva, Switzerland, and runs parallel to the Jura mountain range, close to the CERN site. The majority of the machine is located in the 'Molasse' (a local impermeable sedimentary rock), at a typical depth of 370 m.

The elevations of the three sample sites are shown in Figure 2.13. The tunnels for all three sites would be predominantly constructed using Tunnel Boring Machines (TBM), at typical rates of 20–30 m per day. The Molasse of the European site near CERN requires a reinforced concrete lining for the entire tunnel length. The Asian site (granite) requires rock bolts and a 5 cm 'shotcrete' lining. The US site is expected to require a concrete lining for only approximately 20% of its length, with rock-bolts being sufficient for permanent structural support.

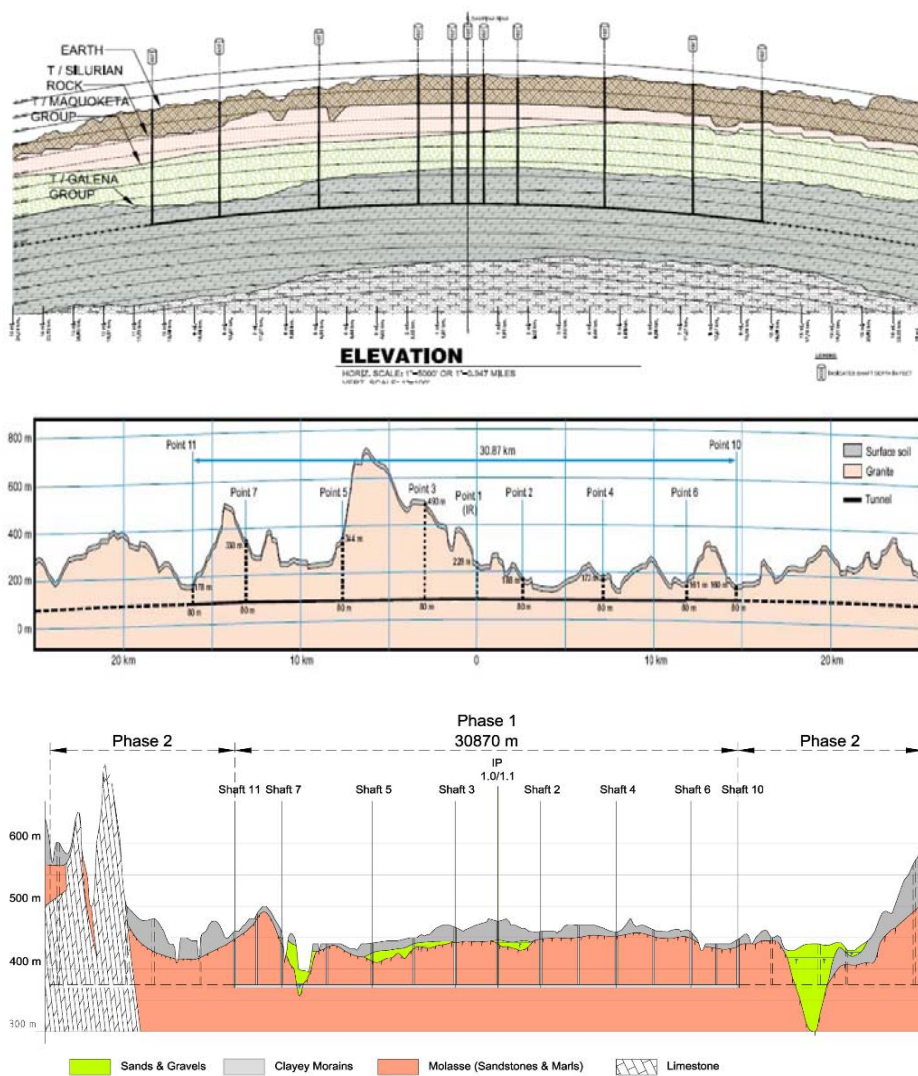


Figure 2.13: Geology and tunnel profiles for the three regional sites, showing the location of the major access shafts (tunnels for the Asian site). Top: the Americas site close to Fermilab. Middle: the Asian site. Bottom: the European site close to CERN.

A second European sample site near DESY, Hamburg, Germany, has also been developed. This site is significantly different from the three reported sites, both in geology and depth (~25 m deep), and requires further study.

In addition, the Joint Institute for Nuclear Research has submitted a proposal to site the ILC in the neighborhood of Dubna, Russian Federation.

The three sites reported in detail here are all ‘deep-tunnel’ solutions. The DESY and Dubna sites are examples of ‘shallow’ sites. A more complete study of shallow sites – shallow tunnel or cut-and-cover – will be made in the future as part of the Engineering and Design phase.

2.1.4 Value Estimate

A preliminary cost analysis has been performed for the ILC Reference Design. A primary goal of the estimate was to allow cost-to-performance optimization in the Reference Design, before entering into the engineering design phase. Over the past year, the component costs were estimated, various options compared and the design evolved through about ten significant cost-driven changes, resulting in a cost reduction of about 25%, while still maintaining the physics performance goals.

The ILC cost estimates have been performed using a “value” costing system, which provides basic agreed-to value costs for components in ILC Units^{††}, and an estimate of the *explicit* labor (in person hours) that is required to support the project. The estimates are based on making world-wide tenders in major industrialized nations, using the lowest reasonable price for the required quality. There are three classes of costs:

- site-specific costs, where a separate estimate was made in each of the three regions;
- conventional costs for items where there is global capability – here a single cost was determined;
- costs for specialized high-tech components (e.g. the SCRF linac technology), where industrial studies and engineering estimates were used.

The total estimated value for the shared ILC costs for the Reference Design is 4.87 Billion (ILC Units). An important outcome of the value costing has been to provide a sound basis for determining the relative value of the various components or work packages. This will enable equitable division of the commitments of the world-wide collaboration.

In addition, the site specific costs, which are related to the direct costs to provide the infrastructure required to site the machine, are estimated to be 1.78 Billion (ILC Units). These costs include the underground civil facilities, water and electricity distribution and buildings directly supporting ILC operations and construction on the surface. The costs were determined to be almost identical for the Americas, Asian, and European sample sites. It should be noted that the actual site-specific costs will depend on where the machine is constructed, and the facilities that already exist at that location.

Finally, the explicit labor required to support the construction project is estimated at 22 million person-hours; this includes administration and project management, installation and testing. This labor may be provided in different ways, with some being contracted and some coming from existing labor in collaborating institutions.

The ILC Reference Design cost estimates and the tools that have been developed will play a crucial role in the engineering design effort, both in terms of studying options for reducing costs or improving performance, and in guiding value engineering studies, as well as supporting the continued development of a prioritized R&D program.

The total estimated value cost for the ILC, defined by the Reference Design, including shared value costs, site specific costs and explicit labor, is comparable to other recent major international projects, e.g. ITER, and the CERN LHC when the cost of pre-existing facilities are taken into account. The GDE is confident that the overall scale of the project has been reliably estimated and that cost growth can be contained in the engineering phase, leading to a final project cost consistent with that determined at this early stage in the design.

^{††} For this value estimate, 1 ILC Unit = 1 US 2007\$ (= 0.83 Euro = 117 Yen).

2.1.5 R&D and the Engineering Design Phase

For the last year, the focus of the core GDE activity has been on producing the RDR and value estimate. In parallel, ILC R&D programs around the world have been ramping up to face the considerable challenges ahead. The GDE Global R&D Board – a group of twelve GDE members from the three regions – has evaluated existing programs, and has convened task forces of relevant experts to produce an internationally agreed-upon prioritized R&D plan for the critical items. The highest-priority task force (S0/S1) addresses the SCRF accelerating gradient:

- S0: high-gradient cavity – aiming to achieve 35 MV/m nine-cell cavity performance with an 80% production yield.
- S1: high-gradient cryomodule – the development of one or more high-gradient ILC cryomodules with an average operational gradient of 31.5 MV/m.

The S0/S1 task force has already produced focused and comprehensive R&D plans. Other task forces (S2: test linac; S3: Damping Ring; S4: Beam Delivery System, *etc.*) are in the process of either completing their reports, or just beginning their work.

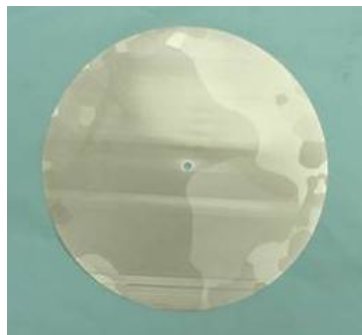
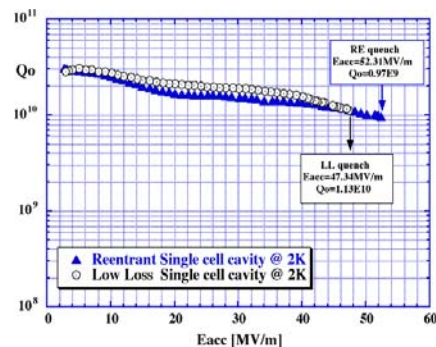


Figure 2.14: Cutting-edge SCRF R&D. top-left: ICHIRO single-cells being prepared for testing at KEK. Top right: world-record performance from novel shape single-cells (ICHIRO and Cornell's reentrant cavity). Bottom left: large-grain niobium disk (JLAB). Bottom-right: single-cell cavity produced from large-grain niobium material (JLAB).

For the cost- and performance-critical SCRF, the primary focus of S0/S1 remains the baseline choice, the relatively mature TESLA nine-cell elliptical cavity. However, additional research into alternative cavity shapes and materials continues in parallel. One promising technique is the use of 'large-grain' niobium [8], as opposed to the small-grain material that has been used in the past (Figure 2.14). Use of large grain material may remove the need for electropolishing, since the same surface finish can

potentially be achieved with Buffered Chemical Polishing (BCP) – a possible cost saving. Several single-cells have achieved gradients in excess of 35 MV/m (without electropolishing) and more recent nine-cell cavity tests have shown very promising results.

Various new and promising cavity shapes are also being investigated, primarily at KEK and Cornell. While the basic nine-cell form remains, the exact shape of the ‘cells’ is modified to reduce the peak magnetic field at the niobium surface. In principle these new shapes can achieve higher gradients, or higher *quality factors* (Q_0). Single-cells at KEK (ICHIRO) and Cornell (reentrant) have achieved the highest gradients to date (~50 MV/m, see Figure 2.14). R&D towards making high-performance nine-cell cavities using these designs continues as future possible alternatives to the ILC baseline cavity.

Beyond the cavity itself, R&D on several alternative designs that promise potentially cost and/or performance benefit alternatives is also formally supported by the GDE. Some key examples are alternative RF power source components, of which the Marx modulator is currently the most promising. In addition, R&D on the critical technologies will continue through the EDR. Topics include items such as the damping ring kickers and electron-cloud mitigation techniques, the positron target and undulator, the final magnets around the interaction region, and global issues that require very high availability such as the control system, the low-level RF, and the magnet power supplies.

While investment into the critical R&D remains a priority, a significant ramping-up of global engineering resources will now be required to produce an engineered technical design by 2010. An important aspect of this work will be the refinement and control of the published estimate by value engineering. The EDR phase will also require a restructuring of the GDE to support the increased scope. A more traditional project structure will be adopted based on the definition of a discrete set of Work Packages. The responsibility for achieving the milestones and deliverables of each Work Package will be assigned to either a single institute, or consortium of institutes, under the overall coordination of a central project management team. The Work Packages need to be carefully constructed to accommodate both the direct needs of the Engineering Design phase, while at the same time reflecting the global nature of the project. An important goal of the current planning is to integrate the engineering design and fundamental R&D efforts, since these two aspects of the project are clearly not independent. The goal is to have the new project structure ready to start the EDR in place by mid 2007.

2.1.6 References

1. ITRP Recommendation, http://www.fnal.gov/directorate/icfa/ITRP_Report_Final.pdf (2004).
2. R. Brinkmann et. al., eds., “TESLA Technical Design Report”, DESY-2001-011 (March, 2001).
3. T. O. Raubenheimer et. al., eds., “Zeroth Order Design Report for the Next Linear Collider”, SLAC-R-474 (1996); N. Phinney, ed., “2001 report on the Next Linear Collider: A report submitted to Snowmass ’01”, SLAC-R-571 (2001).
4. “GLC project: Linear Collider for TeV Physics.”, KEK-Report-2003-7, <http://lcdev.kek.jp/Roadmap/> (2003)
5. M. Altarelli *et al*, “The European X-Ray Free-Electron Laser Technical Design Report”, DESY 2006-097 (2006).

6. ILCSC Parameters Document, http://www.fnal.gov/directorate/icfa/LC_parameters.pdf (2003).
7. F. Furuta *et al.*, “Experimental comparison at KEK of High Gradient Performance of Different Single-Cell Superconducting Cavity Designs”, EPAC06 Proceedings, MOPLS084 750-753 (2006); R. L. Geng *et al.*, “High-Gradient Activities at Cornell: Reentrant Cavities”, SRF 2005 Proceedings, TUP43 (2005).
8. P. Kneisel *et al.*, “Preliminary Results from Single Crystal and Very Large Crystal Niobium Cavities”, PAC05 Proceedings, 3991-3993 (2005).

2.2 Second International Accelerator School for Linear Colliders

Barry Barish, Shin-ichi Kurokawa and Weiren Chou

Mail to: barish@ligo.caltech.edu, shin-ichi.kurokawa@kek.jp, chou@fnal.gov

We are pleased to announce the *Second International Accelerator School for Linear Colliders*. This school is a continuation of the first school held last year at Sokendai, Japan. It is organized jointly by the International Linear Collider (ILC) Global Design Effort (GDE), the International Linear Collider Steering Committee (ILCSC) and the International Committee for Future Accelerators (ICFA) Beam Dynamics Panel. The school this year will take place at the Ettore Majorana Center, Erice (Sicily), Italy from October 1 – 10, 2007. The school is sponsored by the U.S. Department of Energy (DOE) Office of Science, the U.S. National Science Foundation (NSF), Fermilab, SLAC, CERN, DESY, KEK, PPARC, INFN, IN2P3 and CARE/ELAN.

We will offer an 8-day program, including a half-day for excursions. There will be a total of 12 lectures covering both basic accelerator topics (e.g. synchrotrons, linacs, superconductivity, beam-beam interactions, etc.) and advanced topics. Most of the advanced topics will be focused on the ILC (e.g., sources, bunch compressor, damping ring, superconducting RF linac, beam delivery, instrumentation, feedback, conventional facilities and operations). There will also be a lecture dedicated to room temperature RF and the Compact Linear Collider (CLIC). All lectures will run in sequence. (There will be no parallel sessions.) A complete description of the program is attached. There will be homework assignments and a final examination but no university credits.

We encourage young physicists (graduate students, post doctoral fellows, junior researchers) to apply. In particular we welcome those physicists who are considering changing to a career in accelerator physics. The school will accept a maximum of 70 students from around the world. Students will receive financial aid covering the expenses for attending this school (including airfare, lodging, meals, local transportation and school supplies). There will be no registration fee. Each applicant should complete the online registration form (located at www.linearcollider.org/school/2007/) and send us a curriculum vita as well as a recommendation letter from his/her supervisor (in electronic form, either PDF or MS WORD). **The deadline for application is June 1, 2007.**

For more information contact

Cynthia M. Sazama
 Fermilab, PO. Box 500
 Batavia, IL 60510 USA
 Fax: +1-630-840-8589
 E-mail: sazama@fnal.gov

2.2.1 Committees

Organizing Committee	Curriculum Committee
Barry Barish (GDE/Caltech, Chair) Shin-ichi Kurokawa (ILCSC/KEK) Weiren Chou (ICFA BD Panel/Fermilab) Jean-Pierre Delahaye (CERN) Rolf-Dieter Heuer (DESY) In Soo Ko (PAL) Kaoru Yokoya (KEK) Alex Chao (SLAC) Paul Grannis (US DOE)	Weiren Chou (Fermilab, Chair) William Barletta (USPAS) Daniel Brandt (CERN) Alex Chao (SLAC) Jie Gao (IHEP/China) Shin-ichi Kurokawa (KEK) Carlo Pagani (INFN/Milano) Junji Urakawa (KEK) Andrzej Wolski (Univ. of Liverpool)

2.2.2 Lecturers

Lecture	Topic	Lecturer
1	Introduction	Nick Walker (DESY)
2	Sources & Bunch Compressors	Masao Kuriki (KEK)
3	Damping Ring	Andy Wolski (U. Liverpool)
4	Linac	Peter Tenenbaum (SLAC)
5	LLRF & High Power RF	Stefan Simrock (DESY)
6	Superconducting RF	Kenji Saito (KEK)
7	Beam Delivery & Beam-Beam	Andrei Seryi (SLAC)
8	Instrumentation & Control	Marc Ross (Fermilab)
9	Operations	Marc Ross (Fermilab)
10	CLIC	Frank Tecker (CERN)
11	Conventional Facilities	Atsushi Enomoto (KEK)
12	Physics & Detectors	Jim Brau (U. Oregon)

Second International Accelerator School for Linear Colliders – Curriculum (v.3, 04/17/2007)

October 1-10, 2007, Ettore Majorana Center, Erice (Sicily), Italy

Daily Schedule

Activity	Time
Breakfast	08:00 – 09:00
Morning Session	09:00 – 12:30, including ½-hour break
Lunch	12:30 – 14:30
Afternoon Session	14:30 – 18:00, including ½-hour break
Tutorial & Homework	18:30 – 21:00
Dinner	21:00 –

List of Courses

Day	Morning	Afternoon	Evening
October 1		<i>Arrival, registration</i>	<i>Reception</i>
October 2	Introduction	Sources & Bunch Compressors	Tutorial & Homework
October 3	Damping Ring I	Linac I	Tutorial & Homework
October 4	Damping Ring II	Linac II	Tutorial & Homework
October 5	LLRF & High Power RF	<i>Excursion</i>	Tutorial & Homework; <i>Banquet</i>
October 6	Superconducting RF I	Beam Delivery & Beam-Beam	Tutorial & Homework
October 7	Superconducting RF II	Instrumentation & control I	Tutorial & Homework
October 8	Instrumentation & Control II; Operations	CLIC	Tutorial & Homework
October 9	<i>Final exam</i>	Conventional Facilities; Physics & Detectors	<i>Free time</i>
October 10	<i>Departure</i>		

Program

	<i>Tuesday, October 2</i>	<i>Wednesday, October 3</i>	<i>Thursday, October 4</i>	<i>Friday, October 5</i>
Morning 09:00 – 12:30	<p>Opening Remarks (10)</p> <p>Lecture 1 – Introduction (180) <i>Nick Walker (DESY)</i></p> <ul style="list-style-type: none"> • Why LC • What’s ILC • Layout of ILC • Parameter choices & optimization • Overview of accelerator issues 	<p>Lecture 3 – Damping Ring I (180) <i>Andy Wolski (U. Liverpool)</i></p> <ul style="list-style-type: none"> • Role of damping rings • High-level overview of structure, and principles of operation • Review of basic linear beam dynamics • Damping ring lattice • Radiation damping (derivation of damping times, and the need for a damping wiggler in LC damping rings) • Quantum excitation and equilibrium beam emittances 	<p>Lecture 3 – Damping Ring II (180) <i>Andy Wolski (U. Liverpool)</i></p> <ul style="list-style-type: none"> • Brief overview of technical systems • R&D challenges for selected technical components <ul style="list-style-type: none"> ➢ injection/extraction kickers ➢ damping wiggler • Brief overview of beam dynamics issues • Selected beam dynamics issues <ul style="list-style-type: none"> ➢ impedance effects ➢ electron cloud effects 	<p>Lecture 5 – LLRF & High Power RF (180) <i>Stefan Simrock (DESY)</i></p> <ul style="list-style-type: none"> • RF system overview • LLRF • Timing and synchronization • Modulators • Klystrons • RF distribution
Afternoon 14:30 – 18:00	<p>Lecture 2 – Sources & Bunch Compressors (180) <i>Masao Kuriki (KEK)</i></p> <ul style="list-style-type: none"> • e^- gun • e^+ sources • Polarized sources • Bunch compressors • Spin rotator 	<p>Lecture 4 – Linac I (180) <i>Peter Tenenbaum (SLAC)</i></p> <ul style="list-style-type: none"> • Tutorials of linac basics • Standing wave linacs and structures • SRF parameter constraints • Beam loading and coupling • Lorentz force detuning 	<p>Lecture 4 – Linac II (180) <i>Peter Tenenbaum (SLAC)</i></p> <ul style="list-style-type: none"> • Linac lattice • Emittance preservation • RF field stability • Wakefield and dampers • HOMs • Alignment issues • Vibration issues • Beam based alignment 	Excursion
Evening 18:30 – 21:00	Tutorial & homework	Tutorial & homework	Tutorial & homework	Tutorial & homework; Banquet

Program (cont'd)

	Saturday, October 6	Sunday, October 7	Monday, October 8	Tuesday, October 9
Morning 09:00 – 12:30	Lecture 6 – Superconducting RF I (180) <i>Kenji Saito (KEK)</i> <ul style="list-style-type: none"> • Superconductivity basics • SRF specifics and constraints • Cavity design • Cryogenics • ILC cryomodules 	Lecture 6 – Superconducting RF II (180) <i>Kenji Saito (KEK)</i> <ul style="list-style-type: none"> • Material issues • Cavity fabrication and tuning • Surface preparation • Gradient limit and spread • Power Coupler • HOM Couplers • Slow and fast tuner • ILC design 	Lecture 8 – Instrumentation & Control II (90) <i>Marc Ross (Fermilab)</i> <ul style="list-style-type: none"> • Electronics • Data processing Lecture 9 – Operations (90) <i>Mark Ross (Fermilab)</i> <ul style="list-style-type: none"> • Reliability • Availability • Remote control and global network 	Final Exam (180)
Afternoon 14:30 – 18:00	Lecture 7 – Beam Delivery & Beam-Beam (180) <i>Andrei Seryi (SLAC)</i> <ul style="list-style-type: none"> • Overview • Beam-beam interaction and crossing angle • Collimation • Accelerator-detector interface, shielding and beam dump • Background and detector protection • Beam monitoring and control at final focus 	Lecture 8 – Instrumentation & Control I (180) <i>Mark Ross (Fermilab)</i> <ul style="list-style-type: none"> • Beam monitoring • Precision instrumentation • Feedback systems • Energy stability • Orbit control 	Lecture 10 – CLIC (90) <i>Frank Tecker (CERN)</i> <ul style="list-style-type: none"> • Room temperature RF cavities • CLIC design • Differences between CLIC and ILC • Challenges to CLIC Study time (90)	Lecture 11 – Conventional Facilities (90) <i>Atushi Enomoto (KEK)</i> <ul style="list-style-type: none"> • Overview • Tunneling • Site requirement Lecture 12 – Physics & Detectors (90) <i>Jim Brau (U. Oregon)</i> <ul style="list-style-type: none"> • Tera scale physics • Physics beyond 1 TeV • ILC vs. LHC • Detectors
Evening 18:30 – 21:00	Tutorial & homework	Tutorial & homework	Tutorial & homework	Student Awards Ceremony <i>Free time</i>

Notes to the Program:

1. Compared to the last LC school, one major change is that the number of lectures is reduced from 21 to 12. Each lecture will be covered by one lecturer.
2. Another change is the social time during/after dinner.
3. Total of 8 lecture days, Oct 2 – Oct 9, with one afternoon excursion/free. No hands-on courses this time (not because it is not desirable).
4. In order to reduce students' homework load, there will still be homework assignments, but no homework due for grade. Instead, there will be a final exam, and some of the exam problems are to be taken from the homework assignments. Lectures 11 and 12 take place after the final exam. So they do not take part in the exam. The exam papers will be graded right after the exam and results announced late afternoon on Oct. 9 at the Student Awards Ceremony.
5. During registration, each student will be assigned to a small group (1 or 2 people from each region). We will encourage students to do homework with their group. But we won't enforce it. We will also allow students to change group if they feel more comfortable.
6. Every day in the last hour of the homework time, some students or representatives of groups will be invited to the blackboard and demonstrate the solutions.
7. Lecturers should be strongly suggested to cover the basics as well as possible. Their teaching material should be made available (on-line) to the students well ahead of time (~ 1 month prior to the school).
8. Lecturers should be available in the evening of their lecture day during the tutorial & homework time.
9. Lecturers are responsible for the design of homework and exam problems as well as the answer sheet. They are also responsible for grading the exams.
10. The awards ceremony will honor top (~10) students based on their exams.

3 Free-Electron Laser

3.1 Beam Dynamics at FLASH and the European XFEL

Editors: W. Decking and T. Limberg
Mail to: winfried.decking@desy.de
[DESY](http://www.desy.de), 22603 Hamburg

3.1.1 Introduction

FLASH [1] is a VUV-FEL [1] user facility at DESY presently with a beam energy of up to 750 MeV and wavelengths down to 13 nm; the European XFEL [2] is a much bigger machine with beam energies close to 20 GeV and wavelengths as short as 1 Å, which is to be commissioned in 2013. Beam dynamics in both machines deals with

producing bunches with high charge densities, corresponding to peak currents in the kA range, whilst avoiding emittance blow up due to collective effects. The strong self-fields of the intense bunches can also give rise to the so-called micro-bunching instability where the interplay of space charge and Coherent Synchrotron Radiation (CSR) fields and longitudinal compression in dispersive sections can lead to strong unwanted intensity modulations within the bunch.

After a short description of the machine lay-outs, we will present calculations of beam transport, so called ‘start-to-end’ simulations, and compare their predictions with measurements at FLASH. To ensure our understanding of the physics involved, we started dedicated measurements and present results of one of those probing CSR effects. For the European XFEL, we will discuss stability issues, specifically the optimization of the bunch compression to avoid tight rf tolerances and bunch distortions by the micro-bunching instability at the same time. Finally, we will look into possibilities to measure the onset of the micro-bunching instability at FLASH.

FLASH is based on the TESLA Test Facility (TTF), a superconducting linear accelerator constructed within the TESLA collaboration. A schematic layout is shown in Figure 1. The bunches will be accelerated to up to 1 GeV, after the installation of an additional TESLA rf module this year. That will bring the design wavelength of 6 nm in reach. Bunch charges between 0.5 and 1.5 nC are used. At intermediate energies of 130 MeV and 380 MeV the bunches are longitudinally compressed in magnetic chicanes.

The European X-ray Free-Electron Laser Facility is a new international scientific infrastructure to be built in the north-west of Hamburg. The purpose of the facility is to generate ultra-short pulses (~ 100 fs) of spatially coherent X-rays with wavelengths down to 0.1 nm with a brilliance of about 10^{33} photons/s/mm²/mrad²/0.1% bandwidth. Longitudinal bunch compression is done at 0.5 GeV and 2 GeV. The bunch, after traversing the main linac and a collimation section, enters with a peak current of about 5 kA and an energy of 17.5 GeV the up to 200 m long undulators. Five photon beam lines deliver the X-ray pulses to ten experimental stations.

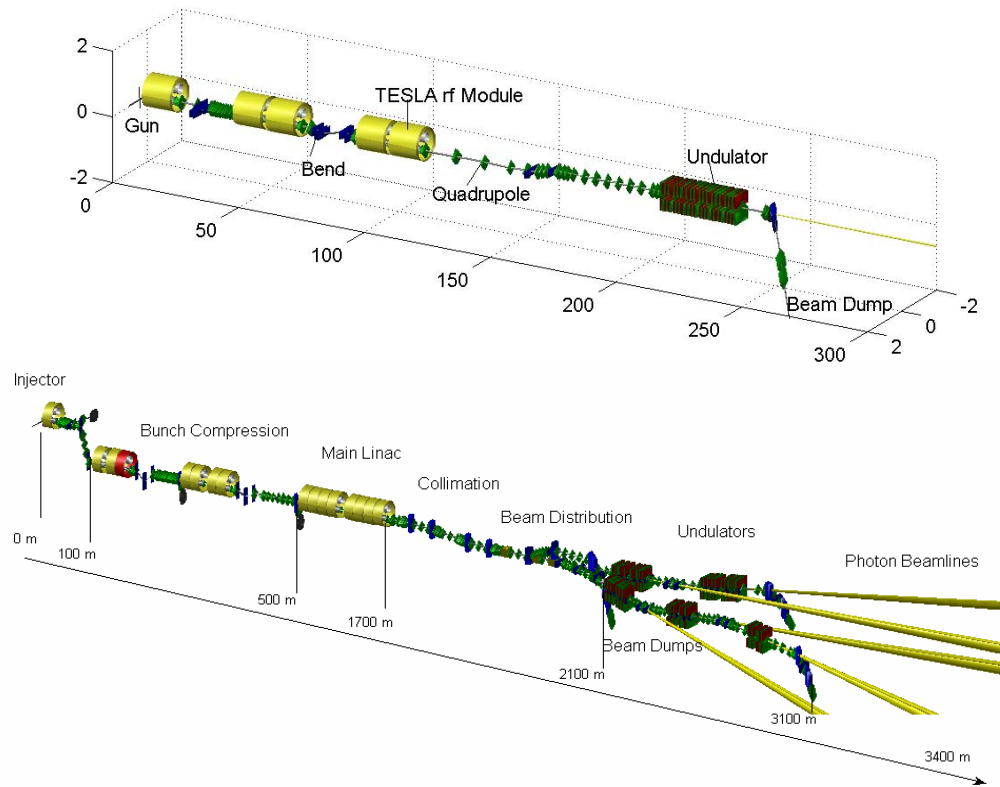
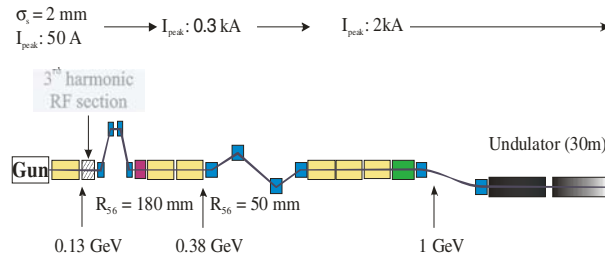


Figure 1: Sketches of FLASH (top, to scale) and the European XFEL.

3.1.2 Bunch Compression and Start-to-End Simulations

Both machines produce bunch trains generated from a Cs_2Te cathode illuminated by a UV laser pulse with a few ps rms duration and about 50 A peak current. Longitudinal compression has to be used to achieve the 2-5 kA peak currents necessary for lasing. The layout of the bunch compression systems is sketched in Figure 2. The design is similar for both machines: the initially 2 mm rms long bunch is compressed in two magnetic chicanes. An energy chirp is injected mostly by running off-crest in the rf module(s) upstream of the first chicane. A third harmonic rf system is used to remove the non-linear part of that chirp and to optimize the final longitudinal charge distribution. Results of a start-to-end (S2E) simulation for the optimized bunch compression simulation for the European XFEL are shown in Figure 3. The initial normalized emittance of 0.8 mm mrad in the core of the bunch is, in an unperturbed machine, preserved throughout the compression to 5 kA peak current. A 10 MeV energy chirp after the bunch compression is taken out almost completely by the main linac longitudinal wake fields. The correlation in the longitudinal phase space plotted in Figure 3 (upper-right) is caused by longitudinal space charge forces downstream of the 2 GeV chicane.

FLASH



European XFEL

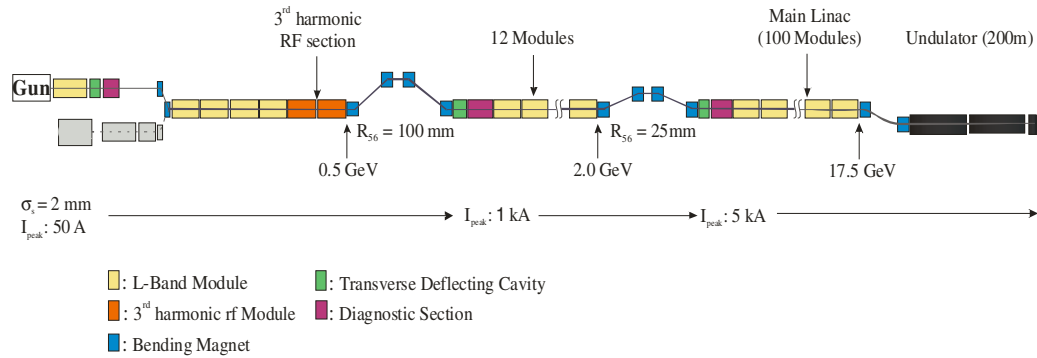


Figure 2: Schematic layout of the FLASH and European XFEL bunch compression systems.

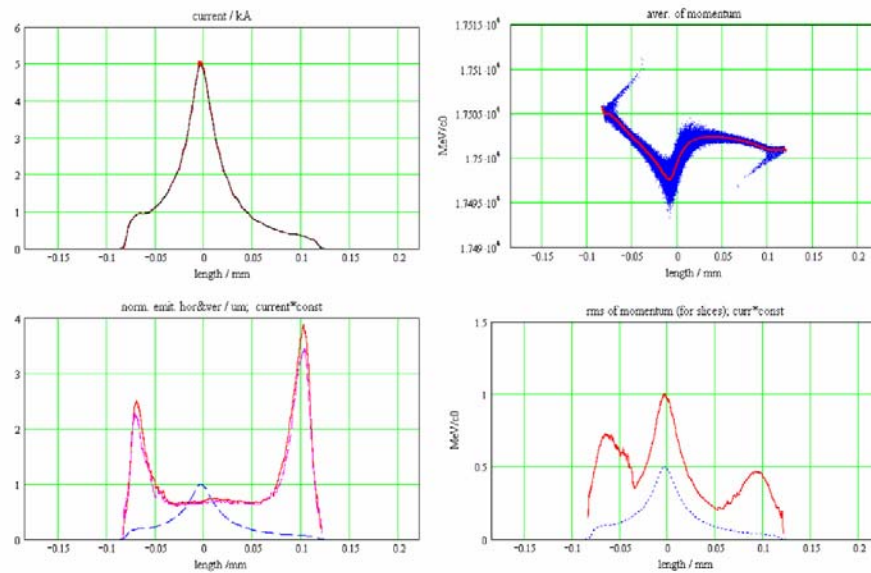


Figure 3: Compression in the XFEL: Longitudinal current distribution (upper left), longitudinal phase space (upper right), slice emittance (lower left) and slice energy spread (lower right) at the entrance of the undulator. The blue lines in the lower row represent again the current distribution.

For FEL driver linacs, start-to-end calculations must include coherent synchrotron radiation effects, space charge forces and the impact of wake fields [3]. Figure 4 shows a scheme of such a calculation:

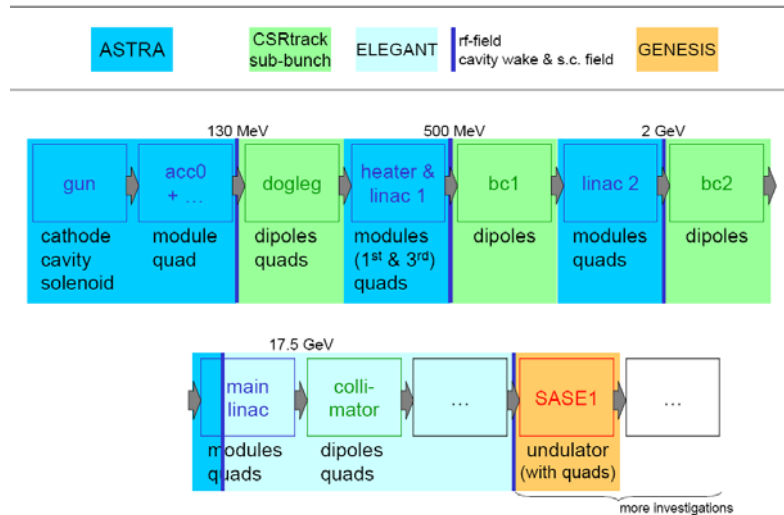


Figure 4: Schematic layout of a start-to-end simulation for the European XFEL.

Different computer codes are used for different sections of the machine, since beam physics changes from the gun to the undulator. A point where FEL driver linacs differ from other linacs is the necessity to take space charge effects into account up to the GeV range, which is caused by the successive increase in peak current.

Up to now, no 3rd harmonic rf system has been installed at FLASH. The present mode of operation cannot correct the non-linearity of the longitudinal phase space; the bunch is over-compressed with some parts of the bunch in full compression. The beam distribution is strongly spiked with a long tail. Only a small fraction of the bunch is contributing to the SASE process, but the spike provides a very short photon pulse (30 fs) and this mode of operation is relatively insensitive to rf amplitude and phase jitter.

Figure 5 shows as a result of a start-to-end simulation the longitudinal phase space distribution in front of the FLASH SASE undulator. Coherent synchrotron radiation and space charge effects have distorted the distribution in the vicinity of the head of the bunch, where the peak current is high enough to expect FEL gain saturation. Since this distortion occurs mostly in dispersive sections, also the transverse phase space is perturbed. As a consequence, not all the particles within the head of the bunch have an emittance sufficiently small for lasing.

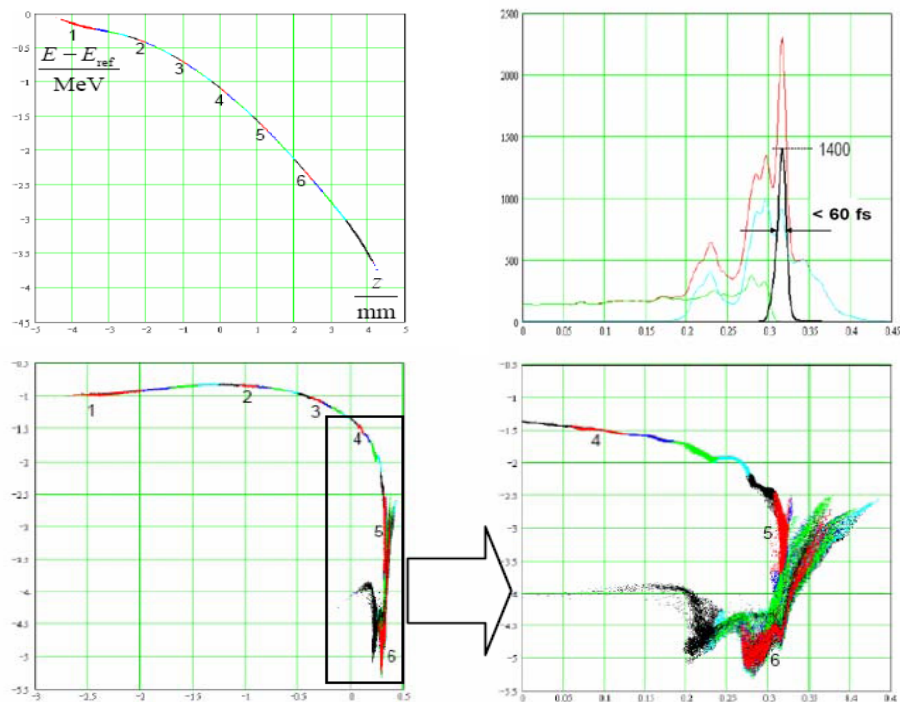


Figure 5: Roll-over compression at FLASH: Initial longitudinal phase space (upper left) and phase space in front of the undulator (bottom row) with a zoom into the head region of the bunch. The upper right picture shows intensity profiles for the different color-coded regions in phase space. The head of the bunch is to the right.

The upper right plot in Figure 5 shows the current distribution for the different color-coded regions in phase space. The black curve indicates *that* fraction of the particles located within an emittance smaller than the tolerable one ($\epsilon \leq 3 \cdot 10^{-6}$ m). This part of the bunch achieves a peak current of 1400 A and is only approx. 60 fs (FWHM) long. According to FEL simulation, such a beam would generate a radiation pulse of about 30 fs (FWHM) length, which is in good agreement with the pulse lengths measured at FLASH. The start-to-end simulations are also in good agreement with pictures of the projection of the bunch onto the longitudinal-horizontal plane, which are taken with the help of a transverse deflecting cavity (see next chapter).

3.1.3 Measurements and Simulation of Beam Slice Properties

Time-domain images of the bunch can be obtained from transverse deflection structures (TDS) [4]: A transverse kick with an amplitude correlated to the longitudinal position within the bunch is applied with an rf cavity and the longitudinal-transverse beam projection is observed on a downstream screen. In a FODO section or using quadrupole scans, the slice emittance can be measured. The projection on a screen in a dispersive section allows gauging of slice energy spread. The European XFEL design foresees multiple pairs of TDS to allow measurements at different locations along the injector and bunch compressor sections. At FLASH, an S-band TDS from SLAC is installed downstream of the linac and is routinely used for beam measurements. At

optimized conditions a rms resolution of about 20 fs is obtained. A typical TDS image is shown in Figure 6 (left), taken under SASE lasing conditions.

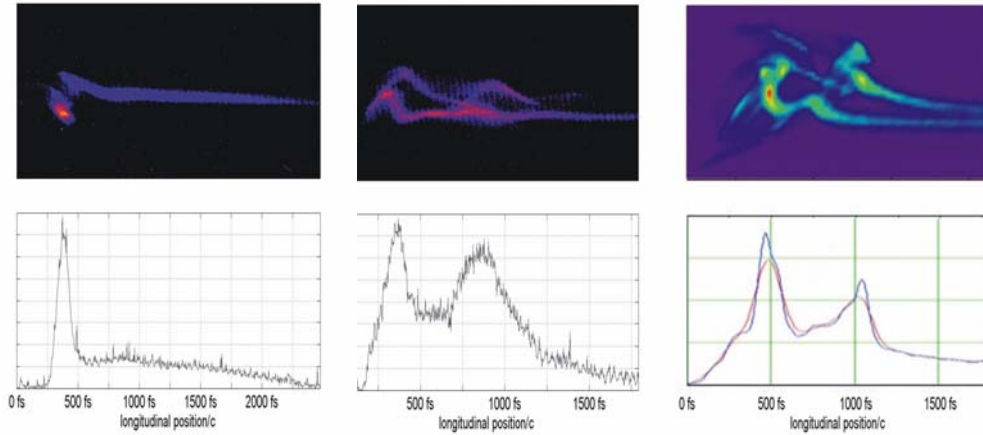


Figure 6: Longitudinal-horizontal projections (top row) and longitudinal charge distribution (bottom row) of a single bunch at FLASH. A measurement under SASE conditions is shown on the left, corresponding to the beam dynamics simulations in Figure 5. The middle and right images show measurement and simulation (right) for the case of an over-compressed bunch.

The leading spike of the bunch (as described in the previous chapter) with a width of about 100 fs is resolved. The two images to the right show a situation where the bunch is fully compressed in BC3. CSR effects and space charge fields lead to a splitting of the bunch head into two distinct spikes. This behaviour is predicted by start-to-end simulations when CSR and space charge are included up to energies of 500 MeV.

More quantitative comparisons of CSR simulations and measurements are possible with the dedicated experiment described in the following [5]. Coherent synchrotron radiation occurs when short bunches travel through bending fields. The CSR leads to an energy loss along the bunch.

The bunch is over-compressed in the first bunch compression chicane (BC2), leading to strong CSR effects only in the 2nd dipole, where the peak current reaches its maximum of about 1 kA. The bunch is decompressed afterwards, mitigating further self-fields effects downstream in the beam line. The energy loss throughout the bunch can be observed as a horizontal sag on the TDS screen (see Figure 7). The measurement is performed for different bunch charges to compare parameter dependencies with those predicted by theory and simulation.

The magnitude of the effect is expected to be up to 130 keV, leading to a trajectory offset of up to 1 mm after the bunch compressor chicane. With proper settings of the optics between the chicane and the TDS (involving 4 more accelerating modules, the 2nd bunch compressor, diagnostic and matching sections) the sag in the longitudinal-horizontal beam profile is of the same order. The upper row of Figure 7 shows a typical beam images for on- and off-crest cases (1 nC charge), while Figure 7 (bottom right) shows the simulated screen image and Figure 7 (bottom left) compares the measured and simulated slice centroid positions. The sag (i.e. the largest offset of the slices from the nominal position) is derived and plotted in Figure 8 for different bunch charges. The sag gets smaller for large bunch charges because the bunch length and the uncorrelated

energy spread at the entrance of the bunch compressor increases, so that the peak current during compression reaches its maximum around 1 nC (see Figure 8).

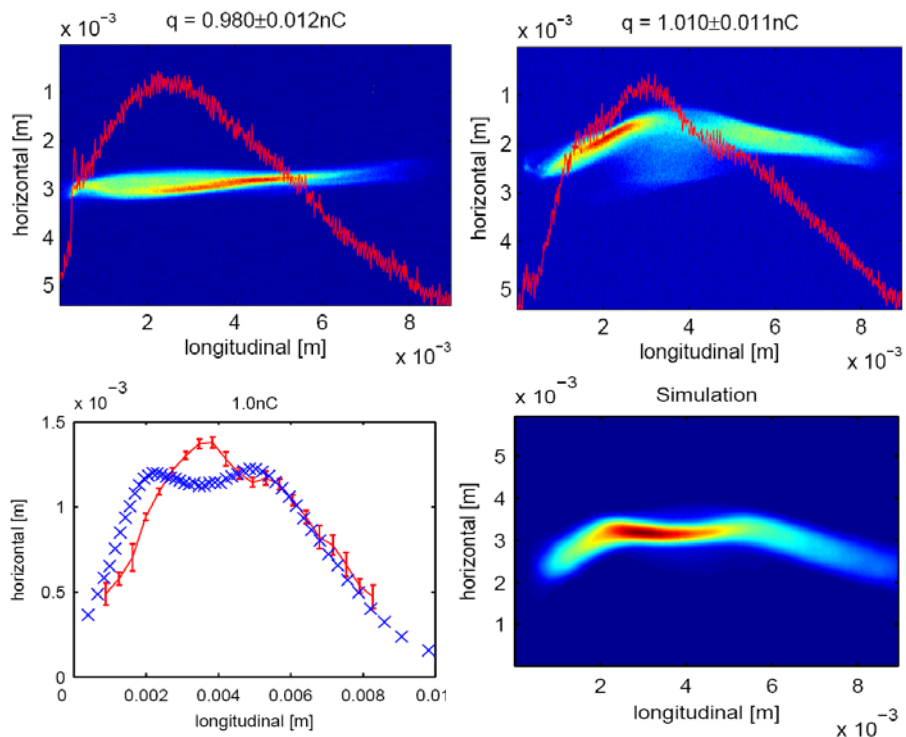


Figure 7: Longitudinal charge distribution within a single electron bunch of FLASH. Upper row: Image of the bunch on an observation screen, located downstream of the TDS. The left part shows the uncompressed case, while the right part shows the over-compressed beam as described in the text. Lower row: Simulated screen image (right) and comparison of simulated (blue) and measured (red) centroid positions (left).

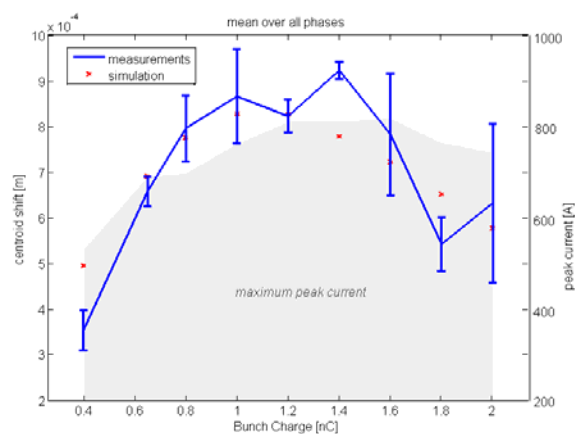


Figure 8: Maximum deviation of the slice centroids derived from measurements and simulations as shown in Figure 7 together with the variation of the maximum peak current.

3.1.4 Simulations of Micro-Bunching Instability and Possible Measurements

An initial bunch current ripple can be amplified by the following mechanism: a slight modulation of the initial bunch density profile produces an energy modulation due to longitudinal impedance, caused by CSR and space charge fields. In a bunch compression chicane, the energy modulation creates more density modulation. In a multi-stage bunch compression system, the gain of this amplification can be very high. A limiting factor for this mechanism is the uncorrelated energy spread. Figure 9 shows the increase of a slight intensity modulation out of the gun (red curve) to a strong modulation ($\sim 100\%$) at the exit of the bunch compression system (green curve).

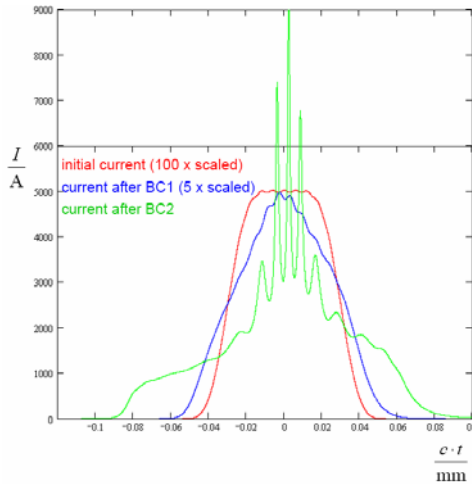


Figure 9: Increase of an initial modulation with 0.6 mm period length and 0.5 % amplitude throughout the European XFEL bunch compression system.

For the calculation of gain curves, a bunch with an initial charge modulation of wavelength λ is traced from the gun to the entry of the undulator. The gain is the amplification of the relative modulation amplitude in the simulation. The gain of the so called ‘CSR Instability’ was calculated with the 3-D code CSRtrack and found to be < 10 . Figure 10 shows gain curves for the space charge driven instability. The calculated gain at the expected small values for uncorrelated energy spread from the gun (rms < 2 keV) would be sufficient to start amplification from shot noise. With a ‘laser-heater’, an about two meter long magnet chicane with an undulator magnet which the electron beam traverses together with a laser beam, we can adjust the uncorrelated energy spread between its initial value and up to 40 keV. The induced initial energy spread is not Gaussian. Figure 10 shows the effect of that. We adjusted the R56 of the collimation section (here called ‘dogleg’) to zero, and increased the induced energy spread from 10 to 20 keV to reduce the shot noise induced current jitter at the undulator entrance to a tolerable value below 1 %.

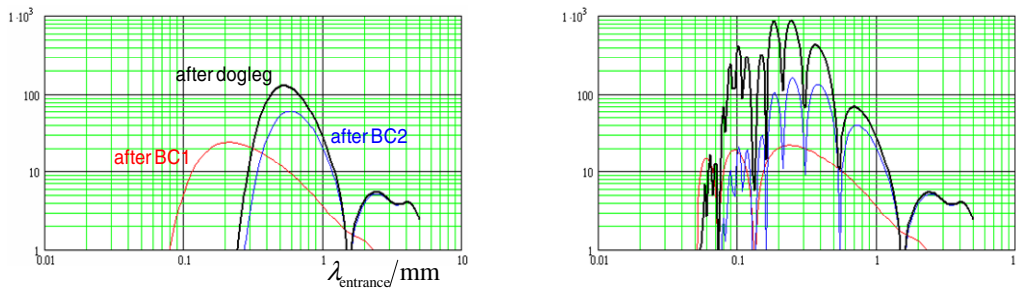


Figure 10: Gain curves for the space charge driven instability. Left side: Contributions of the sub-sections of the linac for an uncorrelated Gaussian energy spread of 10 keV. Right side: Overall gain for realistic laser heater induced energy spectrum of 10 keV rms.

The optimization of the bunch compression system parameters for operating stability tries to maximize the tolerances for rf jitter and to minimize the strength of the micro-bunching instability. The two Figures of merit which are evaluated when scanning the parameter space are on one hand the inverse of the tightest rf tolerance (e.g. the relative change in amplitudes and phases of fundamental and 3rd harmonic rf systems leading to 5% change in final peak current), and on the other hand the jitter in final peak current that micro-bunching instability generates by the amplification of initial shot noise.

The following Figure plots this quantity as a function of the R_{56} of the first chicane for different compression factor ratios (shown by different colors) and for each compression factor ratio, for four different phases of the rf between the chicanes (10, 20, 30 and 40 degrees). The laser heater supplies slice energy spread of about 20 keV rms.

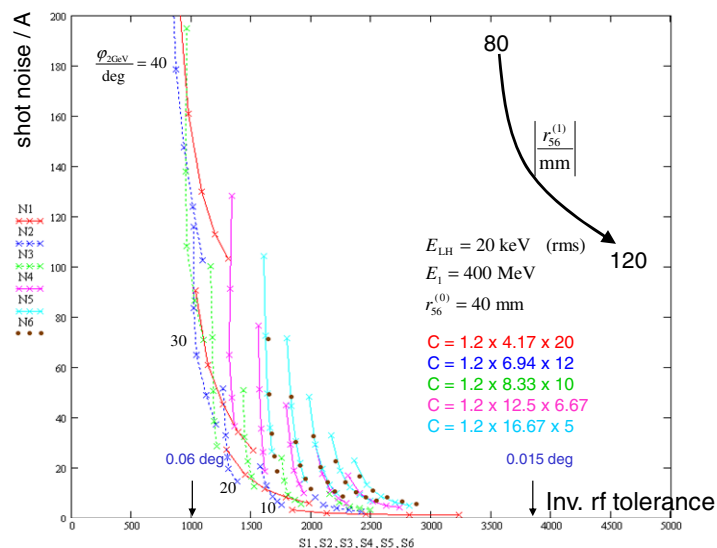


Figure 11: Jitter and final peak current versus inverse rf tolerance for different bunch compression system settings at the European XFEL.

The possible range of rf tolerance for this scan is between 0.015 and 0.06 degrees, the shot noise induced peak current fluctuations should be below 200 A ($\sim 5\%$).

According to the priorities of the users (for instance intensity stability vs. arrival time stability) we can choose the working point of the compression system.

At FLASH, coherent radiation diagnostics [6] might be used to observe micro-bunching effects. If the coherent radiation is spectrally resolved, information about the longitudinal form factor and thus the charge distribution can be obtained. For the typical bunch lengths between 10 fs and 100 fs, the corresponding range of wavelengths is in the far infrared from 10 μm to 300 μm . As shown in Figure 12, the wavelength spectra of coherent transition radiation from ideally compressed electron bunches strongly peak in the region below 200 μm , the position of the intensity maximum directly reflects the length of the current spike. If the bunch is distorted by collective effects, the wavelength spectrum exhibits characteristic substructures which could be used to get information on the strength and nature of the collective phenomena. Despite the fact that a direct reconstruction of the bunch shape from radiation spectra is impossible due to the missing phase information, the wavelength spectra reveal sufficient information to act as 'fingerprints' of the longitudinal bunch structure. As an example, Figure 13 shows a set of successively recorded spectra in the range of in the wavelength range 5-8 μm from coherent transition radiation at FLASH. The phase of the first rf module was changed from -4 to about -10 degrees. The intensity increases at certain off-crest phase angles. This might be an indication for micro-bunching on a few femtosecond scale. The complete analysis of this measurement requires the simulation of the beam dynamics and the response of the spectrometer for the over-compressed bunch with its sharp leading spike.

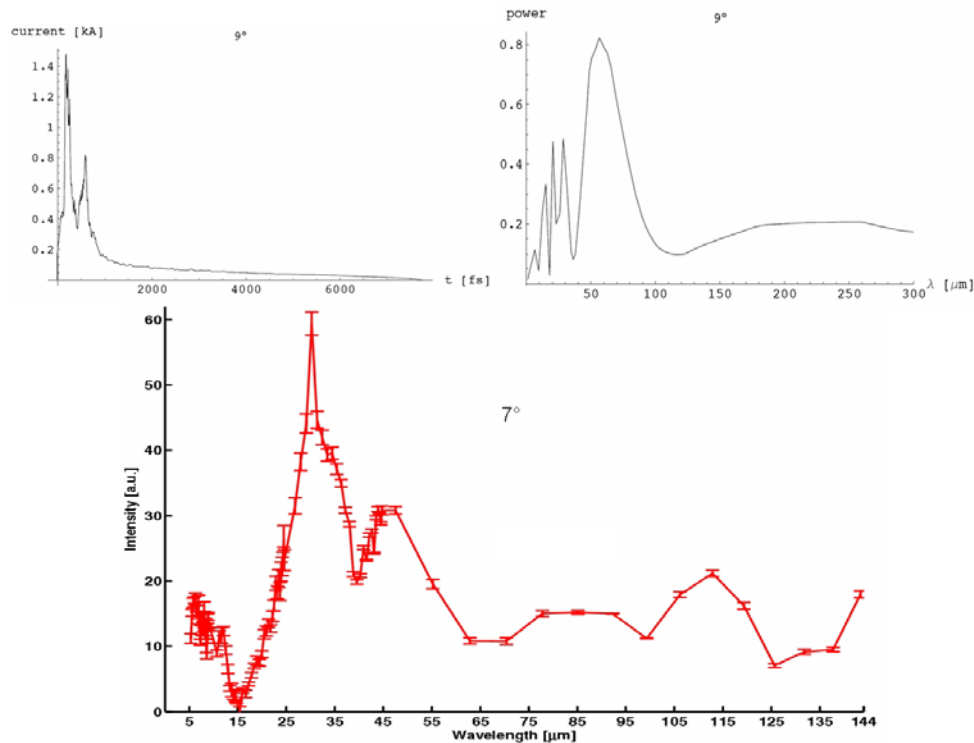


Figure 12: Simulated longitudinal beam profiles in time (upper left) and frequency (upper right) domain in comparison with a coherent radiation spectrum (lower).

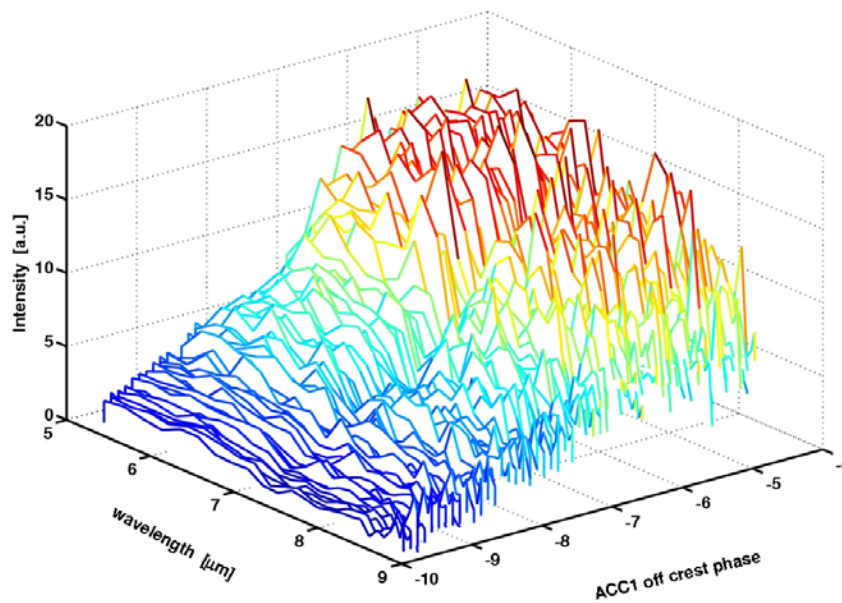


Figure 13: A set of successively recorded single shot spectra in the wavelength range 5-8 μm from coherent transition radiation at FLASH. The phase of the first rf module was changed from -4 to about -10 degrees.

3.1.5 References

1. Jörg Rossbach, "Results from FLASH", EPAC06, <http://cern.ch/AccelConf/e06/PAPERS/MOZBPA01.PDF>.
2. "The Technical Design Report of the European XFEL", http://xfel.desy.de/tdr/index_eng.html.
3. Martin Dohlus, "Modelling Of Space Charge And Csr Effects In Bunch Compression Systems", EPAC2006, <http://accelconf.web.cern.ch/AccelConf/e06/PAPERS/WEYFI01.PDF>.
4. Michael Roehrs et. al. , "Investigations Of The Longitudinal Electron Bunch Structure At The Flash Linac With A Transverse Deflecting Rf-Structure", FEL2006, <http://accelconf.web.cern.ch/AccelConf/f06/PAPERS/TUBAU06.PDF>.
5. Bolko Beutner, "Measurements of CSR Effects at FLASH", private communication.
6. Hossein Delsim-Hashemi et. al. , "Single-Shot Longitudinal Diagnostics With Thz Radiation At The Free-Electron Laser Flash", FEL2006, <http://accelconf.web.cern.ch/AccelConf/f06/PAPERS/THPPH018.PDF>.
7. "FEL Beam Dynamics Group Home Page", <http://www.desy.de/xfel-beam/>.

3.2 Free Electron Laser R&D at the NSLS SDL

X.J. Wang

Mail to: wangx@bnl.gov

<http://www.nsls.bnl.gov>, NSLS, BNL, Upton, NY 11973, USA

3.2.1 Introduction

The Source Development Laboratory (SDL) at the National Synchrotron Light Source (NSLS) of the Brookhaven National Laboratory (BNL) is a laser linac facility dedicated to linac based light source R&D and its applications. It is the only facility now in the world capable of performing laser seeded FEL experiments. The first lasing of the FEL @ 266 nm based on the high-gain harmonic generation (HG) was achieved in October 2002 [1]. Recent achievements at the SDL include the world record of 100 μ J THz generation, the first experimental characterization of the femto-second FEL pulse evolution in the superradiance regime [2], first observation of the frequency detuning effect in a high-gain FEL [3], first lasing of a 4th harmonic HG FEL and ESASE @ 200 nm in April 2006 [4].

In the rest of this report, we first describe the SDL facility and its capabilities, and then we discuss the recent FEL experiments performed at the SDL. In the last section of this report, we will also briefly discuss several FEL research opportunities at the SDL.

3.2.2 The NSLS Source Development Laboratory (SDL)

The NSLS has a long tradition in FEL R&D: pioneering work on both SASE and HG FELs was performed at the NSLS [5-8], the BNL photocathode RF gun developed by the NSLS staff has been widely adopted around the world, and it was used to achieve the first saturation in both SASE and HG FELs in the US. The NSLS established the SDL in the mid 1990s to experimentally demonstrate key technologies for future linac based light sources, such as high brightness electron beam generation and laser seeded FELs.

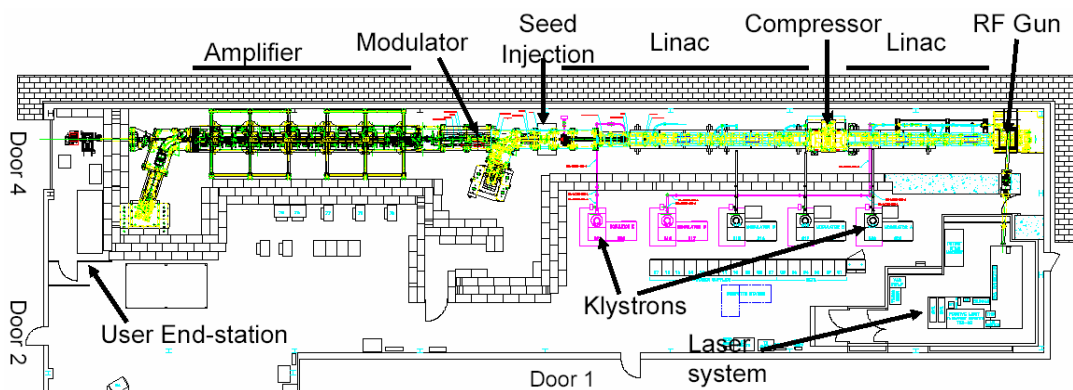


Figure 1: The NSLS SDL layout.

The SDL is shown schematically in Fig. 1. It features a high-brightness electron accelerator and a Ti:Sapphire laser system. The SDL accelerator system consists of a

1.6-cell BNL photo injector driven by a Ti:Sapphire laser system, and a five-section 2856 MHz SLAC-type traveling wave linac that is capable of producing a 300 MeV electron beam. The facility's magnetic chicane bunch compressor produces sub-picosecond long electron bunches with a peak current of a few hundred amperes.

One of the unique features of the SDL laser system is that it was designed in such way that a single laser system is used to drive both the photocathode RF gun and to provide a seed laser pulse for the FEL. This setup makes it possible to achieve sub-ps timing jitter between the seed laser and the electron beam. The SDL Ti:Sapphire laser system consist of an RF synchronized 100 fs oscillator and an chirped pulse amplifier (CPA) system. The 100 fs pulse generated by the Ti:Sapphire oscillator is stretched before being sent to the amplifiers. The SDL laser amplifier system is made up of a regenerative amplifier and two two-pass amplifiers and is capable of generating 50 mJ output. The amplified pulse is divided into two pulses before the final compression. One pulse is compressed down to 4-10 ps (FWHM) and frequency tripled to 266 nm for driving the photocathode RF gun, and the other can be stretched from 100 fs to 6 ps (FWHM) for the laser seeded FEL and other applications.

Table 1 summarizes the basic electron beam and FEL parameters. The SDL FEL undulator system consists of three magnets: the 10 meter long NISUS magnet serves as the FEL amplifier, a 10-period modulator magnet (8 cm period) and a 30 cm long dispersion magnet. The NISUS undulator consists of 16 sections, and each section has an independent gap control. The beam focusing and steering within each section can be adjusted using four wires located at the corners of the vacuum chamber. The modulator is used to modulate the electron beam energy through the inverse free electron laser (IFEL) interaction. The energy modulation of the electron beam is converted into spatial modulation by the dispersion magnet.

Table 1: Summary of the SDL accelerator and FEL parameters.

Parameters			
Electron Energy (MeV)	300	Peak Current (A)	300
Charge (nC)	1	Emittance (mm-mrad)	3 - 5
Seed laser λ_S (nm)	266 -800	Seed laser pulse length (FWHM) (ps)	0.15 - 6
NISUS Period λ_U (cm)	3.89	NISUS length (m)	10
NISUS K	1.1	Dispersion R_{56} (mm)	5
Modulator Period λ_U (cm)	8	Modulator K	0 - 2.5

3.2.3 Recent SDL FEL Experiments

After successfully commissioning of the SDL in early 2000, experiments related to the wide range of the beam physics and FELs were performed. In this section, we highlight several recent FEL experiments and the first chemical science experiment using the FEL light at the SDL.

3.2.3.1 Laser Seeded FEL Amplifier and Femto-second FEL Pulse Evolution in the Superradiance Regime

Recent success with single pass FEL amplifiers and energy recovery linacs has made it feasible to explore using laser seeded FEL amplifiers for directed energy applications [9-10]. For directed energy applications [10] a MW-class FEL at near-IR wavelengths is required. Major challenges to realizing a MW-class laser seeded FEL are high-brightness electron beams and FEL amplifier performance. An experimental program was initialized at the SDL to demonstrate the critical FEL amplifier technologies for high average power applications; especially to investigate various schemes of improving the FEL efficiency and controlling of the FEL output radiation using a pinched e-beam technique [10]. We have experimentally demonstrated more than 3 orders of magnitude gain with an 800 nm seed. By taking advantage of the tapering capability of the NISUS undulator, we are studying the FEL efficiency and optical beam quality as a function of the undulator tapering.

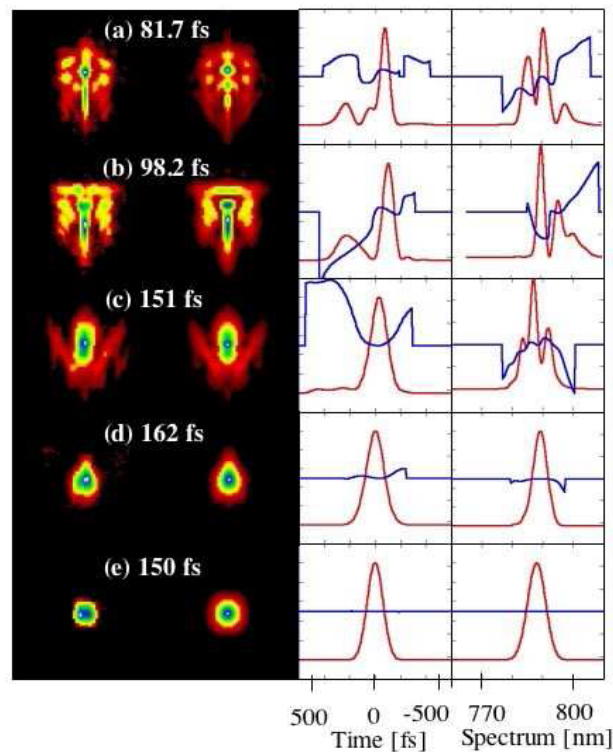


Figure 2: Femto-second seed laser and FEL pulse FROG images, bottom row is the seed laser FROG image [2].-

One of the exciting recent experimental results from the SDL is for the first time we have experimentally characterized femto-second FEL pulse evolution in both the exponential gain and the superradiance regimes [2]. With a 150 fs (FWHM) seed laser, we observed femto-second FEL pulse length growth in the exponential gain regime, and pulse length reduction in the superradiance regime (Fig.2). We also characterized the FEL energy growth beyond saturation of the exponential gain regime.



Figure 3: The experimental setup of the 4th harmonic HGHG.

3.2.3.2 Laser Seeded FEL - 4th harmonic HGHG and ESASE

As part of the recent electron beam energy upgrade [11], extensive modification of the HGHG modulator was done to make it possible to achieve HGHG at harmonics as high as seven. After the successful lasing of SASE at 193 nm, the electron beam energy was tuned to 202.5 MeV for the 4th harmonic HGHG with the seed laser at 795 nm (Fig. 3). With the seed laser pulse length at about 2 ps (FWHM) and a peak power of 50-100 MW, we successfully observed the first lasing of the 4th harmonic HGHG at 199 nm (Fig. 4).

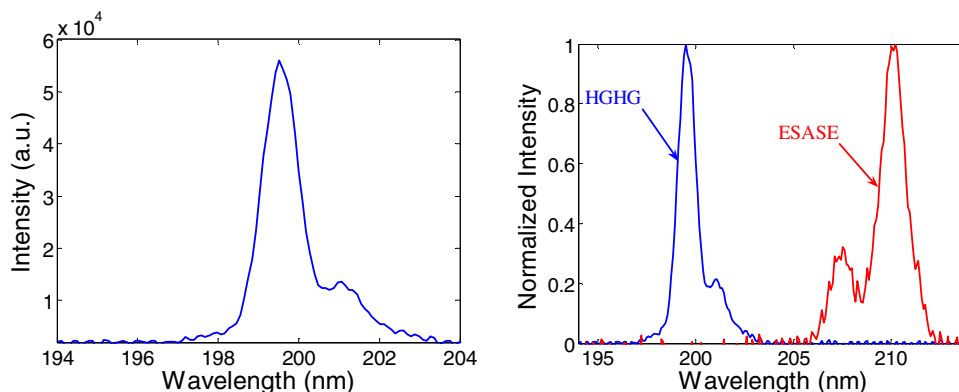


Figure 4: The spectrum of the 4th harmonic HGHG (left) and comparison to ESASE.

Taking advantage of the large tuning range of the HGHG modulator, we moved the electron beam energy to 197 MeV to demonstrate ESASE [12, 13]. The resonance wavelength of the HGHG radiator at 197 MeV is about 210 nm, which is beyond the seed laser bandwidth. We successfully observed first lasing of a laser enhanced SASE FEL at the 210 nm (Fig. 4) using the same HGHG arrangement (Fig.3). The intensity of the ESASE is a couple orders of magnitude stronger than SASE without the seed laser.

3.2.3.3 FEL Light for Chemical Dynamics

After successfully lasing at 266 nm with 800 nm laser seeding, both the second and third harmonic HGHG FEL beams were experimentally characterized using a vacuum

monochromator. The pulse energy for both harmonics (133 and 89 nm, respectively) was measured to be about 1 μ J, which is about one percent of the fundamental value at 266 nm.

The first chemical science experiment on ion pair imaging was successfully completed in 2003, it used the HGHG's third harmonic beam (89 nm) to study the super excited states of methyl fluoride [14]. Methyl fluoride is a highly flammable gas. Arthur Suits and his group from the BNL chemistry department aimed the 89 nm ultraviolet beam from the SDL FEL at a beam of methyl fluoride gas, the gas molecules each absorbed a single energetic photon, which caused them to separate, or dissociate, into their positive and negative fragments, called ion pairs. Velocity-mapped ion images of the fluoride ion, revealed a low translational energy, implying a very high internal excitation in the molecule's methyl cation cofragment

3.2.4 Future FEL R&D at the NSLS SDL

To explore opportunities for future experiments on FELs and beam physics at the SDL, the SDL Beam Physics and FEL Research and Development Workshop (<http://www.nsls.bnl.gov/organization/Accelerator/highlights.htm>) was held at BNL in February 2004. The SDL is an ideal test bed for developing the next generation of FEL experiments.

The near term focus at the SDL is to continue the laser seeded FEL amplifier experimental program. We will investigate the frequency detuning and undulator tapering effects on the efficiency, FEL spectrum and mode distributions. We will also study the evolution of the nonlinear harmonics for a tapered undulator.

We also intend to continue to explore the unique features of the SDL to study various schemes of improving SASE performance and demonstrate key technologies for future x-ray FELs that would be based on the HGHG concept. By taking advantage of the NISUS undulator tapering capability, we could investigate the tapering effect on the SASE FEL. The SDL is well positioned to explore various ideas of generating ultra-short SASE FEL pulses; emittance spoiler [15] and femto-second electron pulses [16] are two prime examples.

For the laser seeded FEL we will explore using the seed laser and electron beam energy chirp to control the FEL output spectrum properties. We will also continue to push the frontier of the HGHG FELs. A cascaded HGHG FEL and a higher harmonic ($n>5$) HGHG FEL are critical for the realization of a HGHG X-ray FEL.

3.2.5 Acknowledgement

We would to thank the BNL director's office and the NSLS for supporting the SDL over the last decade and the contributions from many BNL and NSLS colleagues are gratefully acknowledged. The work reported here is supported by the Office of Naval Research (ONR) and the U.S. Department of Energy under the Contract No. DE-AC02-98CH10886.

References

1. L.H. Yu, et al, Phys. Rev. Lett. 91, 074801-1 (2003).
2. T. Watanabe et al, Phys. Rev. Lett. 98, 034802 (2007).
3. T. Watanabe et al, Proceedings of FEL 2006, BESSY, Berlin, Germany, 190 (2006).
4. X.J. Wang et al, Proceedings of FEL 2006, BESSY, Berlin, Germany, 18 (2006).
5. R. Bonifacio, C. Pellegrini and L.M. Narducci, Opt. Comm., 373 (1984).
6. J.B. Murphy, C. Pellegrini and R. Bonifacio, Optics Comm., 197 (1985).
7. J.M. Wang and L.H. Yu, NIM A 250, 484 (1986).
8. L.H. Yu, Phys. Rev. A 44, 5178 (1991).
9. D.C. Nguyen and H.P. Freund, NIM A507, 120 (2003).
10. P. Sprangle, et al, IEEE J. Quantum Electronics, 40 1739 (2004).
11. X. J. Wang et al, Proceeding of the 2004 FEL conf., Trieste, Italy, 209-211 (2004).
12. Y. Liu et al, Phys. Rev. Lett. 80, 4418 (1998).
13. A.A. Zholents, Phys. Rev. ST Accel. Beams 8, 040701 (2005).
14. W. Li et al, Phys. Rev. Lett. 92, 083002-1 (2004).
15. P.J. Emma et al, Phys. Rev. Lett. 92, 074801 (2004).
16. X.J. Wang and X.Y. Chang, NIM A 507, 310 (2003).

3.3 FEL Design Studies at LBNL: Activities and Plans

J. Corlett, W. Fawley, S. Lidia, H. Padmore, G. Penn, I. Pogorelov, J. Qiang, F. Sannibale, J. Staples, C. Steier, M. Venturini, W. Wan, R. Wilcox, A. Zholents

Mail to: jncorlett@lbl.gov, Lawrence Berkeley National Laboratory,
1 Cyclotron Road, Berkeley, CA 94720, USA

3.3.1 Introduction

LBNL staff are currently pursuing R&D for future x-ray FELs, and participate in two FEL construction projects. Our strategy is to address the most fundamental challenges, which are the cost-drivers and performance limitations of FEL facilities. An internally funded R&D program is aimed at investigating accelerator physics and technologies in three key areas:

- Theoretical study, modelling, and experimental development of low emittance, high quantum efficiency cathodes
- Theoretical study, modelling, and experimental development of low emittance, high quantum efficiency cathodes
- Design studies of electron beam delivery systems, including emittance manipulations, high-resolution modelling of 6-D phase space, and low-emittance beam transport
- Design studies of optical manipulations of electron beams for seeded and SASE FELs, providing short x-ray pulses of variable duration, synchronous with the seed and pump laser sources, and also long transform-limited pulses with a narrow bandwidth. Design studies of means for production of attosecond x-ray pulses at various wavelengths.

We are collaborators in the FERMI@Elettra seeded FEL facility under construction at Sincrotrone Trieste, Italy, participating in accelerator design and FEL physics studies, and mechanical and electrical engineering [1, 2].

We are participating in the LCLS project at SLAC [3, 4], implementing our design of stabilized timing and synchronization systems. Here we outline our long-term objectives, and current activities.

3.3.2 A High Repetition Rate FEL Facility

The LBNL program in R&D toward advanced FELs addresses the scientific needs of the future, such as understanding the dynamics and “emergent” properties of complex systems arising from correlated interactions between charge carriers and constituent atoms. Direct quantitative measurements of the electronic and atomic structural dynamics on the ultrafast time scale of the underlying correlations will be indispensable in achieving new insight into the complex properties emerging from correlated phenomena in atoms, molecules, and solids (see for example references [5-8] for scientific conferences and workshops motivating these requirements). The fundamental time scales span:

- ~ picoseconds, characteristic of conformational relaxations in molecular systems and electron-lattice energy transfer times in crystalline solids.
- ~100 femtoseconds, characteristic of atomic vibrational periods in molecules and solids.
- ~10 femtoseconds, characteristic of electron-electron scattering times in solids.
- ~100 attoseconds, characteristic of electron-electron correlations and valence electron motion.

Answering questions in these areas will require new tools, complementing the existing and planned synchrotron radiation facilities. To address these needs, we suggest a new user facility equipped with an array of task-designated FELs, wherein each FEL may be configured to operate in a different mode, independently of the other FELs. Each FEL will have independent control of wavelength and polarization, and optical manipulations of the electron beam will be used to produce seeded x-ray pulses with control of pulse duration, offering flexibility and versatility to many experiments simultaneously [9-14]. High repetition rate and high average photon flux are essential to many experimental techniques. To meet these needs, we envision a facility comprised of a high bunch repetition rate (~MHz), low-emittance and low energy spread RF photocathode electron gun, and a low-energy (~2 GeV) superconducting linac, feeding an array of approximately ten FELs through an elaborate beam switchyard. Each FEL operates independently at a repetition rate of ~100 kHz. Photon energies would span approximately 10 eV to 1 keV, with the possibility to reach higher photon energy at the expense of reduced photon flux. A variety of seeded and SASE FELs provide the above described output radiation with a peak power from a few hundred megawatts to a few gigawatts. The temporal coherence available in the seeded FEL allows close to transform-limited x-ray pulses, resulting in a narrow bandwidth signal that could possibly be utilized in experiments without a monochromator. Techniques have also been developed to use optical manipulations of the electron bunch to produce x-ray pulses of a few hundred attosecond duration [12-14].

Figure 1 shows a schematic of a multi-user FEL facility concept. The major components are: (1) a low-emittance, low energy spread RF photocathode electron gun operating in CW mode at ~60 MHz, providing electron bunches at up to MHz repetition rate, (2) hardware for manipulating the electron-beam emittance in preparation for the FEL process, (3) a CW superconducting RF linac, (4) a beam-switching system, (5)

multiple independent FELs and beamlines, and (6) lasers for the photocathode gun, FEL seeding, pump-probe experiments, and timing and synchronization. A low-energy linac is used to minimize costs. The electron beam is dumped at the end of each FEL as we do not currently believe the added cost and complexity of electron beam recirculation and energy recovery is worthwhile for a machine of modest electron beam power.

3.3.3 Current R&D Activities

Efficient radiation at wavelengths down to 1-nm, with an electron beam energy of approximately 2 GeV, requires a bright electron beam with low-emittance, low energy spread, and high peak current. This, together with the requirement of high-repetition rate, drives the need for a vigorous R&D program.

3.3.3.1 VHF Photo-gun

We are developing a design for a high-brightness, high-repetition rate electron gun that uses a normal conducting RF structure in the VHF range, between 50 to 100 MHz. The gun cavity has quarter-wave coaxial geometry, which is a mature RF technology similar, for example, to that employed in the NSLS VUV ring accelerating cavities. The lower frequency results in a larger cavity compared to the more common designs operating at ~ 1 to ~ 3 GHz. A significant benefit of using a larger cavity is a dramatic

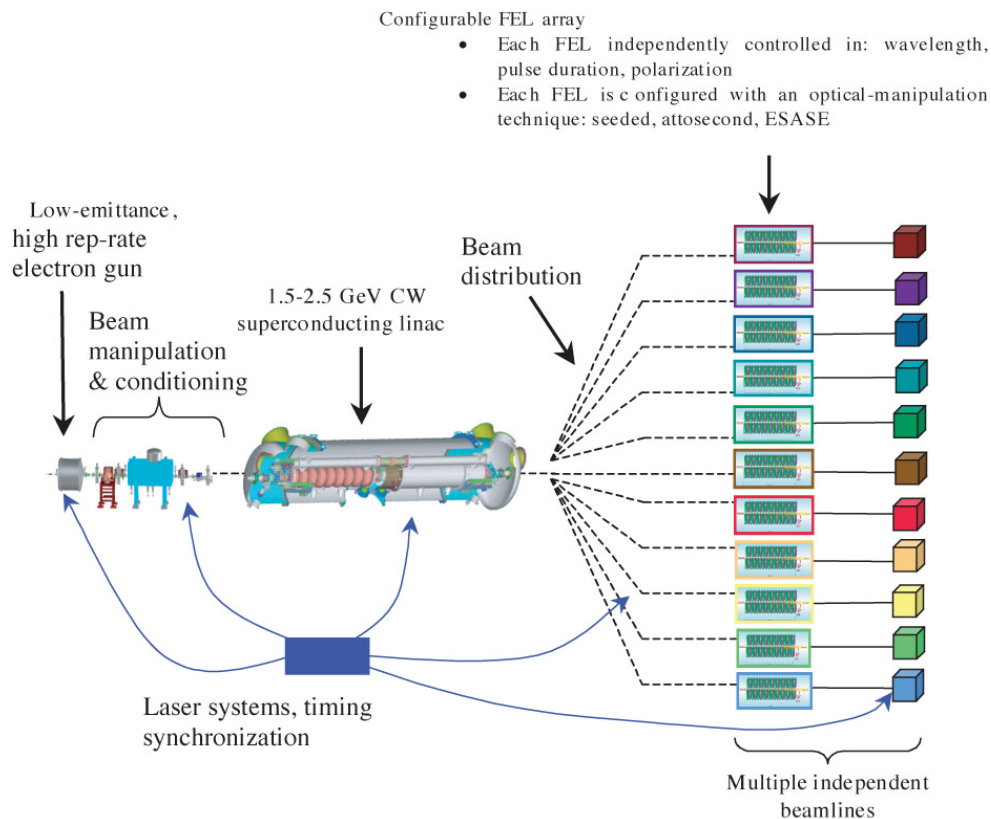


Figure 1. Schematic of a light source facility based on a high-pulse-repetition-rate, seeded FEL.

reduction of the power density on the cavity walls, which allows CW operation of the gun, and thus a bunch repetition rate of up to the RF frequency (dependent on photocathode-laser time structure). Calculations show that a VHF gun can achieve accelerating gradient at the cathode of approximately 20 MVm^{-1} . Table 1 shows example parameters for a VHF photocathode cavity.

3.3.3.2 Photocathode Design

The aim of this program is to improve the beam quality through development of a cathode that produces a beam with very low thermal emittance. We also aim to increase the quantum efficiency up to the point at which conventional laser technology can be used to produce tailored electron pulses at MHz repetition rate. As a first step, we have investigated metallic photocathodes, and determined that photo-current at the very low photon energies typically used is dominated by surface states. This directly has led to a prediction of the minimum transverse momentum, and to a direction for producing lower emittance through use of other crystalline surfaces. These studies will be extended to metallic systems in which the surface electric field is manipulated using plasmonic interactions, and to semiconductor systems. The latter have the advantage that some

Table 1: Example parameters for a VHF coaxial cavity

<i>Parameter</i>	<i>Unit</i>	<i>Value</i>
Frequency	MHz	65
Gap Voltage	MV	0.5-1.0
Unloaded Q		3.5×10^4
Effective Gap Length	cm	4
Range of field in planar gap	MV/m	15-25
Cavity length	m	1
Cavity diameter	m	1.4
Inner conductor diameter	m	0.3
RF power for 0.75 MV on gap	kW	65
Peak wall power density	W/cm^2	7

degree of thermalization can take place, resulting in colder emission. This work is based on understanding the near Fermi surface electronic structure, through use of very low energy photoelectron spectroscopy, and through electronic structure modeling.

3.3.3.3 Electron Beam Delivery Systems

Production of electron beams for x-ray FELs is a difficult and elaborate process consisting of the electron generation, acceleration, compression, and transport. A significant understanding of the underlying physics such as space charge effects, wake-fields, and coherent synchrotron radiation (CSR) has been gained over the past decade [15-19]. Radical improvements in the electron beam quality may be needed to be able to build a cost effective VUV-soft x-ray FEL facility. We are developing understanding of the beam phase space evolution, and means to control and manipulate emittances, using both theoretical approaches and high-resolution numerical modeling. We have developed a parallel code suite, IMPACT [20-21], for advanced supercomputer modeling

of high intensity, high brightness beams in rf linacs and photoinjectors. An example is provided by 100 million macroparticle simulations of the microbunching instability, simulations that cannot be sensibly performed on today's single-processor computers. Figure 2 shows a multiprocessor simulation using IMPACT for the FERMI@Elettra linac. The figure shows the sensitivity to macroparticle number of the evolution of the microbunching instability. We are augmenting our present particle loading approach with “quiet-start” techniques, and in parallel we are also developing a direct Vlasov-Maxwell solution.

Following the accelerator, electron beams will be switched into each FEL in the array, in a time-sliced manner dependent on user needs. Techniques for switching the electron beam between FEL's are being studied, using pulsed ferrite magnets in a linear array, selectively switching the beam into FEL beamlines.

3.3.3.4 FEL Design

Our goal is to develop design concepts for flexible photon beam performance, based on a number of FEL configurations, fed by a low-energy electron accelerator, that would provide experimentalists a variety of configurations, including high flux time-domain pulses of fs to 0.1 fs duration, and high resolution frequency-domain outputs with close to transform limited meV bandwidth.

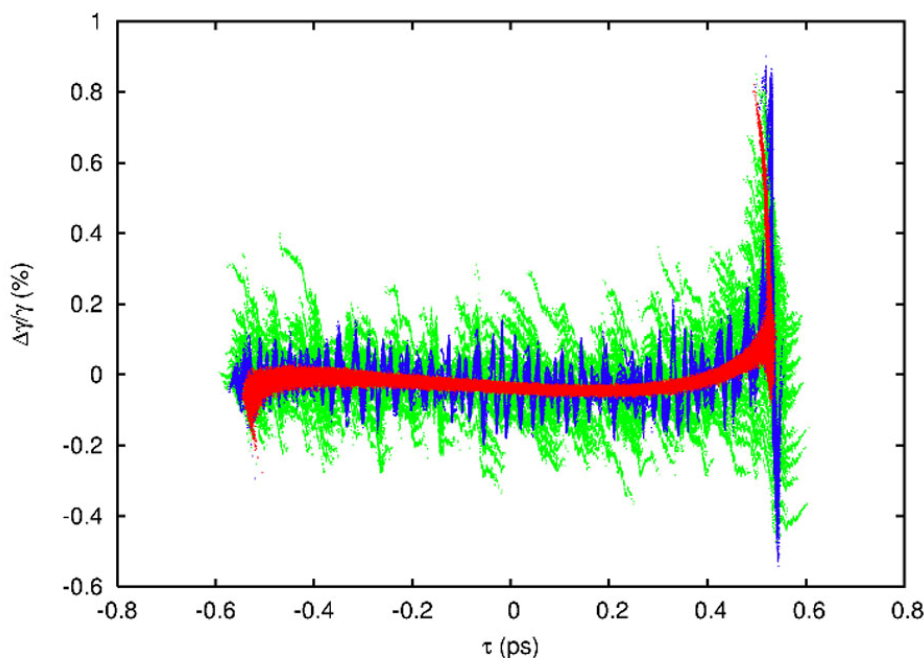


Figure 2. Longitudinal phase space distribution calculated at the end of the FERMI@Elettra linac using 2 million (green) and 100 million (blue) macroparticle IMPACT simulations. Red shows the model with no space-charge or CSR effects.

SASE, seeded, regenerative amplifier, and oscillator techniques are being simulated and developed, using GINGER and GENESIS simulation codes. Start-to-end modeling of the electron beam is critical in determining realistic FEL performance capabilities.

3.3.4 LBNL Support for the FERMI@Elettra Project

LBNL accelerator physicists and engineers participate in design and optimization studies for a seeded FEL facility, to be built at Sincrotrone Trieste, as described elsewhere in this newsletter. A novel feature will be the ability to provide both ultrafast (100 fs and shorter) photon pulses for time-domain exploration, and also longer pulses of 500-1000 fs duration with very high temporal coherence. The latter will result in photon beam bandwidths of a few meV, providing extremely high resolving power directly from the FEL.

The LBNL team participates in the design of the various systems from the high-brightness photocathode RF gun, through the main linac accelerating sections, bunch compressors, beam switch yard between two FELs, optical seeding and modulation of the electron beam, and photon production in the FELs. We also contribute to design of ultra-stable timing and synchronization systems, diagnostics and instrumentation, RF power systems, low-level RF systems, and start-to-end modeling.

3.3.5 References

1. The FERMI@Elettra FEL Project, <http://www.Elettra.trieste.it/FERMI/>
2. C. Bocchetta et al., "FERMI@Elettra: A seeded FEL Facility for EUV and soft x-rays," Proceedings of the 28th Int'l FEL Conf. (Berlin, Germany, Aug. 27-Sept. 1, 2006), <http://www.bessy.de/fel2006/proceedings/PAPERS/MOPPH054.PDF>.
3. The Linac Coherent Light Source, <http://www-ssrl.slac.stanford.edu/lcls/>
4. LCLS Conceptual Design Report, SLAC-R-593 (2002)
5. Workshop on Ultrafast Time-resolved Soft X-ray Science (Zeuthen, Germany, April 2005). For a workshop report, see: Synchrotron Radiation News, 18, p.2-6, 2005, and the related document Visions of Science (and references therein) available at <http://www.bessy.de/publicRelations/publications/files/sc.pdf>
6. Ultrafast X-rays 2004 (San Diego, CA, USA, April 2004); <http://ultrafast2004.lbl.gov/>
7. Ultrafast Science with X-rays and Electrons (Montreux, Switzerland, April 2003); <http://sls.web.psi.ch/view.php/science/events/uscience03/index.html>
8. New Opportunities in Ultrafast Science using X-rays (Napa, CA, USA, April 2002); <http://www-esg.lbl.gov/Conferences%20&%20Meetings/ultrafast/>
9. A.A. Zholents, "Method of an enhanced self-amplified spontaneous emission for x-ray free electron lasers," Phys. Rev. Special Topics: Accelerators and Beams 8, 040701 (12 April 2005); <http://dx.doi.org/doi:10.1103/PhysRevSTAB.8.040701>
10. Saldin, E.L., Schneidmiller, E.A., and Yurkov, M.V., Optics Comm. 237, 1-3 (2004), pp. 153-164; <http://dx.doi.org/doi:10.1016/j.optcom.2004.03.070>
11. Saldin, E.L., Schneidmiller, E.A., and Yurkov, M.V., "A new technique to generate 100 GW-level attosecond X-ray pulses from the X-ray SASE FELs," Optics Comm. 239 (2004), pp. 161-72; <http://dx.doi.org/doi:10.1016/j.optcom.2004.05.0244>
12. A.A. Zholents and G. Penn, "Obtaining attosecond x-ray pulses using a self-amplified spontaneous emission free electron laser," Phys. Rev. Special Topics: Accelerators and Beams 8, 5 (May 2005), 050704; <http://dx.doi.org/doi:10.1103/PhysRevSTAB.8.050704>
13. A.A. Zholents and W.M. Fawley, "Proposal for intense attosecond radiation from an x-ray free-electron laser," Phys. Rev. Letters 92, 22 (June 2004), 224801;
14. E.L. Saldin, E.A. Schneidmiller, and M.V. Yurkov, "Self-amplified spontaneous emission FEL with energy-chirped electron beam and its application for generation of attosecond x-ray pulses", PRSTAB 9, 050702 (2006)
15. M. Borland, Y.C. Chae, P. Emma, J.W. Lewellen, V. Bharadwaj, W.M. Fawley, P. Krejcik, S.V. Milton, H. Nuhn, R. Soliday and M. Woodley, "Start-to-end simulation of self-amplified spontaneous emission free electron lasers from the gun through the undulator", NIM A, Vol. 483, pp. 268-272 (2002).

16. E.L. Saldin, E.A. Schneidmiller and M.V. Yurkov, "Klystron instability of a relativistic electron beam in a bunch compressor", NIM A, Vol. 490, pp. 1-8 (2002).
17. S. Heifets, G. Stupakov and S. Krinsky, "Coherent synchrotron radiation instability in a bunch compressor", Phys. Rev. ST Accel. Beams, Vol. 5, 064401 (2002).
18. Z. Huang and K.-J. Kim, "Formulas for coherent synchrotron radiation microbunching in a bunch compressor chicane", Phys. Rev. ST Accel. Beams, Vol. 5, 074401 (2002).
19. K. Bane, "Wakefields of Sub-Picosecond Electron Bunches", [SLAC-PUB-11829](#), 2006.
20. J. Qiang and R. Ryne, "Parallel 3D Poisson solver for a charged beam in a conducting pipe," Computer Physics Communications 138, 18 (2001).
21. J. Qiang, R.D. Ryne, S. Habib, and V.K. Decyk, "An object-oriented parallel particle-in-cell code for beam dynamics simulation in linear accelerators," J. Computational Phys. 163, 434 (2000).
22. J.M. Byrd, L. Doolittle, A. Ratti, J.W. Staples, and R. Wilcox, "Timing distribution in accelerators via stabilized optical fiber links," Proceedings of the 2006 Linac Conference (Knoxville, TN, USA, August 2006).

3.4 FERMI@Elettra

Carlo J. Bocchetta

on behalf of the FERMI team

Mail to: carlo.bocchetta@elettra.trieste.it

Sincrotrone Trieste, Trieste I-34012, Italy

3.4.1 Introduction

The FERMI project at the Elettra Laboratory of Sincrotrone Trieste will be a national and international user facility for scientific investigations with high brilliance X-ray pulses of ultra-fast and ultra-high resolution processes in material science and physical biosciences. The underlying technology of the new facility is the Free Electron Laser (FEL) employing a master-oscillator-power-amplifier configuration with high gain harmonic cascades of undulators. This configuration with an external laser driving the FEL process is particularly suitable for pump/probe synchronization at time scales well below a picosecond. The new facility will consist of a linear accelerator and two initial FEL chains delivering photon beams to five beamlines. New infrastructures including a new experimental hall will be built in the complex environment of a multi-beamline user facility provided by the Elettra synchrotron light source.

The FERMI project utilizes a normal conducting S-band linear accelerator, part of which is the current injector of the Elettra storage ring, and a new electron source based on photo-injector technology. In the near future, with the start of operation of a new booster ring as the Elettra injector, the existing linac will be upgraded to become the FEL driver. Seven accelerating sections will be added to the linac bringing the energy to 1.2 GeV. At this energy, and with state-of-the-art undulator technology, the FEL will operate in the 100-40 nm energy region in the initial phase (FEL-1) and down to 10 nm in a subsequent phase (FEL-2). Table 1 lists the basic parameters of the electron beam and of the FEL radiation at 40 nm (FEL-1) and 10 nm (FEL-2).

Table 1: Nominal electron beam and FEL parameters.

<i>Parameters</i>	<i>Value at 40 nm</i>	<i>Value at 10 nm</i>	<i>Units</i>
Electron beam energy	1.2	1.2	GeV
Peak current	800	500	A
Emittance (slice)	1.5	1.5	μm , rms
Energy spread (slice)	150	150	keV
Bunch duration	700	1400	fs, FWHM
Repetition rate	50	50	Hz
FEL peak power	2.5	0.6	GW
FEL pulse duration	200	400	fs, FWHM
# of photons/pulse	1014	1012	
Bandwidth	17	4	meV

FERMI has been designed to have peak brightness orders of magnitude greater than third generation sources, full transverse coherence, (close to) transform limited bandwidth, pulse lengths of the order of a picosecond or less, variable polarization and energy tuneability. The coherence properties will open up new perspectives for single shot imaging, allowing the study of chemical reactions dynamics and other phenomena. The high peak power will allow the study of non-linear multi-photon processes in a regime never explored before. The short pulse duration will open the door to visualizing ultra-fast nuclear and electronic dynamics. The high peak power enables studying dilute samples that are of paramount importance in atmospheric, astrophysical and environmental physics as well as the characterization of nano-size materials.

3.4.2 Overall Layout

Figure 1 shows the layout of the facility. The accelerator and FEL complex is composed of a photo-injector and two short linac sections, generating a high brightness electron beam accelerated to 100 MeV, a main linear accelerator, where the electron beam is time-compressed and accelerated to 1.2 GeV, an electron beam transport system to the FEL undulators, an undulator hall with side gallery and photon beam transport lines from the undulators to the experimental area.

New constructions include a backward extension of the linac tunnel of 80 m to make room for the photo-injector, new accelerating sections and the first bunch compressor. At its downstream end, 30 m of the tunnel will be cleared out to accommodate additional accelerating sections and the electron beam transfer lines to a new underground undulator hall. While only two FELs are envisaged initially, the transverse dimension of this hall allows installation of up to four undulator chains side-by-side. Finally an experimental hall, also partially underground, will house the FEL radiation beamline optics and the experimental hutches, including support laser systems.

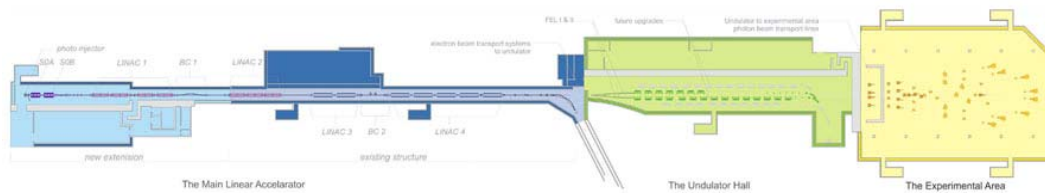


Figure 1. Overall FERMI layout.

3.4.3 Linear Accelerator and FEL's

3.4.3.1 *The Photo-Injector*

A high brightness electron beam is produced by a photo-injector is based on the proven 1.6 cell electron gun developed at BNL/SLAC/UCLA. The gun will produce a 10 ps long pulse with 0.8-1 nC charge and a rms normalized transverse emittance of 1.2 mm-mrad at 100 MeV. Following standard layout schemes, the design includes a solenoid for emittance compensation and acceleration to 100 MeV with two S-band rf sections. A laser pulse provides temporal and spatial bunch shaping. The FERMI design calls for a novel temporal bunch profile in which the bunch current increases approximately linearly with time (linear ramp). Such a profile at the start of acceleration produces a more uniform energy and current profile at the entrance to the undulators. Simulations using the GPT and Astra codes indicate that the electron beam performance objectives for injection into the main linac at 100 MeV are attainable. The timing and charge stability are challenging but within present state of the art.

3.4.3.2 *Main Linac and Beam Transport*

From the exit of the photo-injector the beam is accelerated to the final energy of 1.2 GeV. FEL-1 and FEL-2 will have different operating modes governed by user requirements. For FEL-1 an electron bunch length of 200 fs and a peak current of 800 A or higher will be used. For those experiments for which the timing jitter is critical, and to account for a predicted e-beam timing jitter of ~ 400 fs, the “medium bunch” design aims at a duration of 700 fs. Including the inevitable inefficiency of the compression system, the obtainable peak current is 800 A with 0.8 nC of charge from the photo-injector. FEL-2 covers the 40-10 nm wavelength range. This line provides up to ~ 400 fs long, high brightness FEL radiation pulses using the fresh part of the bunch technique. In this case, a ~ 1.4 ps “long bunch” of electrons is required from the electron accelerator. With a 1 nC bunch charge from the injector the attainable peak current is 500 A. For both operating modes, the energy and charge distributions correlated with the distance along the electron bunch should be as flat as possible in order not to broaden the FEL bandwidth. The horizontal and vertical normalized emittances at the end of the linac (1.2 GeV) should not exceed 1.5 mm-mrad to meet the desired photon throughput. This value, 30% higher than predicted by photo-injector simulations, includes a safety margin against emittance dilution effects.

At the exit of the photo-injector, the 100 MeV electrons enter the L1 linac where they are accelerated to 250 MeV (see figure 2). Acceleration off-crest creates the

correlated energy spread along the bunch needed to compress it in the first compressor, BC1. An X-band rf structure tuned at the 4th harmonic of the main (3 GHz) linac frequency is placed half-way between the four linac sections of L1. The function of the structure is to provide the non-linear quadratic and, when operated off-crest, cubic corrections of the correlated momentum distribution along the bunch in presence of the photo-injector and the magnetic compressors non-linearities and of longitudinal wake fields. The L2 and L3 linac structures, located between the first and second bunch compressors, accelerate the beam from 250 MeV to 650 MeV. They also provide the residual momentum chirp needed for the second compressor, BC2. After BC2 the beam is accelerated to its final 1.2 GeV energy in the L4 structure. The rf phases of the linac sections following BC1 are chosen to provide the necessary momentum spread for compression and also to cancel the linear part of the longitudinal wakes. The non-linear correlated momentum spread at the end of the linac is fine-tuned by acting on the amplitude and phase of the x-band structure. The linac focusing system is designed to minimize transverse emittance dilution due to transverse wakefields, momentum dispersion and coherent synchrotron radiation in bends.

Two transfer lines, one assigned to FEL-1 and the other to FEL-2, transport the electron beam from the linac end to the undulators. The two undulator lines are parallel and separated by 2 m. Fast switching between lines is not foreseen at this stage. The electron optics is designed to cancel any emittance blow up due to the emission of coherent synchrotron radiation in the bends by a suitable choice of the small bending angles and of the phase advances between dipoles. The lattice of the spreader is flexible, and allows to switch from the configuration for photon delivery to a configuration less suitable for operation but optimized for electron beam diagnostics purposes.

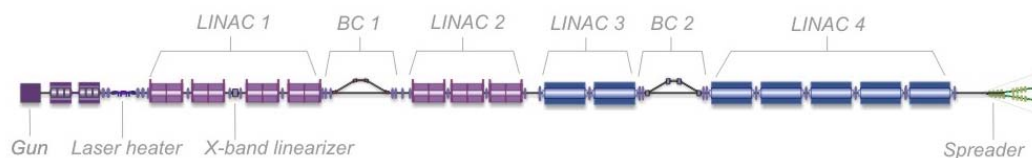


Figure 2: Schematic Layout of the Linac.

3.4.4 Photon Production

3.4.4.1 Principle of Operation

Photon production is based on the principle of the high gain, harmonic generation FEL amplifier employing multiple undulators, up-shifting an initial “seed” signal in a single-pass. The initial seed signal is provided by a conventional pulsed laser operating at wavelengths in the region 240-300 nm. The energy modulation induced by the interaction of the laser with the electron beam in the first undulator (the modulator) is converted to spatial modulation by passing the beam through the magnetic field of a dispersive section. The bunching further increases the initial bunch modulation at harmonics of the seed wavelength. Thus re-bunched, the electrons emit coherent

radiation in a second undulator (the radiator) tuned at a higher harmonic corresponding to the desired FEL output. FEL-1 requires one stage of “modulator + dispersive section +radiator” to reach 40 nm. FEL-2 will require a second stage to reach 10 nm and will adopt a “fresh part of the bunch” seeding technique for the FEL process.

The choice of harmonic generation by an external seed laser is dictated by the scientific applications and the flexibility that such choice entails. As the seed laser determines the duration, bandwidth, and wavelength of the output radiation, all are tunable and controllable, covering a wide spectral range. The seed laser provides a reference signal to facilitate the femtosecond level precision timing and synchronization of all systems.

3.4.4.2 Undulators and Beamlines

FEL-1 and FEL-2 are required to provide, at all wavelengths, continuously tunable beam polarization ranging from linear-horizontal to circular to linear-vertical. The FEL-1 radiator and the final radiator in FEL-2 will be APPLE-II type undulators. For the modulator a simple, linearly-polarized configuration has been chosen both for its simplicity and because the input radiation seed can be linearly polarized. The wavelength will be tuned by changing the undulator gap at constant electron beam energy. The FEL-1 and FEL-2 radiators consist of 6 and 10 undulator modules of roughly 2.4 m magnetic length. Electromagnetic quadrupoles, high quality beam position monitors and quadrupole movers are installed in between magnets to correct the electron trajectory. At the shortest design wavelength of 10 nm, the FEL process requires the straightness of the electron trajectory in the undulators to stay within 10 μm (rms value over the undulators length). This performance can be achieved by present state-of-the-art surveying techniques together with beam-based-alignment procedures.

Pulse length preservation, mono-chromatization, energy resolution, source shift compensation, focusing in the experimental chamber and beam splitting are all included in the design of the FEL radiation transport system. It is designed to handle the high power of up to 10 GW in a sub-ps long pulse. Its differentially pumped vacuum system is windowless, the low-Z material beam line components operate at grazing incidence angles and the radiation intensity is controlled by a gas absorption cell.

3.4.5 Design Studies

To meet requirements of operational flexibility the design is based on extensive studies of possible perturbations that may affect the electron beam dynamics, of means to correct them, and of parameter optimization. These studies show that the most important determinants of the quality of the FEL radiation are the quality and uniformity of the electron beam properties along the bunch (energy, energy spread, transverse emittance, electron optics, peak current, etc.), as well as the pulse-to-pulse stability of such properties. A cornerstone for these studies has been provided by “end-to-end” simulations, in which the electron beam is tracked from the photocathode, through the linac and all the way through the FEL process. The exhaustive studies carried out included foreseen random perturbations and jitters of accelerator and FEL parameters. A challenging aspect on the overall design was the demand to produce transform-limited optical pulses with narrow bandwidth requiring as uniform as possible peak current and energy distributions along the bunch at the undulator entrance. Extensive theoretical and computational studies[1] were carried out in order to understand the non-linear magnetic and collective effects that might impede the

achievement of such a uniform electron beam distribution. It was found necessary to correct the linear, quadratic and cubic terms of the energy variation along the bunch with judicious choices of the accelerating rf phases. Determination of the optimal choice of parameters, in particular the initial longitudinal beam distribution, was done by tracking an ideal beam backwards through the accelerator to the photo-injector section. Coherent synchrotron radiation (CSR) in the bends does not play an important role in the beam distribution for FERMI allowing meaningful back tracking results. This technique revealed that at the start of the main acceleration a current distribution that was ramped along the bunch provides an effective way to combat the non-linearities induced by longitudinal wake-fields in the accelerating structures. A varying charge density along the bunch, however, makes the solenoidal emittance compensation less than perfect [2]. In the FERMI case the effect is small, resulting in an emittance increase of less than 20% compared to that produced by a flat distribution. Emittance dilution in the linac due to transverse wake-fields [3] and anomalous momentum dispersion, each of which arises with component misalignments have been simulated. These simulations include realistic correction techniques and successfully demonstrate that the required level of transverse emittance preservation is achievable. Jitter studies [4] have focused mainly on the longitudinal dynamics, since the FEL process is more sensitive to the longitudinal jitter than to jitter in the transverse planes. A global jitter study verified the stability of the methods implemented to counteract the wake fields, such as beam shaping, cubic chirp manipulation and so on. A jitter study was also applied to each slice of the final beam to characterize the stability of each sub-ensemble of the beam.

Although the choice of parameters is sound, there are still accelerator physics issues that need to be studied further. Foremost among them is the microbunching instability, which in the present configuration is mitigated using a laser heater at 100 MeV. It is important for the FEL process that the beam slice energy spread not be much larger than 150 keV (rms value). Six-D, end-to-end tracking simulations are normally carried out with the codes GPT [5], Astra [6], and Elegant [7]. However, it was found that the numerical noise driven by the finite number of particles used in the tracking (200,000) for reasonably short computing times affects the final results when longitudinal space charges are included. For this reason, two codes have been developed at the Center for Beam Physics at LBNL that allow simulating hundreds of million of particles. They are IMPACT [8], based on parallel processors, and a "Vlasov solver"[9] that tracks the particle distribution. Preliminary results from both codes indicate that the energy spread may exceed the desired 150 keV. Studies on this very important issue are ongoing, including the possibility of using, for those cases that warrant it, the use of only the low energy bunch compressor (BC1). This option, it is hoped, will moderate the onset of the micro-bunching process, since the 2nd bunch compressor is the main source of the instability. So far ideal drive laser distributions have been used and future studies will use a realistic laser pulse shape, including the determination of tolerances for the departure from its ideal shape. Recent FEL studies have also show the desirability to extend the parameters in the direction of shorter bunches (50 fs) with a peak current of about 2 kA. This configuration requires even more challenging compensation of the non-linear distortions induced by the longitudinal wakes and the stronger compression and also requires close attention to the CSR driven microbunching instability. A continuation of the studies of timing and trajectory jitter is also high on the agenda. This research includes a study of the sensitivity of the FEL output to the accelerator

parameters and a realistic simulation of the several types of feedback that are planned to stabilize the beam.

3.4.6 Status

The conceptual design study has been completed and the technical design, engineering and construction of the facility are under way. The replacement injector for Elettra will be commissioned in the third quarter of 2007, fully freeing the linac for the necessary upgrades. Activities are progressing with accelerator, beamline and end-station systems. Civil engineering for the backward extension of the linac tunnel and associated klystron gallery is ongoing as is the engineering, procurement and construction management of FERMI main infrastructures. First light and first user experiments using FEL-1 are foreseen for 2009, while commissioning of main systems for FEL-2 will occur in 2010. The project has greatly benefited from close and continual collaboration between many institutes and user groups, in particular the Center for Beam Physics and the Engineering Division at LBNL, the LCLS Division at SLAC, the MIT Center for Accelerator Science and Technology and the EUROFEL group.

3.4.7 References

1. M. Cornacchia, S. Di Mitri, G. Penco, A. A. Zholents, "Formation of electron bunches for harmonic cascade x-ray free electron lasers", *Phys. Rev. ST Accel. Beams* 9, 120701 (2006) and S. Di Mitri, "How to Obtain High Quality Electron Bunches in Presence of Normal Conducting Linac Wakefields", *Proc. FEL Conf.*, 2006.
2. G. Penco, M. Trovo, S. Lidia (LBNL) "Ramping Longitudinal Distribution Studies for the [FERMI@ELETTRA](#) Photoinjector" *Proc. FEL Conf.*, 2006.
3. P. Craievich, S. Di Mitri, "Emittance Growth due to Short-Range Transverse Wakefields in Linacs", *Proc. FEL Conf.*, 2006.
4. P. Craievich, S. Di Mitri, A. Zholents, "Jitter Studies for the [FERMI@ELETTRA](#) Linac", *Proc. EPAC. Conf.*, 2006.
5. S.B. Van der Geer, et. al., <http://www.pulsar.nl/gpt/index.html>.
6. K. Flöttman, https://www.desy.de/~mpyflo/Astra_dokumentation.
7. M. Borland, "Elegant: A Flexible SDDS-Compliant Code for Accelerator Simulations, Advanced Photon Source LS-287, September 2000.
8. J. Qiang, R. Ryne, S. Habib, V. Decyk, "An Object-Oriented Parallel Particle-In-Cell Code for Beam Dynamics Simulation in Linear Accelerators," *J. Comp. Phys.* Col 163, 434, (2000)
9. M. Venturini, et. al. "Development of a 2D Vlasov Solver for Longitudinal Beam Dynamics in Single-Pass Systems, LBNL-60513, June 2006".

4 Single-Particle Beam Dynamics

4.1 Computation of Transfer Maps from Magnetic Field Data in Wigglers and Undulators

C. E. Mitchell and Alex J. Dragt
 University of Maryland at College Park, USA
 Mail to: cemitch@glue.umd.edu, dragt@physics.umd.edu

4.1.1 Introduction

Simulations indicate that the dynamic aperture of damping rings and storage rings is critically dependent on the nonlinear properties of their wiggler/undulator transfer maps. The computation of single-particle transfer maps through wigglers and undulators has often employed idealized wiggler models [1,2]. However, wiggler transfer maps can in general depend sensitively on fringe-field and high-multipole effects. The inclusion of these effects requires a detailed and realistic model of the interior and fringe magnetic fields, including knowledge of high spatial derivatives. We describe how such information can be extracted reliably from 3-dimensional magnetic field data $\mathbf{B}(\mathbf{r})$ on a grid as provided by various 3-dimensional finite element field codes, for example OPERA-3d available from Vector Fields.

The required high derivatives of the vector potential \mathbf{A} , required to compute transfer maps, cannot be reliably computed directly from this data by numerical differentiation due to numerical noise whose effect becomes progressively worse with the order of derivative desired. The effect of this noise, and its amplification by numerical differentiation, can be overcome by fitting on a bounding surface far from the axis. We consider, in particular, field data supplied in the domain between pole faces of wiggler magnets with small gap and wide poles (Fig 1). Fitting is done using a cylinder with *elliptical* cross-section. This approach preserves the desirable features of previous approaches that have employed a cylinder with circular cross-section [3] while it improves insensitivity to errors in the boundary data by exploiting the wide pole-face geometry. The key ingredients are the use of surface data and the smoothing property of the inverse Laplacian operator. We also discuss briefly the use of other geometries.

As an application, we produced a transfer map for the proposed ILC (CESR-c type) wiggler using data provided by finite element computations [4]. Values of \mathbf{B} were provided on a rectangular mesh along the full length of the wiggler including the fringe-field regions. The normal component of \mathbf{B} on the surface of the elliptical cylinder was obtained by interpolation using polynomial splines. This normal component on the surface was then used to compute the desired interior expansion for \mathbf{A} using the scalar potential as an intermediate quantity.

4.1.2 Transfer Maps

Charged-particle motion through any beam-line element is described by a symplectic transfer map \mathcal{M} . Through aberrations of order $(n-1)$ such a map has the Lie representation [5,6]

$$\mathcal{M} = \mathcal{R}_2 \exp(: f_3 :) \exp(: f_4 :) \cdots \exp(: f_n :) \quad (1)$$

where \mathcal{R}_2 describes the linear part of the map.

The linear map \mathcal{R}_2 and the Lie generators f_m are determined by solving the equation of motion $\mathcal{M}^X = \mathcal{M} : -H :$. The deviation variable Hamiltonian H is determined in turn by the Hamiltonian K with z as the independent variable. In Cartesian coordinates, and in the absence of electric fields, K is given by

$$K = -(p_t^2/c^2 - m^2c^2 - (p_x - qA_x)^2 - (p_y - qA_y)^2)^{\frac{1}{2}} - qA_z \quad (2)$$

and has the (truncated) expansion

$$H = H^2 + H^3 + \cdots + H^n = \sum_{s=1}^S h_s(z) P_s(6; x, p_x, y, p_y, \tau, p_\tau). \quad (3)$$

Here the $P_s(6; \cdots)$ are the various homogeneous monomials in the six phase-space deviation variables, and the H^m denote the sum of all such terms that are homogeneous of degree m . Expanding about a design orbit through the wiggler at a longitudinal location z yields representations for the components of \mathbf{A} of the (truncated) form

$$A_w(x, y, z) = \sum_{l=1}^L a_l^w(z) P_l(2; x, y). \quad (4)$$

Here $w = x, y$, or z and the $P_l(2; x, y)$ are the various homogeneous monomials in the two transverse deviation variables (x, y) . The upper limits L and S in the sums (3) and (4) are determined by n . For example, if $n = 6$ then $L = 27$ and $S = 923$.

We conclude that the computation of high-order maps requires a Taylor expansion for the vector potential components A_w in the deviation variables x and y . Their z -dependent coefficients $a_l^w(z)$ must be accurately determined from a knowledge of \mathbf{B} . In the following section, we construct a representation for the vector potential that is analytic (so that high derivatives can be computed), satisfies Maxwell's equations exactly, $\nabla \times \nabla \times \mathbf{A} = 0$, and accurately represents both the magnetic field and its high-order derivatives.

4.1.3 Fitting the Wiggler Field

Consider elliptic cylinder coordinates defined by

$$\begin{aligned} x &= f \cosh(u) \cos(v) \\ y &= f \sinh(u) \sin(v) \end{aligned} \quad (5)$$

where the radial coordinate u satisfies $u \geq 0$, and the angular coordinate v satisfies $-\pi \leq v \leq \pi$. Here f is the distance of the focus of the ellipse to the axis. The general solution of Laplace's equation in elliptic cylindrical coordinates takes the form

$$\psi = \sum_{m=0}^{\infty} \int_{-\infty}^{\infty} dk e^{ikz} [\alpha(k) Ce_m(u, q) ce_m(v, q) + \beta(k) Se_m(u, q) se_m(v, q)] \quad (6)$$

where we set $q = -k^2 f^2 / 4$. Here $ce_m(v, q)$ and $se_m(v, q)$ are Mathieu functions, while $Ce_m(u, q)$ and $Se_m(u, q)$ are modified Mathieu functions [7,8]. Consider an infinite cylinder of elliptical cross-section with axis along the z-axis defined by the equation $u = U$, where U is a constant. The cylinder is characterized by the pair of parameters (U, f) . The normal component of \mathbf{B} on the surface of the cylinder may be written in terms of the scalar potential ψ in elliptic cylindrical coordinates as:

$$\tilde{B}_u(u = U, v, k) = [\partial_u \tilde{\psi}(U, v, k)] / \sqrt{J(U, v)} \quad (7)$$

where

$$\partial_u \tilde{\psi}(U, v, k) = \sum_{m=1}^{\infty} [F_m(U, k) se_m(v, q) + G_m(U, k) ce_m(v, q)] \quad (8)$$

is the derivative of the scalar potential with respect to the coordinate u . Here $J(u, v)$ is the Jacobian of the mapping from Cartesian to elliptic coordinates. The normal component of \mathbf{B} on the surface of the elliptical cylinder may be obtained by interpolation of field values using polynomial splines. The surface values of the field are then characterized by the surface functions F_m and G_m . All desired quantities may now be written in terms of on-axis gradients $C_{r,s}(z)$, $C_{r,c}(z)$, given by

$$C_{r,\alpha}^{(m)}(z) = \frac{i^m}{2^r r! \sqrt{2\pi}} \int_{-\infty}^{\infty} k^{r+m} e^{ikz} \beta_r^\alpha(U, k) dk \quad (9)$$

where

$$\begin{aligned} \beta_r^s(U, k) &= \sum_{m=0}^{\infty} g_s^m(k) B_r^{(m)}(k) \left[\frac{F_m(U, k)}{Se'_m(U, q)} \right], \\ \beta_r^c(U, k) &= \sum_{m=0}^{\infty} g_c^m(k) A_r^{(m)}(k) \left[\frac{G_m(U, k)}{Ce'_m(U, q)} \right]. \end{aligned} \quad (10)$$

Here Se'_m and Ce'_m are derivatives of the modified Mathieu functions, and the functions g_α^m , $B_r^{(m)}$, $A_r^{(m)}$ are independent of the geometry or surface data. The on-axis gradients uniquely characterize the interior field and its derivatives [9]. In the case of midplane symmetry, the vertical field through terms of degree four is given in terms of the on-axis gradients (9) by the relation

$$B_y = C_1(z) + 3C_3(z)(x^2 - y^2) - C_1^{[2]}(x^2 + 3y^2)/8 + C_1^{[4]}(z)(x^4 + 6x^2y^2 + 5y^4)/192 - C_3^{[2]}(z)(3x^4 + 6x^2y^2 - 5y^4)/16 + C_5(z)(5x^4 - 30x^2y^2 + 5y^4). \quad (11)$$

There are similar expressions for the other components of \mathbf{B} and the components of \mathbf{A} . We emphasize that on-axis gradients are obtained using only information about the field on the elliptic cylindrical boundary. The advantages of this technique are as follows.

1. Maxwell's equations are satisfied by construction.
2. The numerical error in the interior is globally controlled. Due to the properties of harmonic functions, the error must take its extrema on the boundary, where we have done a controlled polynomial fit to the field data.
3. Such techniques have been benchmarked against analytic results for fields due to arrays of magnetic monopoles. These results will be discussed in the following section.
4. Results are relatively insensitive to surface errors due to the smoothing property of the inverse Laplacian operator. That is, each kernel multiplying the surface functions F_m and G_m falls off rapidly with frequency k . As a result, high frequency noise in the boundary data has little effect on the functions $C_{r,\alpha}^{[m]}$, as we will discuss in the section on Smoothing.

4.1.4 Benchmarks

A partial test of the accuracy of this procedure (and on the quality of the magnetic data on the mesh) is that the magnetic field computed from the surface data should reproduce the magnetic field at the interior mesh points. We computed such an interior fit, and the associated transfer map, for the modified CESR-c design of the Cornell wiggler, which has been accepted as the design prototype for use in International Linear Collider studies. We were provided data obtained from the 3-dimensional finite element modeling code OPERA-3d on a mesh $0.4 \times 0.2 \times 0.2$ cm in a volume $10.4 \times 5.2 \times 480$ cm, extending beyond the fringe-field region. The fit obtained for the vertical field of the proposed ILC wiggler is shown in Fig 2. Both the z and x dependence of the field are well described. The fit employed an elliptical cylinder with semimajor axis 4.4 cm and semiminor axis 2.4 cm. Other components of the field are fit equally well. We find residuals in the midplane of 0.5 G relative to a peak field of 16.7 kG.

A more demanding test of our procedure has been made by verifying that values for fields and their high derivatives as computed numerically from surface data agree with analytically computed values in the case of a soluble test field. In particular, we consider the field produced by a pair of magnetic monopoles of strength $g=0.3 \text{ Tcm}^2$ lying at locations $z = \pm 4.7008$ cm. Exact field values were computed on the surface of an elliptical cylinder, on-axis gradients were obtained using (9) and (10), and these gradients were compared with analytic results. We found, for example, that the gradients $C_{1,s}$, $C_{3,s}$, $C_{5,s}$, and their z -derivatives exhibited errors relative to peak of less than 3×10^{-9} .

4.1.5 Smoothing

When computing symplectic maps we are particularly interested in high-order derivatives of the field data. One straightforward method of computing these derivatives involves fitting an interpolating function to data near or on the axis of the magnetic element and approximating derivatives using derivatives of this interpolant. However, the presence of small, random numerical errors at each mesh point introduces noise in the high-frequency tail of the spectrum for the interpolating function. This high-frequency noise is amplified by each differentiation. Numerical studies of wiggler finite-element data indicate that such techniques rapidly fail for high-order derivatives.

The use of surface fitting eliminates such noise due to the high-frequency behavior of the kernels multiplying F_m and G_m in (10), a property known as smoothing. The amount of smoothing increases with domain size. Suppose we fix the semiminor axis b and increase the semimajor axis a , stretching the elliptic cylinder horizontally and enlarging the enclosed cross-sectional area to include the "wings" of the domain. In Fig (3) we have illustrated the computation of the gradient $C_5(z)$ for the ILC wiggler, for three different domains. The first was computed using a small elliptic cylinder $(a,b) = (1,0.6)$ cm. The second figure was obtained by extending the semimajor axis to fill the domain horizontally, with $(a,b) = (4.4,0.6)$ cm. At this point the noise has been suppressed. The third was obtained by extending the semiminor axis to fill the domain permitted by the data, with $(a,b) = (4.4,2.4)$ cm. Note that little change appears between the second and third figures, indicating that increasing the horizontal domain size alone is sufficient in this case to eliminate high-frequency noise. Figure 3 illustrates that, even for a small vertical aperture, use of a large aspect-ratio ellipse can dramatically improve accuracy.

4.1.6 Generalization to Other Domains

The previous technique can be used effectively for straight-axis magnetic elements. For elements with significant sagitta, such as dipoles with large bending angles, we must generalize to more complicated domains for which Laplace's equation is no longer separable. Surface data can again be used to fit interior data provided *both* ψ and the normal component of \mathbf{B} are available on the surface. In this case, surface data are integrated against a geometry-independent kernel [10]. This technique also has all the advantages previously described for cylindrical fitting. We have implemented such a routine for fitting data onto the surface of a bent box (Fig 4). The routine has again been benchmarked using arrays of magnetic monopoles. We verify that $\nabla \cdot \mathbf{B} = 0$ and $\nabla \times \mathbf{B} = 0$ to machine precision, while Taylor coefficients produced were accurate to 10^{-6} .

In summary, surface methods provide a reliable and numerically robust procedure for extracting transfer maps from numerical field data. The smoothing property of the inverse Laplacian operator ensures that computed derivatives are relatively insensitive to errors in the surface data. Such methods provide a promising approach to the general problem of computing realistic transfer maps for real magnets with complicated fringe and high-order multipole error fields.

4.1.7 References

1. Y. Cai, "Dynamic Aperture in Damping Rings with Realistic Wigglers", ser. Workshop on Wiggler Optimization for Emittance Control, INFN-LNF, February (2005).
2. J. Gao, "Analytical Estimation of Dynamic Apertures Limited by Wigglers in Storage Rings", PAC03 (2003)
3. M. Venturini and A. Dragt, "Accurate Computation of Transfer Maps from Magnetic Field Data", Nuclear Instruments and Methods, A427, p. 387 (1999).
4. J. Urban and G. Dugan, "CESR-c Wiggler Studies in the Context of the International Linear Collider Damping Rings", PAC 2005 (2005)
5. A. Dragt and F. Neri, "Lie Algebraic Treatment of Linear and Nonlinear Beam Dynamics", Annual Review of Nuclear and Particle Science, 38, p 455 (1988)
6. Dragt, "Lie Methods for Nonlinear Dynamics with Applications to Accelerator Physics", some 1020 pages available in draft form (2007)
7. M. Abramowitz and I. Stegun, Handbook of Mathematical Functions, Dover Publications (1972)
8. N. McLachlan, Theory and Application of Mathieu Functions, Dover Publications (1964)
9. A. Dragt, T. Stasevich, and P. Walstrom, "Computation of Charged-Particle Transfer Maps for General Fields and Geometries Using Electromagnetic Boundary-Value Data", Proceedings of the 2001 Particle Accelerator Conference (2001)

4.1.8 Figures

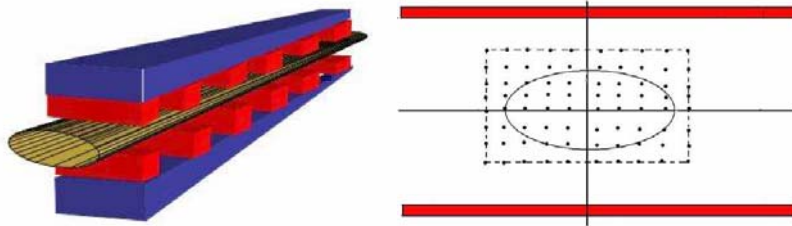


Figure 1: (Left) An elliptical cylinder fitting between the pole faces, having large major axis, and extending beyond the fringe-field region. (Right) End view of 3-d mesh on which B is given.

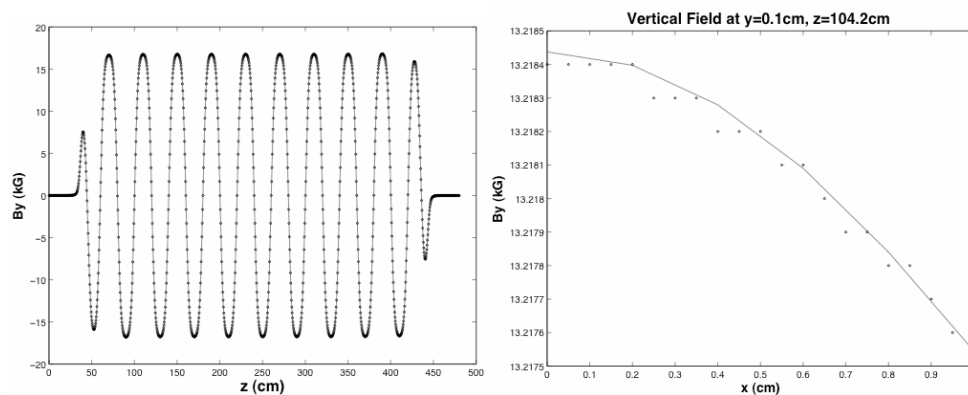


Figure 2: Fit obtained to proposed ILC wiggler vertical field using an ellipse with $x_{\max}=4.4\text{cm}$, $y_{\max}=2.4\text{cm}$. The solid line is computed from surface data; dots are numerical data provided by OPERA-3d.

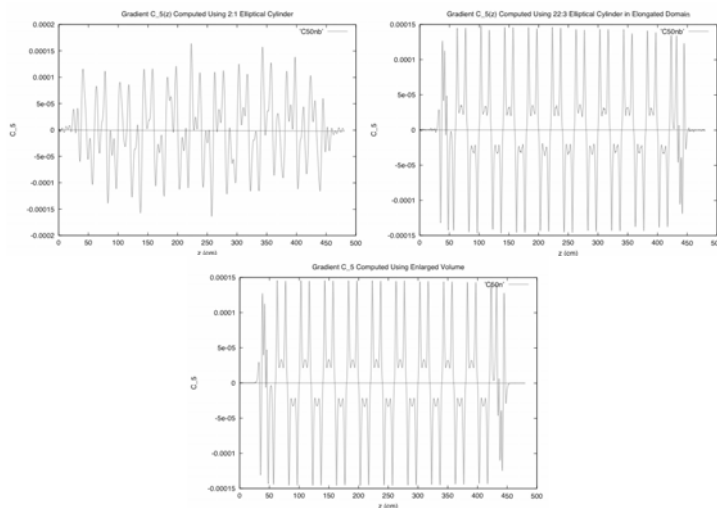


Figure 3: Illustration of the effect of domain size on the smoothing of numerical errors. (Left) Gradient $C_5(z)$ computed using a small elliptical cylinder $(a,b) = (1,0.6)$ cm. (Center) Gradient computed with $(a,b) = (4.4,0.6)$ cm. (Right) Gradient computed with $(a,b) = (4.4,2.4)$ cm.

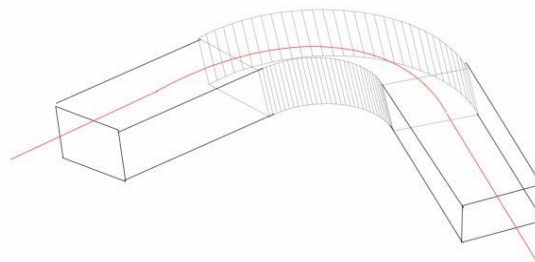


Figure 4: Bent box surrounding the design orbit for a dipole bending magnet with large sagitta. The straight legs of the box extend beyond the fringe-field region.

4.2 Storage Ring Optics Measurement, Model, and Correction

Yiton T. Yan

Mail to: yan@slac.stanford.edu

SLAC, 2575 Sand Hill Road, Menlo Park, CA 94025, USA

4.2.1 Introduction

To improve the optics of a storage ring, it is very helpful if one has an accurate lattice model. Although the ideal lattice may serve such a purpose to some extent, in most cases, real accelerator optics improvement requires accurate measurement of optics parameters. In this section, we present precision measurements of a complete set of linear orbits from which we can form a linear optics model to match the linear optics of the real machine. We call such a model a virtual machine [1].

To obtain a virtual machine, one starts with a computer lattice model with its initial state of the ideal lattice design or the previously obtained virtual machine. A complete set of independent machine quantities must be considered as variables to fit a sufficient set of well chosen linear-optics parameters that are obtainable from calculation of the computer lattice model and measurement of the real machine. It can be better interpreted with a simple mathematical formula

$$\vec{Y}(\vec{X}) = \vec{Y}_m \quad (1)$$

where the array \vec{X} represents a complete set of variables while array \vec{Y} is a well selected sufficient set of optics parameters that are to be fitted to their respective corresponding quantities, the array \vec{Y}_m , from real machine measurements.

\vec{Y} is the response to \vec{X} and is therefore a vector function of \vec{X} as is explicitly shown in Equation (1). The task is to find \vec{X} such that \vec{Y} matches \vec{Y}_m . For linear geometric optics, a reasonably complete set of independent variables would be all quadrupole strengths and sextupole feed-downs. Since we cannot avoid BPM gains and BPM cross couplings, they should also be included as variables. The response quantities we have chosen are the phase advances and the Green's functions among BPMs. The Green's functions are simply the transfer matrix components R_{12} , R_{34} , R_{32} , R_{14} between any two BPMs. There are essentially an unlimited number of such Green's functions that help in fitting convergence and accuracy. We can also choose Eigen coupling ellipses' tilt angles and axis ratios at all double-view BPM locations as response quantities. However, we usually leave these coupling quantities alone for an after-fitting check to see if they automatically match between the virtual machine and the real machine to make sure the virtual machine is indeed the right one.

The above variables and response quantities form a complete fitting system for geometric optics only. Therefore, if we include the linear dispersions at BPMs as response quantities, we should add suitable bending magnet strengths and/or orbit corrector strengths as fitting variables. However, for application to PEP-II optics, we found that once the geometric optics was fitted, the dispersion was roughly matched between the virtual model and the measurement for most cases. This encouraged us to consider adding dispersion fitting without adding bending or corrector magnet strengths as variables. However, we may turn on normal quadrupole skew components as additional variables to achieve dispersion fitting with negligible effect on the geometric optics.

Once the virtual machine is obtained, one may use it to find and adjust one or two magnets with noticeable differences from our expectation. However, a more fruitful practice would be to use the virtual machine to search for an easily-approachable better-optics model by pre-selecting and fitting a group of normal and skew quadrupole strengths or orbit correctors (for creating sextupole bumps), and then create a machine operation knob for dialing into the real accelerator. These procedures have been successfully applied to PEP-II for optics improvement and have made a major contribution to PEP-II luminosity enhancement.

4.2.2 Geometric and Chromatic Orbit Measurement with a Model-Independent Analysis (MIA)

4.2.2.1 Geometric Orbit Measurement

Linear geometric optics is determined if one has 4 independent linear (betatron) orbits. This can be shown by first forming the 4 independent linear orbits at each location into a 4-by-4 matrix \mathbf{Z} , such that each orbit is in a column. Then a linear map, a 4-by-4 matrix \mathbf{R}^{ab} , can map the orbit matrix from any point a to any other point b such that $\mathbf{Z}^b = \mathbf{R}^{ab}\mathbf{Z}^a$. Since \mathbf{Z}^a has an inverse for 4 independent linear orbits, the linear map between any two points \mathbf{R}^{ab} is determined. Therefore, a complete geometric set of data must provide the extraction of 4 independent orbits.

With a model-independent analysis (MIA) [2], ideally, one may take advantage of beam particle jittering for extracting 4 independent linear orbits with Model-Independent Analysis MIA [2] from multi-sets of turn-by-turn BPM buffer data without invading the machine. However, unfortunately and fortunately (to be clear later), this is not the case for a damping storage ring such as the PEP-II e- (HER) or e+ (LER) storage ring due to radiation damping. Therefore, for a damping storage ring one must unfortunately invade the machine to excite the betatron orbits. In order to extract 4 independent linear orbits, the most economic process would be through two orthogonal resonance excitations, one at the horizontal (Eigen-plane 1) and the other at the vertical (Eigen-plane 2) betatron tune, and then take and store buffered BPM data. Since each betatron motion has two degrees of freedom (phase and amplitude), each excitation generates a pair of conjugate (cosine- and sine-like) betatron motion orbits. They are obtained from the real and imaginary parts of the tune-matched (zooming) FFT respectively. Fortunately, it should be noted that exciting betatron orbits for a damping machine makes the wanted signal (the betatron motion) stand out. Figure 1 shows an example of 4 independent linear orbits from two resonance excitations for the PEP-II Low-Energy Ring (LER). Orbits x_1, x_2, y_3, y_4 show the major projection of the betatron motions while orbits y_1, y_2, x_3, x_4 show strong linear couplings in the interaction region (IR). Each pair of the conjugate orbits (x_1, x_2) and (y_3, y_4) contains the phase advancement which will be discussed later.

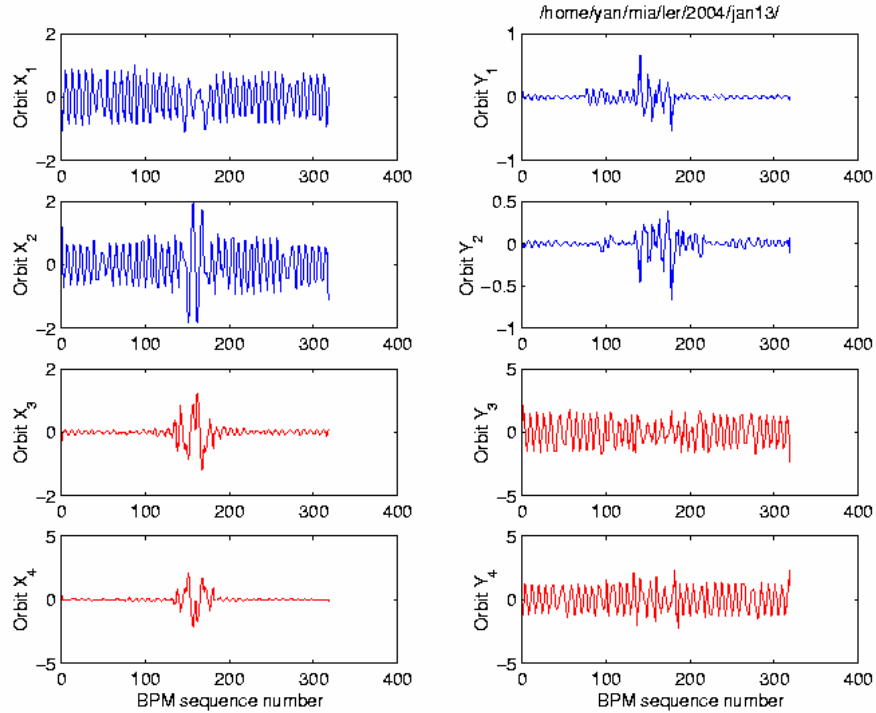


Figure 1: Four independent linear orbits extracted from PEP-II LER BPM buffer data taken on January 13, 2004. The first two orbits (x_1, y_1) and (x_2, y_2) are extracted from beam orbit resonance excitation at the horizontal tune while the other two orbits (x_3, y_3) and (x_4, y_4) are from resonance excitation at the vertical tune.

4.2.2.2 Chromatic Orbit Measurement

In order to extract dispersion, one may change the beam particle energy to find the transverse orbit difference. One may also try to use singular value decomposition (SVD) on the resonantly excited betatron orbits, where one may find the third largest singular mode to be the dispersion mode and the first and the second singular modes to be the two-degrees-of-freedom betatron motion modes, given that all bad BPM data have been excluded. However, to be consistent with the above accurate geometric orbit measurement, longitudinal oscillation at the synchrotron tune is resonantly excited for an additional transverse BPM data acquisition. Chromatic (dispersed) orbits at BPM locations are then measured by taking a longitudinal-tune-matched (zooming) FFT from such turn-by-turn BPM data.

4.2.2.3 Response Quantities

Once the variables (\vec{X} in Eq.1) in the computer lattice model are given, one can update the computer lattice transfer matrices. The response quantities (\vec{Y} in Eq.1: the phase advances and the Green's functions among BPMs, Eigen coupling ellipses' tilt angles and axis ratios, and the dispersions at BPM locations), are then calculated by

projection of these updated transfer matrices or the concatenated one-turn linear maps. Their corresponding quantities (\vec{Y}_m in Eq.1) from measurement are described below:

4.2.2.4 Phase Advances

The orbit betatron phase at each BPM location can be obtained by taking the arctangent of the ratio of the imaginary part to the real part of the resonance excitation FFT mode [1]. Phase advances between adjacent BPMs can then be calculated by subtractions. Note that the ratio of the imaginary part to the real part of the FFT will cancel the linear BPM gains but not the BPM cross couplings because beam orbit couplings and BPM cross couplings are not distinguishable from measurement. Therefore the phase advances among BPMs are repeatedly calculated during the Least Square fitting process as the BPM cross couplings and BPM gains are updated to correct the linear orbits.

4.2.2.5 Linear Green's Functions

The linear Green's functions [3] are simply R_{12}^{ab} , R_{14}^{ab} , R_{32}^{ab} , R_{34}^{ab} of the linear transfer matrix between any two BPMs labelled as a and b . They can be derived from the 4 independent orbits as given below.

$$\begin{aligned} (x_1^a x_2^b - x_2^a x_1^b) / Q_{12} + (x_3^a x_4^b - x_4^a x_3^b) / Q_{34} &= R_{12}^{ab} \\ (x_1^a y_2^b - x_2^a y_1^b) / Q_{12} + (x_3^a y_4^b - x_4^a y_3^b) / Q_{34} &= R_{32}^{ab} \\ (y_1^a x_2^b - y_2^a x_1^b) / Q_{12} + (y_3^a x_4^b - y_4^a x_3^b) / Q_{34} &= R_{14}^{ab} \\ (y_1^a y_2^b - y_2^a y_1^b) / Q_{12} + (y_3^a y_4^b - y_4^a y_3^b) / Q_{34} &= R_{34}^{ab} \end{aligned}$$

where Q_{12} and Q_{34} are the two betatron motion invariants of the two transverse resonance excitation at equilibrium state. If there is no BPM error, the two invariants and the Green's functions can be accurately derived from the 4 independent linear orbits. However, before Eq.1 is fitted and thus the BPM gains and cross couplings are not determined, we can only determine the ratio of the two invariants [4] and therefore leave either Q_{12} or Q_{34} as a fitting variable that belongs to \vec{X} in Eq.1. On the other hand, if we have all double-view BPMs, we could update the 4 independent orbits and therefore update the Green's functions each time we update the invariants, the BPM gains, and BPM Cross couplings during the fitting process. However, in most cases, one may not have all double-view BPMs. Therefore, we consider fitting these Green's functions in the BPM measurement space. That is, we transform corresponding Green's functions calculated from the computer lattice model into the BPM measurement space for Green's function fitting. The transformation is given below.

$$\begin{aligned}
R_{12} &= g_x^b R_{12} g_x^a + g_x^b R_{14} \theta_{xy}^a + \theta_{xy}^b R_{32} g_x^a + \theta_{xy}^b R_{34} \theta_{xy}^a \\
R_{32} &= g_y^b R_{32} g_x^a + g_y^b R_{34} \theta_{xy}^a + \theta_{yx}^b R_{12} g_x^a + \theta_{yx}^b R_{14} \theta_{xy}^a \\
R_{14} &= g_x^b R_{14} g_y^a + g_x^b R_{12} \theta_{yx}^a + \theta_{xy}^b R_{34} g_y^a + \theta_{xy}^b R_{32} \theta_{yx}^a \\
R_{34} &= g_y^b R_{34} g_y^a + g_y^b R_{32} \theta_{yx}^a + \theta_{yx}^b R_{14} g_y^a + \theta_{yx}^b R_{12} \theta_{yx}^a
\end{aligned}$$

where the BPM gains, $g_x^a, g_x^b, g_y^a, g_y^b$, and the BPM cross coupling multipliers, $\theta_{xy}^a, \theta_{xy}^b, \theta_{yx}^a, \theta_{yx}^b$, are repeatedly updated and applied for making the transformation during the fitting process.

4.2.2.6 Coupling Ellipses

For each double-view BPM, one can trace the MIA extracted high-resolution real-space orbits to obtain a coupling ellipse in real space for each resonance (Eigen) excitation. Shown in Figure 2 are typical Eigen ellipses projected in the real X-Y plane.

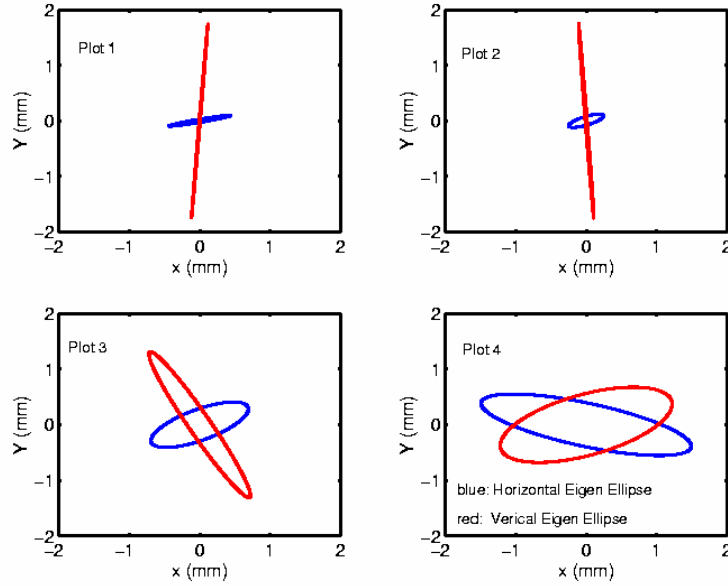


Figure 2: Eigen-mode coupling ellipses projected on the transverse x-y plane at 4 double-view BPM locations of PEP-II LER. The top 2 are at the two BPMs beside the IP, which show little coupling, while the bottom 2 are at the tenth BPMs from IP in each side, which show large couplings as the axis ratios of the short axis vs the long axis are large. (data acquired on September 30, 2003).

Therefore, one can calculate coupling ellipse tilt angles and axis ratios for all double-view BPMs [5]. The tilt angle of the coupling ellipse at the IP for the horizontal Eigen resonance excitation is very close to the real tilt angle of the beam at the IP. One can also calculate these corresponding coupling parameters from the linear map of a lattice model [5]. Therefore, these quantities can be used as part of the fitting parameters to help obtain an accurate virtual machine. For fitting speed consideration,

we prefer using more Green's functions to using coupling ellipses' tilt angles and axis ratios. However, these coupling ellipses' tilt angles and axis ratios are still very useful for after-fitting checks of self consistency that would verify the fitting accuracy.

4.2.2.7 Dispersions

Once we obtain the chromatic orbits from the longitudinal oscillation excitation, we can treat the chromatic orbits as being proportional to the linear dispersions. Both horizontal and vertical dispersions have the same proportional constant δ that is to be determined. That is, δ is a variable which belongs to \vec{X} in Eq.1.

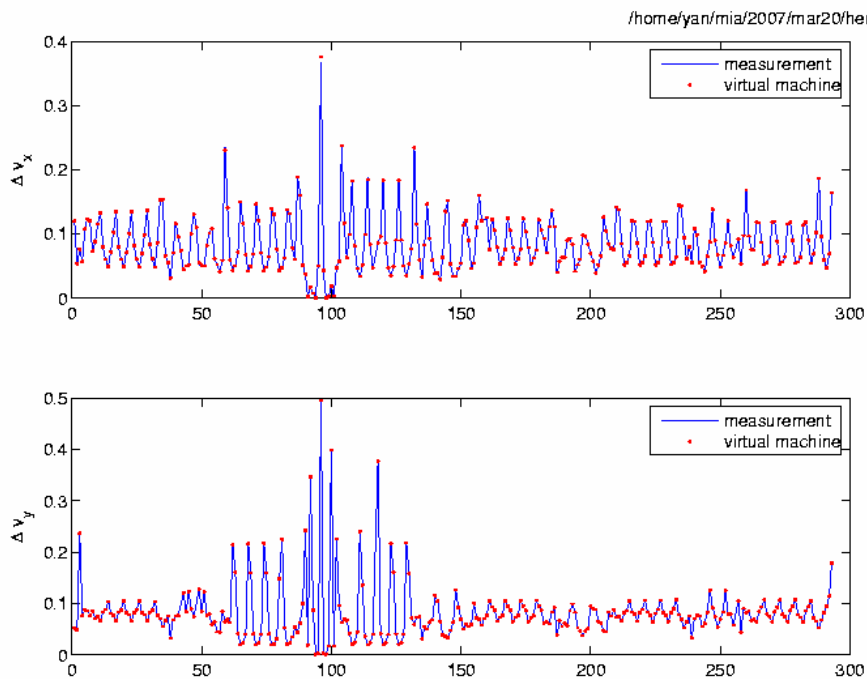


Figure 3: Typical plots comparing phase advances from measurement (blue) and from the virtual machine (red) of PEP-II HER on March 20, 2007.

4.2.3 SVD-Enhanced Least-Squares Fitting

Each time the variables \vec{X} (all quadrupole strengths, all sextupole feed-downs, all BPM gains and BPM cross couplings, one invariant, and one dispersion proportional constant) in Eq.1 are updated from the computer lattice model, one can calculate and update the phase advances, the Green's functions and the dispersions so as to fit them to their respective corresponding quantities derived from the 4 independent orbits that are obtained through high-resolution MIA analysis of the turn-by-turn BPM buffer data. With reasonable guessed initial values for the variables (for example, initialization with the ideal lattice design or with the previous virtual machine), Eq.1 can be efficiently carried out with an SVD-enhanced least-square fitting [6] that guarantees convergence provided that all bad BPM data are excluded. Figure 3 shows a comparison of phase advances between measurement and the corresponding virtual machine for PEP-II HER.

Since the phase advances are the fitted response quantities, that they match very well is a necessary but not necessarily sufficient condition to guarantee an accurate virtual machine. Fortunately, as stated in subsection 4.2.2.6, for fitting speed consideration, we do not fit for the coupling ellipses' parameters; we reserve them for after-fit check. Their automatic matching without fitting can establish a much stronger condition to make sure the fitting is all right. Figure 4 shows a comparison of coupling ellipses' parameters between measurement (blue) and the corresponding SVD-enhanced Least-Square fitted PEP-II LER virtual machine (red). The strong match shows that the fitting is pretty accurate and the virtual machine is reliable.

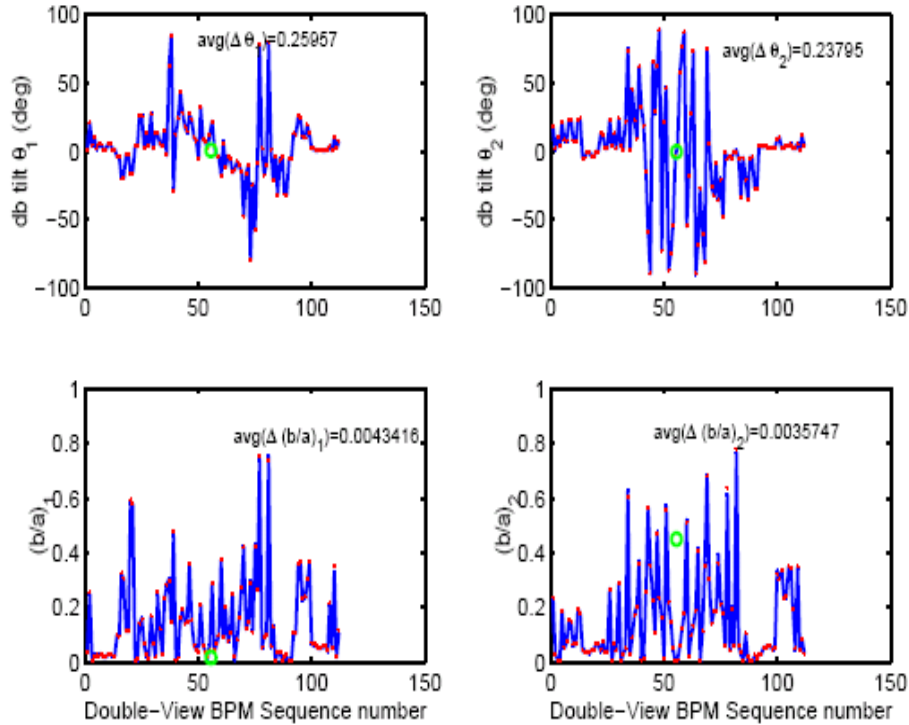


Figure 4: Typical plots comparing coupling characteristics for the whole ring. The Eigen-mode coupling ellipses' tilt angles (top plots) and axis ratios (bottom plots) are compared between measurement (blue) and its corresponding virtual machine (red) at all double-view BPM locations. Note that the left plots are for Eigen mode 1 (horizontal resonance excitation) while the right plots are for Eigen mode 2 (vertical resonance excitation).

4.2.4 Application for PEP-II Measurements

The PEP-II Low-Energy Ring (LER) has 319 BPMs while the High-Energy Ring (HER) has 293 BPMs. For each measurement of the LER (or HER), we take 3 sets of the MIA data for horizontal (Eigen mode 1), vertical (Eigen mode 2), and longitudinal resonance excitation of the beam motion. Once the complete sets of MIA data are collected, we retrieve the 4 independent geometric orbits and the chromatic orbits as discussed in Section 4.2.2. At the same time, we rank BPM data validity and identify those that must be excluded from the fitting for the virtual machine. This is a key step

for successful fitting – fitting unreliable data just does not work! To identify bad BPMs, we start by taking a singular value decomposition of each set of data and then identify those BPMs whose data show low correlation with most of the BPM data. At this stage, we would exclude those identified bad BPMs from the 4 independent orbits and start SVD-enhanced Least-Square fitting. In many cases, we get an accurate virtual machine without trouble. However, in some cases, we find that the residuals are not small enough after fitting is completed. In such cases, we would first find a small group of BPMs which are suspiciously bad but not identified, then take one such BPM out at a time and calculate (not fitting) its influence on the reduction of the residuals. If necessary, we would use more Green's functions in such fast tests of residual reduction. We would take out those (could be just one) BPMs that have a large effect on the residuals and continue the fitting process. Not only would we fit the residuals to a satisfactory small value such that fitted response quantities match very well, but we would also check and compare the measurement and the virtual machine for those response quantities that are not used for fitting to see if they match automatically as discussed in Section 4.2.3. Figure 5 shows a typical measurement of PEP-II HER on March 20, 2007. This figure shows a quick survey of the virtual machine optics that matches the real machine optics. It should be noted that in many cases we also try to understand the real machine optics by direct measurement without obtaining the virtual machine. However, these direct measurements rely on the perfection of BPMs and therefore are less accurate than those derived from the virtual machine because the virtual machine also takes into account the BPM gains and cross couplings.

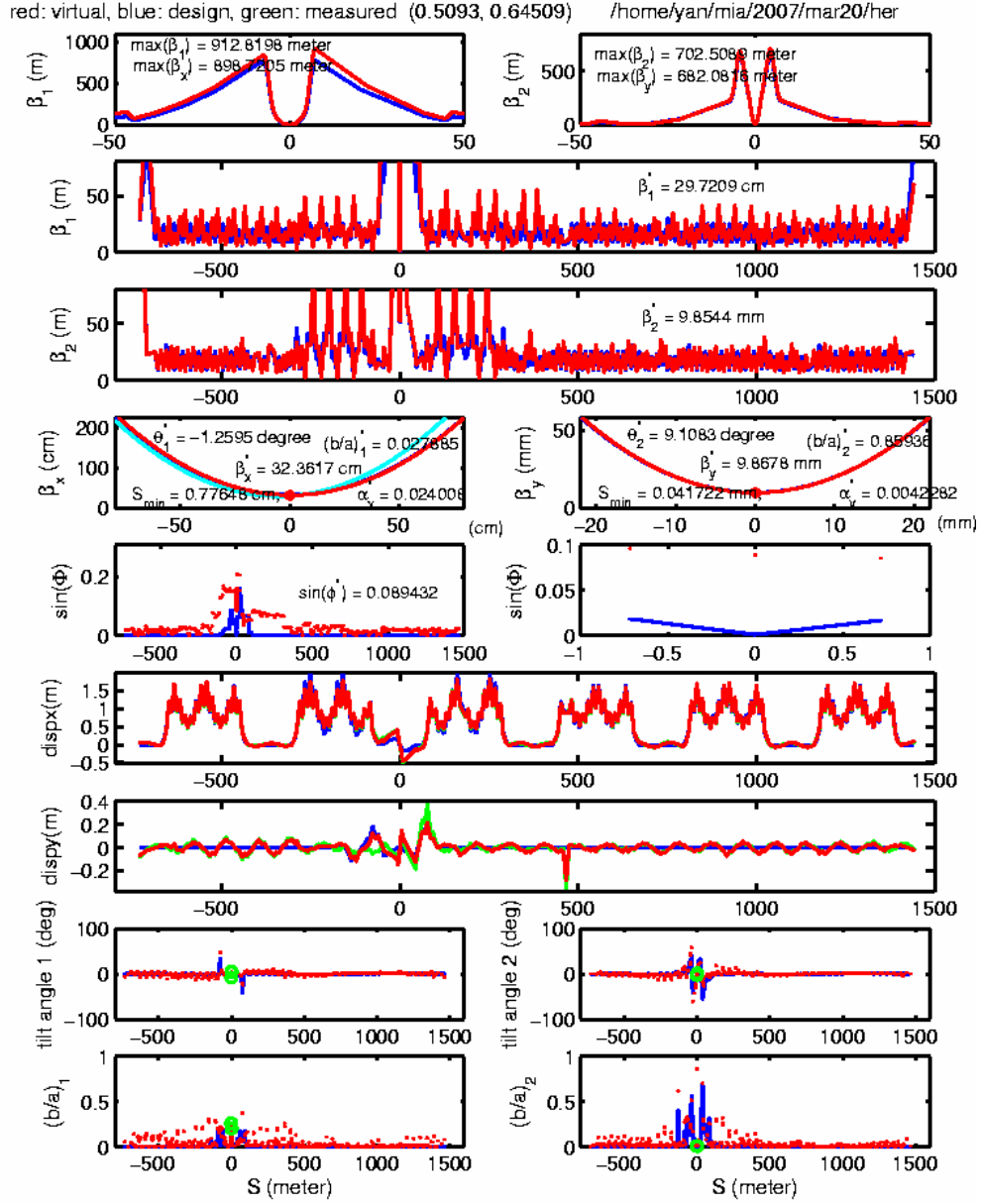


Figure 5: Typical plots to show virtual machine linear optics characteristics (red color) compared with those of the designed lattice (blue color). In this case, it is PEP-II HER measured on March 20, 2007. The top two plots show the two Eigen β functions in the vicinity of the IP followed by two plots that show the β functions for the whole machine and then the β function plots at the IP, which are accompanied by prints of the β^* , α^* , Eigen ellipses' tilt angles θ^* and axis ratios $(b/a)^*$ as well the waist shifts. The next two plots show the phase-space coupling determinants $\sin(\phi)$ followed by 2 plots that show the horizontal and vertical dispersions. The coupling ellipse parameters, the tilt angles, and the axis ratios for all double-view BPMs are compared in the last (bottom) 4 plots.

4.2.5 Application to PEP-II Optics Improvement - Examples

Once the optics-matched virtual machine is obtained through an SVD-enhanced Least-Square fitting, the updated transfer matrices can be concatenated into one-turn maps at the desired locations for calculating optics parameters. By fitting a well selected set of normal and skew quadrupoles as well as orbit correctors (for sextupole bumps), one can also find solutions for improving the optics, such as reducing the beta beating and the linear coupling, optimizing beta functions at the IP, bringing the working tune to near half integer, and improving dispersion. Furthermore, the updated virtual machine is stored online (the online model) for better subsequent online measurement. They are also fed to the program MAD to help lattice improvement and to the program LEGO for beam-beam simulations [7].

4.2.5.1 Beta Beat Fix

Shown in Figure 6 is the PEP-II HER β function on Nov. 22, 2005, which shows a high beta beat and was subsequently corrected through a solution from the MIA virtual model.

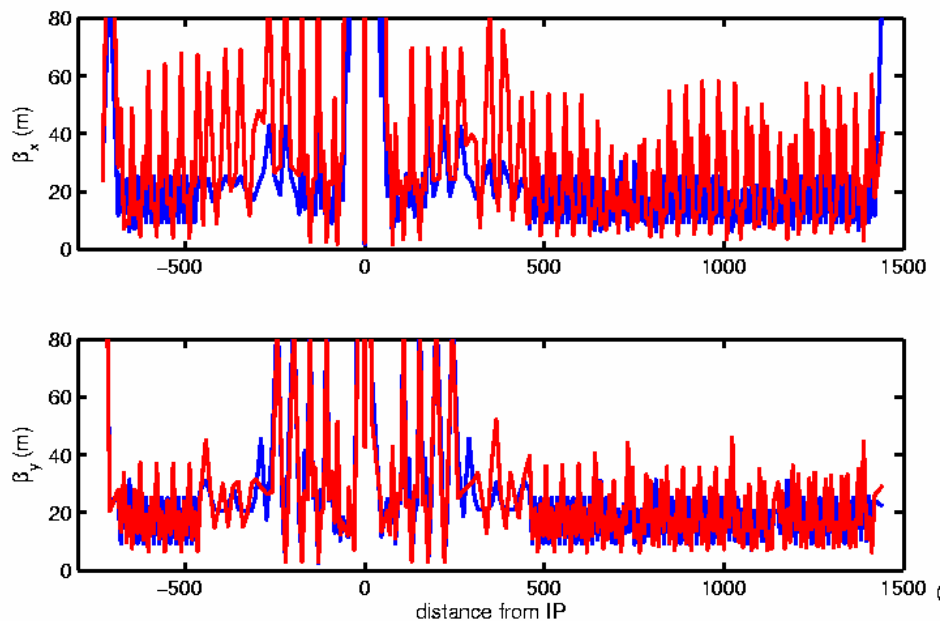


Figure 6: Comparison of PEP-II HER β functions on Nov. 22, 2005: the ideal lattice (blue color) and the virtual machine (red color). The PEP-II HER showed high beta beats which were subsequently corrected through solution from the virtual machine.

Shown in Figure 7 is the PEP-II HER β function on Mar. 16, 2006, which shows that the beta beat has been much improved. From the MIA virtual machine, we have been able to identify a key quadrupole (QF5L). This normal quadrupole along with the linear trombone quads and local and global skews are used as variables in the MIA program for finding the solution from the virtual machine. The solution is then translated into a control system knob for dialing into the PEP-II HER.

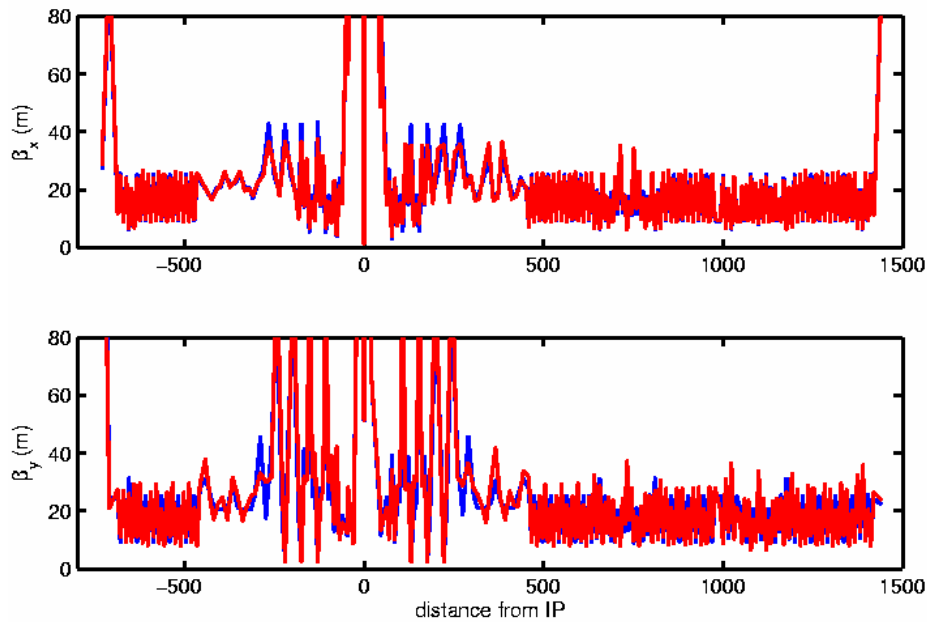


Figure 7: Comparison of PEP-II HER β functions on Mar. 16, 2006: the ideal lattice (blue color) and the virtual machine (red color). Beta beat shown in Fig. 5 has been much improved. This beta beat fix was done with a scheduled 1-shift MD.

4.2.5.2 Dispersion Beat Fix

As mentioned above, we have been able to include dispersion measurements in the virtual machine without adding new types of variables. Figure 8 compares dispersion calculated from the virtual machine and derived from the direct measurement of PEP-II HER on Nov. 22, 2005. There is no bending magnet or orbit corrector involved in the fitting for the virtual machine. The vertical dispersion beat was subsequently improved with the MIA virtual model.

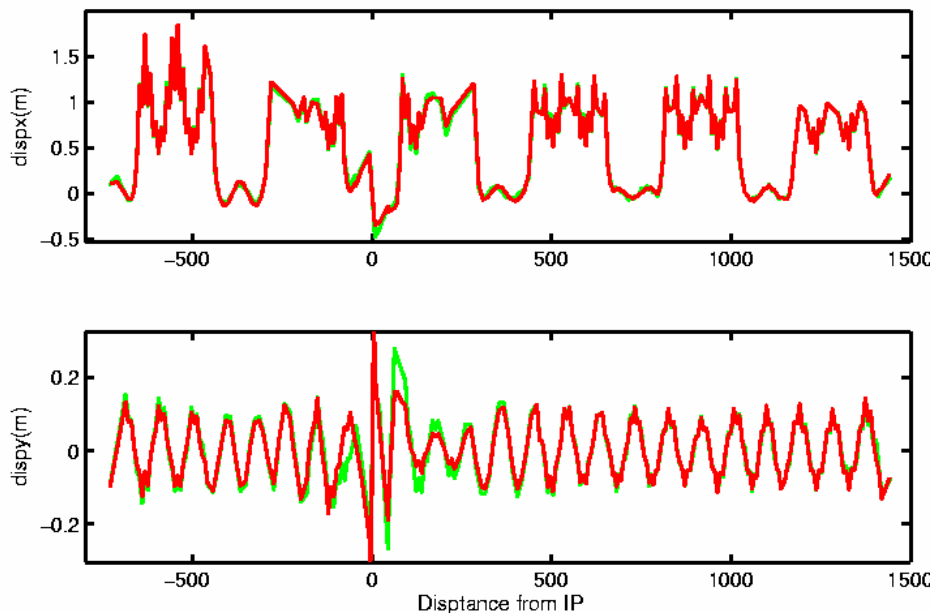


Figure 8: Comparison of PEP-II HER dispersion on Nov. 22, 2005: the direct measurement (green color) and the virtual machine. No bending magnet or orbit corrector was added as a variable for fitting. The vertical dispersion beats were subsequently fixed.

4.2.5.3 *Dramatic Change of Machine Working Tunes*

The MIA virtual machine has also been applied to PEP-II LER on April 29, 2003, bringing its working tune to near half integer, fixing its strong beta beat, and along with other efforts, subsequently boosting PEP-II luminosity by 50%.

4.2.5.4 *Optics Fix after Major Orbit Steering*

As another example, due to strong coupling in the IR, PEP-II LER major orbit steering is usually accompanied by a much degraded linear optics due to the change of sextupole feed-downs, which has been very difficult to correct. Indeed, without help from an accurate optics model, there have been many previous tries of LER major orbit steering which ended with back-out. With an accurate MIA virtual machine established for the LER (right after the major steering), we have been able to correct the linear optics such that the major LER orbit steering in April, 2006 was kept. Figure 9 shows the LER linear coupling characteristics after dialing in MIA solutions right after the major orbit steering. This PEP-II LER coupling is a record low with a record low residual from the ideal lattice.

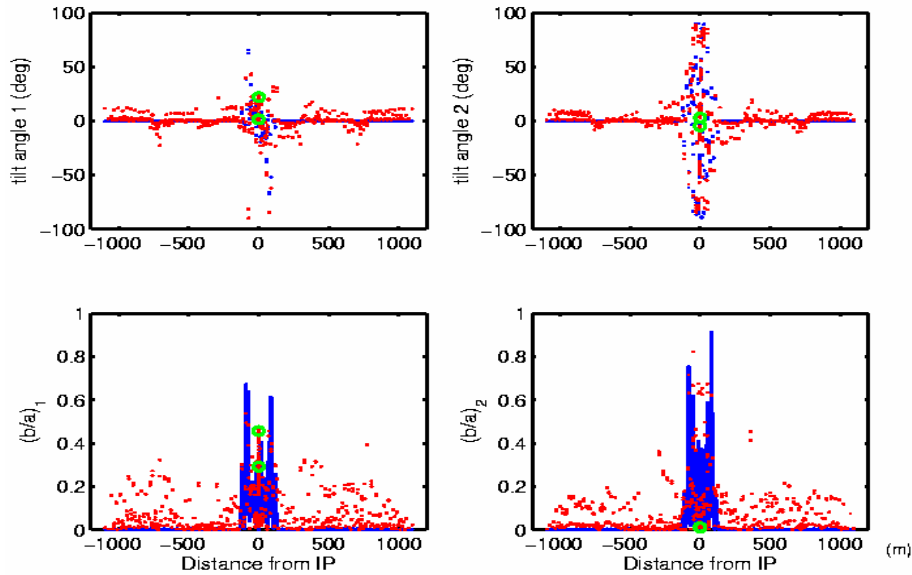


Figure 9: Comparison of PEP-II LER linear couplings on Apr. 21, 2006: the ideal lattice (blue color) and the virtual machine (red color). This was after a major orbit steering that was accompanied by a MIA solution for linear optics correction. Top plot shows the Eigen ellipse tilt angles while the bottom plot shows the Eigen ellipse axis ratios for Eigen plane 1 and 2 respectively

4.2.5.5 *Virtual Emittance and Virtual Luminosity*

The beta beat fix example shown in Figure 7 was achieved with a formal schedule of 1 shift of machine development (MD). Here we show another example without a formal MD schedule. That is, we tried to dial in the MIA solution knob to HER adiabatically during PEP-II collision. Figure 10 shows the strong beta beat from the MIA virtual machine of PEP-II HER on Feb 6, 2007. Based on this virtual machine, we found a solution that would significantly reduce the beta beat. We had the chance to adiabatically dial 50% of the solution into the real machine, HER, during collision. Subsequently, the beta beat was reduced by half as shown in Figure 11, while the emittance was improved as shown in Table 1. To make up the other 50% solution that was not dialed into the machine, we tried to get another solution, which we called the new half solution, from the updated virtual machine on Feb. 8, 2007 after 50% of the solution derived from the virtual machine of Feb. 6, 2007 was in. The beta beat is expected to be nicely fixed as shown in Figure 12, which shows the beta functions of the wanted model for the new half solution. The X emittance can also be nicely reduced to near the ideal lattice design of about 50 nm as shown on Table 1. However, before the machine changed (drifts) enough such that the new half solution was no longer suitable, we did not get a chance to dial in the new half solution in time. Therefore we do not know if this new half solution will indeed work as expected.

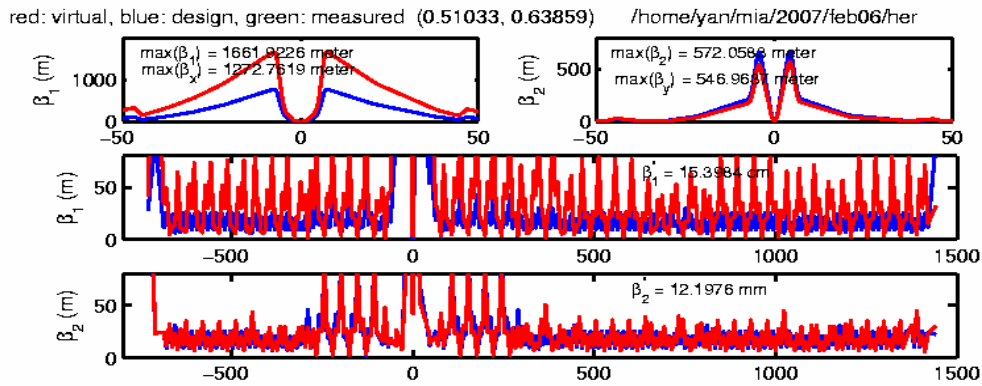


Figure 10: Comparison of PEP-II HER β function on Feb. 6, 2007: the ideal lattice (blue color) and the virtual machine (red).

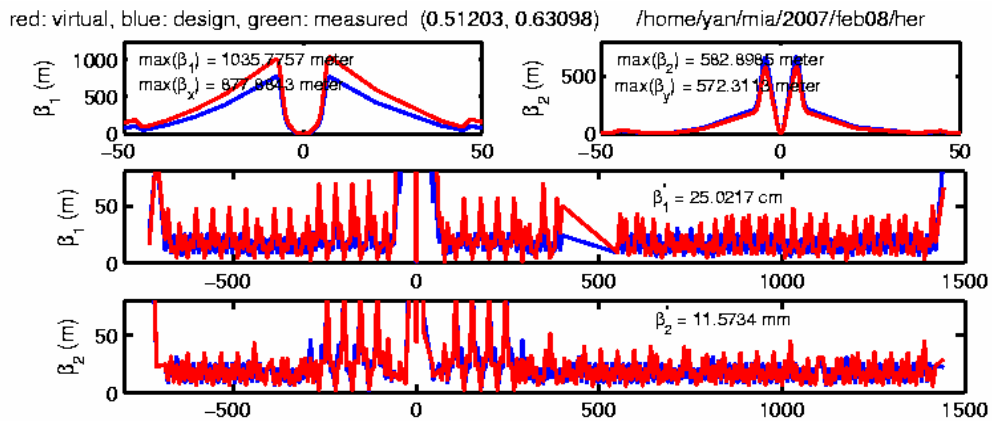


Figure 11: Comparison of PEP-II HER β function on Feb. 8, 2007 after dialling in 50% of the MIA solution knob derived from the virtual machine of Feb. 6, 2007: the ideal lattice (blue color) and the virtual machine (red).

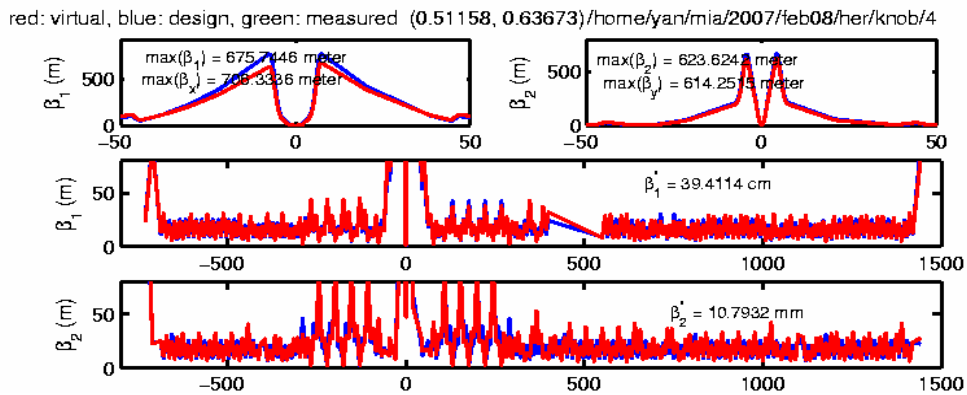


Figure 12: Comparison of PEP-II HER β function on Feb. 8, 2007: the ideal lattice (blue color) and the wanted model (red color) for the new half solution derived from the virtual machine of Feb. 8, 2007.

Table 1: Emittance comparison for PEP-II HER

<i>PEP-II HER</i>	<i>X emittance (nm)</i>	<i>Y emittance (nm)</i>
Virtual HER Feb. 6, 2007	94	0.59
Virtual HER Feb. 8, 2007 (after 50% MIA solution in)	64	0.24
Wanted model for the new half solution derived from Virtual HER Feb. 8, 2007 after 50% MIA solution	52	0.24
Ideal Lattice emittance calculated from MIA program	51	0.13

Since we can get the virtual machine if we extract the MIA BPM buffer data from the real machine, we can calculate in detail how the emittance is integrated through the circumference. In Figure 13, the top plot shows how the X emittance is integrated through the circumference while the bottom plot shows how the Y emittance is integrated through the circumference.

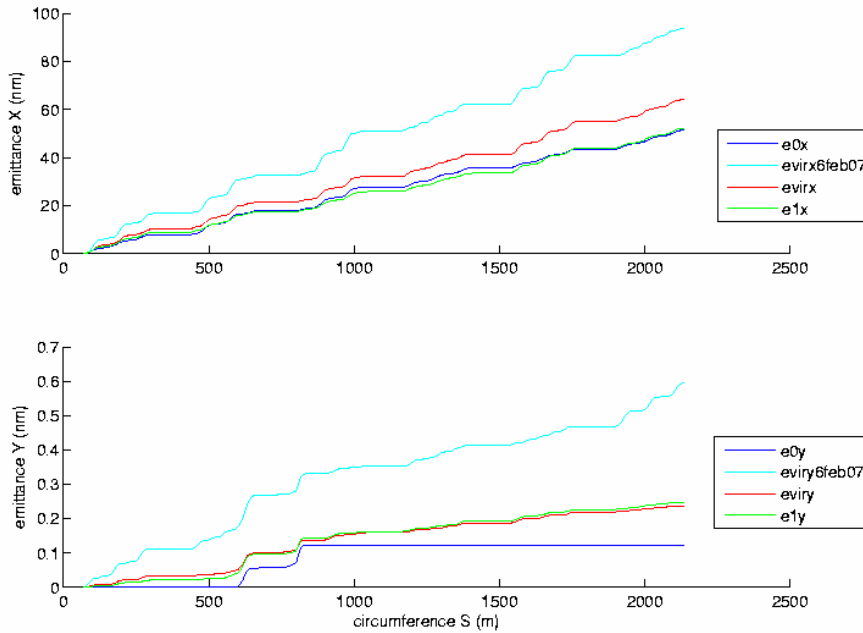


Figure 13: Comparison of PEP-II HER X emittance (top plot) and Y emittance (bottom plot) contribution through circumference for the virtual machine on Feb 6, 2007 (evirx6feb07, eviry6feb07), the virtual machine on Feb 8, 2007 (evirx, eviry), the wanted model for the new half solution derived from the virtual HER on Feb 8, 2007 (e1x, e1y), and the ideal lattice of HER (e0x, e0y).

It should also be noted that since we can calculate the emittance and the IP optics parameters from the virtual machines (HER and LER), we can calculate the virtual specific luminosity and the virtual luminosity of PEP-II given that we get both virtual LER and virtual HER.

4.2.6 Conclusions

We have used a model-independent analysis (MIA) for accurate orbit and phase advance measurement and then used an SVD-enhanced Least Square fitting for building accurate virtual models for PEP-II e+, e- storage rings. The MIA virtual machine matches very well the real-machine linear optics including dispersion. It has successfully improved PEP-II beta beats, linear couplings, half-integer working tunes, and dispersion. The success comes from:

- **Auto optimized selection of the Eigen modes for the SVD-enhanced Least-Square fitting:** The auto optimized SVD-enhanced Least-Square fitting can avoid degeneracy and has a fairly fast convergence rate allowing for application to a fairly large system.
- **PEP-II ring has a reasonable amount of good BPMs:** The PEP-II ring has a reasonable amount of good BPMs allowing for extraction of sufficient physical quantities for fitting.
- **Essentially unlimited Green's functions add to fitting convergence:** The linear Green's functions among BPMs can provide essentially unlimited fitting constraints that add significantly to convergence and accuracy.

4.2.7 Acknowledgement

The author would like to thank Y. Cai, A. Chao, W. Colocho, F-J. Decker, S. Ecklund, J. Irwin, S.Y. Lee, J. Seeman, M. Sullivan, J. Turner, C-x. Wang, U. Wienands, W. Wittmer, M. Woodley, and J. Yocky for their collaboration and many helpful discussions.

4.2.8 References

1. Y.T. Yan, Y. Cai, F-J. Decker, S. Ecklund, J. Irwin, J. Seeman, M. Sullivan, J. Turner, U. Wienands, "Virtual Accelerator for Accelerator Optics Improvement," SLAC-PuB-11209, in PAC2005 Proceedings (2005), MPPE058.
2. J. Irwin, C.X. Wang, Y.T. Yan, etc. "Model-Independent Beam-Dynamics Analysis", Phys. Rev. Lett., **82**, 1684 (1999).
3. J. Irwin, and Y.T. Yan, "Beamline model verification using model-independent analysis"
4. SLAC-PUB-8515 (2000), in EPAC2000 Conference Proceedings.
5. Y.T. Yan, Y. Cai, W. Colocho, F-J. Decker, to be presented in PAC2007.
6. Y.T. Yan and Y. Cai, "Precision measurement of coupling Eigen ellipses in a storage ring,"
7. SLAC-PUB-10371 (2006).
8. Y.T. Yan and Y. Cai, "Precision PEP-II optics measurement with an SVD-enhanced
9. Least-Square fitting," Nucl. Instrum. Meth. A555:336-339, 2006.
10. Y. Cai, et al., "Luminosity improvement at PEP-II based on optics model and beam-beam simulation," in EPAC2006 proceedings: MOPLS052.

5 Recent Doctorial Theses

5.1 Emittance Evolution Process in High Brightness Photo-Cathode RF Gun with Focusing Solenoids

Jangho Park, Pohang Accelerator Laboratory, POSTECH, Korea
eMail to: wpjho@postech.ac.kr

Name: Jangho Park

University: Pohang University of Science and Technology

Affiliation: Pohang Accelerator Laboratory

Thesis Title: Emittance Evolution Process in High Brightness Photo-Cathode RF Gun with Focusing Solenoids

Graduation Date: February 14, 2007

Supervisor: Prof. In Soo Ko

Abstract:

A BNL GUN-IV type photocathode rf gun has been fabricated to use in Femto-second Electron Diffraction (FED), femto-second Far Infra-red Radiation (fs-FIR) facility, and X-ray Free Electron Laser (X-FEL) at the Pohang Accelerator Laboratory (PAL). The gun consists of a 1.6-cell cavity with a copper cathode, solenoids for beam emittance compensation, beam diagnostic components for beam characteristics and auxiliary systems. The dimension of the cavity that provides desired resonant frequency is determined by the SUPERFISH code for 2D dimension determination. Change of the resonant frequency due to laser ports, a pumping port, and a waveguide port on the cavity wall was estimated with Slater's perturbation theorem. The dimensions of the waveguide port for the magnetic coupling from the klystron to the gun cavity are finalized by a series of the cutting and measuring processes. Basic beam parameters are measured to confirm the successful fabrication of the photocathode RF gun system. Basic diagnostics for the beam include the beam spot size, the beam charge, the beam energy, and the beam emittance. The best performance of the beam energy and the bunch charge of the photo-electron beam is measured as 3.7 MeV and 550 pC at the 30° laser injection phase, respectively. The rms beam spot size and the normalized rms transverse emittance of the beam are measured as 0.79 ± 0.042 mm and 1.72 ± 0.29 mm-mrad at 3.7 MeV beam energy with 300 pC beam charge at 30° laser injection phase, respectively. In addition to these results, measurements of the emittance evolution by the emittance meter are carried out. These experimental approaches in various beam conditions can lead proper experimental conditions for the PC RF gun commissioning using the fully emittance compensated beam. The experimental and the computational approaches of the emittance evolution and the compensation are introduced in this thesis.

5.2 Study on the Lattice and Beam Collective Effects of High Energy Electron Storage Ring

Yi-Peng Sun

Peking University, Beijing, China

Institute of High Energy Physics, CAS, Beijing, China

Mail to: sunyipeng_job@126.com

Supervisor: Prof. J. Gao, IHEP and Prof. Z.Y. Guo, Beijing University

5.2.1 Introduction

The high energy storage ring lattices play a dominant role in determining many important parameters of a storage ring, such as the luminosity, emittance, dynamic aperture, and so on. The beam instabilities caused by collective effects are the main limitations of the beam intensity and colliding luminosity in modern accelerators. Thus, the beam instabilities are also the research frontier of accelerator physics around the world. This doctoral thesis does study on the BEPCII lattice and the ILC damping ring lattice, also study on the beam collective effects.

5.2.2 On BEPCII Lattice

On the high energy storage ring lattices, based on beam-beam simulation results [1], the thesis studies all the possibilities on increasing the luminosity of BEPCII collision mode, say the working point, shorter natural bunch length, smaller vertical beta function at IP, the beam-beam parameter, etc, and gets several high luminosity collision mode; the thesis also does study on the optimization of BEPCII synchrotron radiation mode, to get a much more stable tune and transverse motion, and include some commissioning results of BEPCII SR mode.

In Table 1 the main parameters of the BEPCII collision mode are listed, where a comparison is made between the original BEPCII collision mode and the optimization results [2]. The luminosity of BEPCII collision mode can be increased from $0.5 \times 10^{33} \text{ cm}^{-2} \text{ s}^{-1}$ to $0.828 \times 10^{33} \text{ cm}^{-2} \text{ s}^{-1}$, **which is estimated by the simulation results**. The dynamic aperture (DA) [3] of the optimized modes is larger than $10\sigma_x \times 10\sigma_y$ and can fulfill the requirements for injection and running, shown in Fig. 1.

Table 1: Comparison between the original BEPCII collision mode and the optimization results.

<i>Parameter</i>	<i>Original</i>	<i>Mode 1</i>	<i>Mode 2</i>
Energy E (GeV)	1.89	1.89	1.89
Natural chromaticity x/y	-11/-21	-12/-21	-11/-25
Tune x/y	6.53/5.58	6.53/5.56	6.53/5.56
Emittance x (nm.rad)	144	144	142
Momentum compaction factor	0.0235	0.0187	0.0189
Bunch length (cm)	1.5	1.2	1.2
Beta-function at IP(x/y) (m)	1/0.015	1/0.015	1/0.012
Luminosity ($\text{cm}^{-2} \text{ s}^{-1}$)	0.5×10^{33}	0.77×10^{33}	0.828×10^{33}

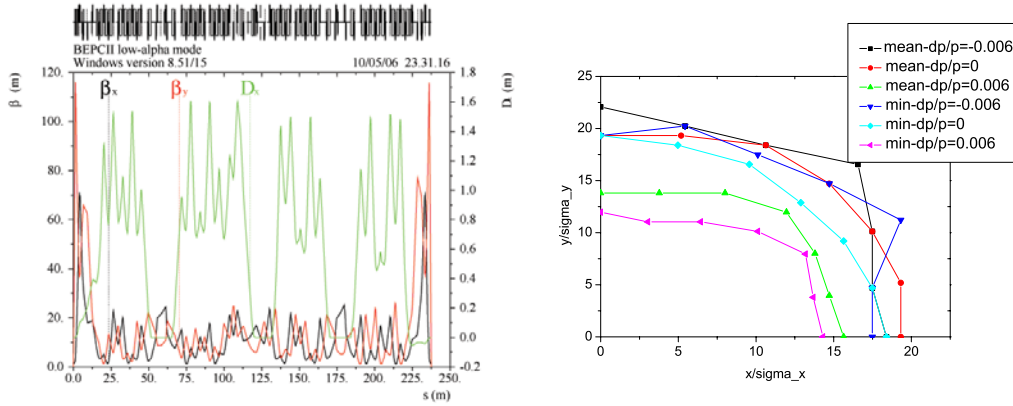


Figure 1: (Left): TWISS parameters of one optimized collision mode; (Right): DA.

FMA (Frequency Map Analysis) [4] is performed on the optimized BEPCII SR lattice where 2500 on-momentum particles are tracked for 2000 turns, and the result is shown in Fig. 2. From the optimized dynamic apertures of both on-momentum and off-momentum particles (with linear wiggler model and nonlinear wiggler model), and dynamic aperture of on-momentum particles with FMA, it can be seen that this new lattice is much better than the original lattice to be used for the commissioning and operation of BEPCII SR run.

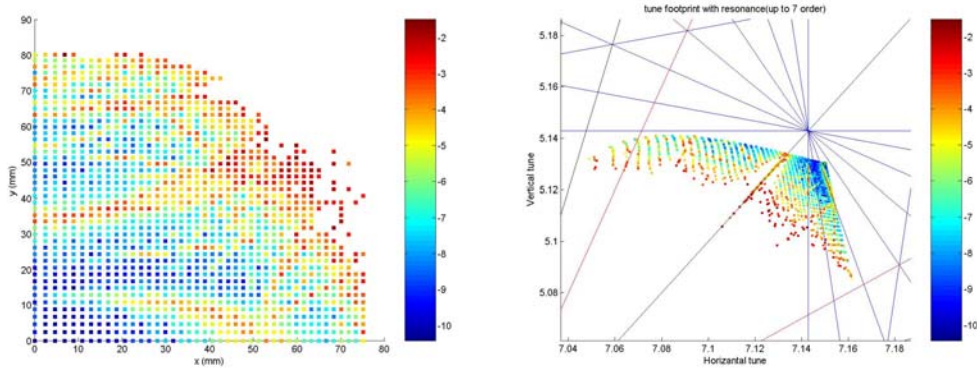


Figure 2: (Left): DA with FMA; (Right): Footprint on tune space.

5.2.3 On ILC Damping Ring Alternative Lattice

The thesis also studies on the International Linear Collider damping rings lattice with the aim to reduce the total cost. That includes the comparison between different kinds of arc cells, the simplification of the total lattice structure, decreasing the total magnets number, the design of the dispersion suppressor, and also the dynamic aperture optimization and tune choosing associated studies. From these studies, a full technique on designing and optimizing the large storage ring lattices is established.

To have proper momentum compaction, emittance, beta functions, and phase advance, the arc cell length, total arc cell number, and the drift's length in one arc cell are scanned [5]. At last, 72/72 degree modified FODO arc cell which is 29.4 m long is selected, and the total arc cell number is selected to be 184. The arc cell and dispersion suppressor design are shown in Fig. 3.

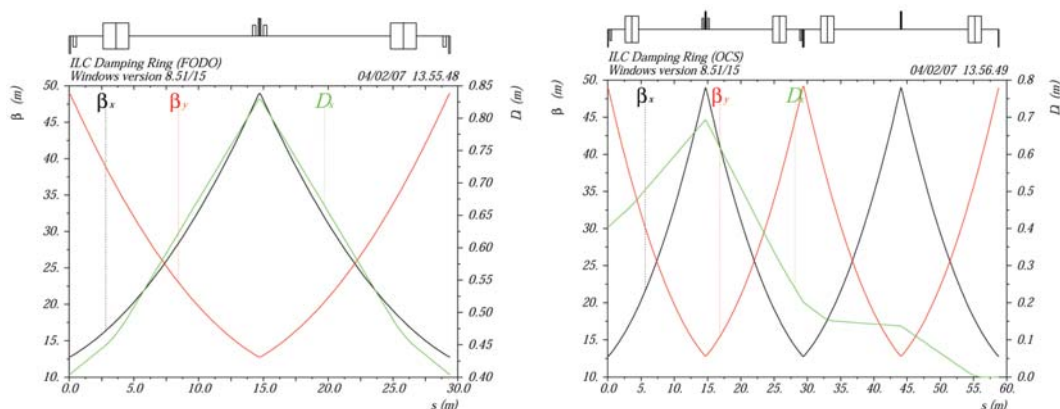


Figure 3: (Left): Arc cell design; (Right): Dispersion suppressor design.

After careful considerations of the matching sections between arc and straight, finally an ILC damping ring FODO lattice design is accomplished, with 2/3 number of quadrupoles, same total length of dipoles, less sextupoles, and a half number of cryogenics access shafts in comparison with OCS6 lattice (the baseline design). The layout and total ring TWISS parameters are shown in Fig. 4.

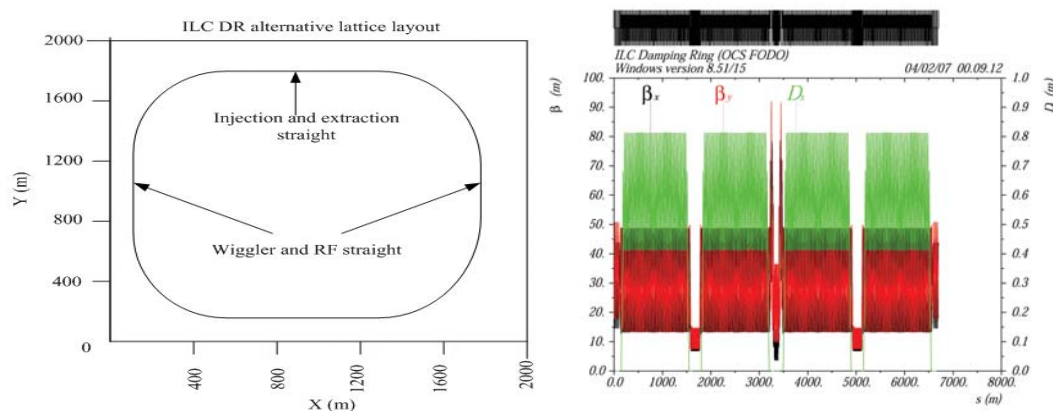


Figure 4: (Left): Layout; (Right): TWISS parameters of the damping ring.

Following some matching criteria and the requirements for selecting a proper working point, the linear lattice matching, chromaticity correction and FMA (Frequency Map Analysis) (dynamic aperture) tracking process are repeated. For $\alpha_p = 4 \times 10^{-4}$ case, the DA is about 7 times injected positron bunch size for on-momentum particles, without magnets errors and alignment errors. For $\alpha_p = 2 \times 10^{-4}$ case, the DA is about 3.5 times injected positron bunch size and under optimization.

The advantage of this design is that: with the whole lattice unchanged, by only adjusting the power supply of the quadrupoles, the momentum compaction of the FODO damping ring can be tuned between 2×10^{-4} and 6×10^{-4} ; accordingly the phase advance of one arc cell is tuned between 90/90 degree and 60/60 degree.

5.2.4 Beam Collective Effects

On the beam collective effects, first the thesis studies on the single bunch transverse instability of BEPC both theoretically and experimentally.

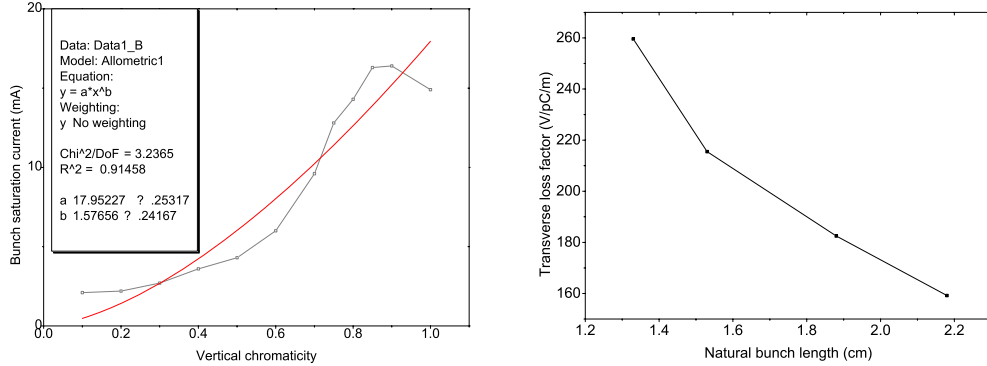


Figure 5: (Left): Fit of the experimental data; (Right): Transverse loss factor.

The experiments were made on the single bunch transverse instability threshold current versus the vertical chromaticity on BEPC. By analyzing the experimental data based on the transverse instability theory [6], the transverse loss factor of BEPC and the corresponding scaling law are obtained for the first time, as shown in Fig. 5. The corresponding scaling law for BEPC ring is found to be $I_{th} \propto \zeta_{c,y}^{*1.57}$, where I_{th} is the single bunch saturation current and $\zeta_{c,y}$ is the vertical chromaticity.

Also the thesis studies on the bunch lengthening effect both analytically and theoretically. A new macro-particle tracking code is developed to calculate the single bunch length and energy spread in storage rings using FORTRAN [7]. The bunch length and energy spread under different bunch current are calculated for BEPCII. Also the single bunch microwave instability threshold is predicted to be around 65 mA for BEPCII. The tracking result of this code is in good accordance with other codes. The simulated bunch length, energy spread, and bunch longitudinal distribution under different single bunch current are shown in Fig. 6.

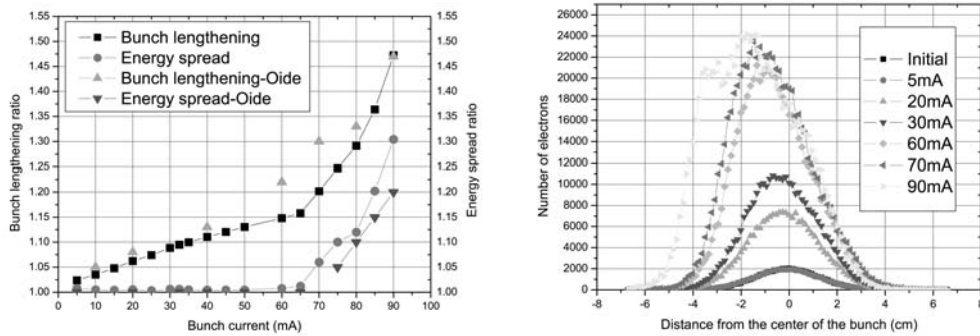


Figure 6: (Left): Bunch length and energy spread under different single bunch current (in comparison with other code’s results); (Right): Longitudinal distribution.

Theoretically, based on one existed bunch lengthening theory [8], through a series of deduction, a new bunch lengthening theory is established, where the wiggler's effect is taken into account. The associated bunch lengthening and energy spread widening are as follows:

$$R_z^2 = 1 + \frac{\sqrt{2\zeta} R_{av} \rho B K_{z,0}^{tot} I_b}{\gamma^{3.5} R_z^{1.21}} + \frac{(e C I_b \cdot B K_{z,0}^{tot})^2 \cdot f_0}{\vartheta \cdot \gamma^7 \cdot \left(\frac{1}{\rho^3} + \sum \frac{2I_{2,w}}{\pi \lambda_0 \rho_0} \right) \cdot R_z^{2.42}} \quad (1)$$

$$R_\varepsilon^2 = 1 + \frac{(e C I_b \cdot B K_{z,0}^{tot})^2 \cdot f_0}{\vartheta \cdot \gamma^7 \cdot \left(\frac{1}{\rho^3} + \sum \frac{2I_{2,w}}{\pi \lambda_0 \rho_0} \right) \cdot R_\varepsilon^{2.42}} \quad (2)$$

where $R_z = \sigma_z / \sigma_{z0}$, $R_\varepsilon = \sigma_\varepsilon / \sigma_{\varepsilon0}$, $\sigma_{\varepsilon0}$ is the natural energy spread, σ_{z0} is the natural bunch length, $K_z^{tot}(\sigma_z)$ is the longitudinal loss factor of the ring for one turn, I_b is the bunch current, R_{av} is the average radius of the ring, C is the circumference of the ring, ρ is the ring curvature, γ is the normalized electron energy, B is associated with the inductance of the ring, $I_{2,w}$ is the second radiation integral for wigglers.

The effectiveness of this formula is checked on the CESR ring and then applied on the International Linear Collider damping ring to predict the bunch lengthening (with natural bunch length as 9 mm). The results are shown in Fig. 7.

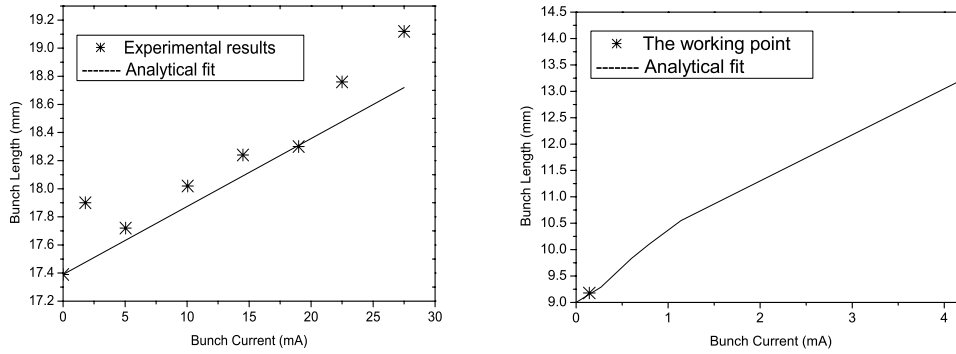


Figure 7: (Left): CESR storage ring with wigglers: the solid line is the analytical fit results; the star dots are the experimental results; (Right): ILC damping ring: The solid line is the analytical fit results ($\sigma_{z0}=9$ mm).

5.2.5 References

1. Yuan Zhang et al., "Simulation study of beam-beam effects", Phys. Rev. ST Accel. Beams 8, 074402 (2005).
2. H. Grote, and C. Iselin, The MAD Program, CERN/SL/90-13 (AP) (1990).
3. SAD manual, http://acc-physics.kek.jp/SAD/example/design_example.HTML.
4. S. Dumas, J. Laskar, "Global dynamics and long-time stability in Hamiltonian systems via numerical frequency analysis", Phys. Rev. Lett. 70, 2975 (1993).

5. A. W. Chao, M. Tigner, Handbook of Accelerator Physics and Engineering, World Scientific, p. 60 (1998).
6. J. Gao, "Theory of single bunch transverse collective instabilities in electron storage rings", Nucl. Instr. And Methods A 416, p. 186 (1998).
7. A. Renieri, LNF-76/11(R), Frascati (1976).
8. J. Gao, "Bunch lengthening and energy spread increasing in electron storage rings", Nucl. Instr. And Meth.

6 Forthcoming Beam Dynamics Events

6.1 International Europhysics Conference on High Energy Physics (HEP 2007)

C. Biscari, LNF – INFN, Frascati, Italia

H. Burkhardt, CERN, Switzerland

Mail to: caterina.biscari@lnf.infn.it, Helmut.Burkhardt@cern.ch

The International Europhysics Conference on High Energy Physics (HEP 2007) (<http://www.hep.man.ac.uk/HEP2007/>) will take place in Manchester from 19-25 July 2007.

The conference is organised by the High Energy and Particle Physics Division of the European Physical Society (EPS). The two most recent conferences in the series were held in Aachen and Lisboa in 2003 and 2005, respectively.

HEP 2007 will consist of plenary, parallel and poster sessions. In this connection, the Interdivisional Group on Accelerators of the EPS (EPS-IGA) has been invited to collaborate with the HEP 2007 Programme Committee in the organization of two parallel sessions on Accelerator Research and Development and Technology.

In the context of a high energy physics conference, this session is thus aimed at our colleagues working in the field of particle physics, in particular the younger ones, to inform them about the physics and technology challenges in the accelerator field, and to stimulate interest in working more closely with colleagues in our field. Presentations should be more pedagogical talks than reviews. They are not aimed at accelerator physicists or engineers and should present a selection of the most exciting and challenging topics in the accelerator field in a form matched to this particular audience keeping in mind that less is more.

This is a unique but challenging opportunity for us accelerator physicists to interest our peers in particle physics but also to continue our dialogue with this community to understand its needs and motivation.

Abstracts for oral presentations or posters can be sent directly through the above mentioned conference web site. Since the deadline is already very near, you can also send your abstracts directly to our email addresses, and we will convey them into the parallel or poster sessions.

Caterina Biscari

Convenor, Accelerator Session of HEP 2007
Chairman EPS Interdivisional Group for Accelerators
(caterina.biscari@lnf.infn.it)

Helmut Burkhardt

Convenor, Accelerator Session of HEP 2007
Member of Organizing Committee of HEP 2007
(Helmut.Burkhardt@cern.ch)

6.2 LARP Mini-Workshop on Beam-Beam Compensation 2007

Date: July 2-4, 2007

Place: SLAC

Website: www-conf.slac.stanford.edu/larp/

The US LHC Accelerator Research Program (LARP) hosts a mini-workshop on beam-beam compensation at SLAC. The workshop will review the experience with beam-beam compensation tests, both long-range and head-on, in existing machines (DCI, SPS, Tevatron, DAΦNE, KEKB, RHIC), and outline milestones for the implementation of beam-beam compensation schemes in the LHC. It is also intended to be a platform for young scientists to present their work. The workshop is by invitation only.

Program Committee

O. Brüning (CERN)
 Y. Cai (SLAC)
 A. Chao (SLAC)
 W. Fischer (BNL, chair)
 M. Furman (LBNL)
 J.-P. Koutchouk (CERN)
 T. Sen (FNAL)
 V. Shiltsev (FNAL),
 F. Zimmerman (CERN)

Local Organizing Committee (SLAC)

M. Bengali
 Y. Cai
 A. Chao
 T. Knight
 R. McDunn
 J. Valine
 S. West

6.3 Low Level Radio Frequency Workshop (LLRF 2007)

Mark Champion

Mail to: champion@fnal.gov

Fermi National Accelerator Laboratory
 PO Box 500, Batavia, IL 60510 USA

6.3.1 Announcement

This four-day workshop will be the third in a series of LLRF workshops; the first was held at Thomas Jefferson National Accelerator Facility in 2001 and the second was held at CERN in 2005. This will be the 16th in the series of mini-workshops conducted under the auspices of the ICFA Beam Dynamics Panel. The goals of the LLRF07 Workshop are to bring together people working on LLRF control systems worldwide to share our experiences, to present the status of our work, to discuss recent technical developments, and to seek solutions to technical problems.

The workshop will include invited and contributed talks, a poster session, and working group sessions. The LLRF07 web site is under development and will soon be available at: <http://www.sns.gov/workshops/llrf2007/>.

Registration opens May 1, 2007. Please register early to ensure a place in the workshop, which is limited to approximately 100 people.

7 Announcements of the Beam Dynamics Panel

7.1 ICFA Beam Dynamics Newsletter

7.1.1 Aim of the Newsletter

The ICFA Beam Dynamics Newsletter is intended as a channel for describing unsolved problems and highlighting important ongoing works, and not as a substitute for journal articles and conference proceedings that usually describe completed work. It is published by the ICFA Beam Dynamics Panel, one of whose missions is to encourage international collaboration in beam dynamics.

Normally it is published every April, August and December. The deadlines are 15 March, 15 July and 15 November, respectively.

7.1.2 Categories of Articles

The categories of articles in the newsletter are the following:

1. Announcements from the panel.
2. Reports of beam dynamics activity of a group.
3. Reports on workshops, meetings and other events related to beam dynamics.
4. Announcements of future beam dynamics-related international workshops and meetings.
5. Those who want to use newsletter to announce their workshops are welcome to do so. Articles should typically fit within half a page and include descriptions of the subject, date, place, Web site and other contact information.
6. Review of beam dynamics problems: This is a place to bring attention to unsolved problems and should not be used to report completed work. Clear and short highlights on the problem are encouraged.
7. Letters to the editor: a forum open to everyone. Anybody can express his/her opinion on the beam dynamics and related activities, by sending it to one of the editors. The editors reserve the right to reject contributions they judge to be inappropriate, although they have rarely had cause to do so.

The editors may request an article following a recommendation by panel members. However anyone who wishes to submit an article is strongly encouraged to contact any Beam Dynamics Panel member before starting to write.

7.1.3 How to Prepare a Manuscript

Before starting to write, authors should download the template in Microsoft Word format from the Beam Dynamics Panel web site:

<http://www-bd.fnal.gov/icfabd/news.html>

It will be much easier to guarantee acceptance of the article if the template is used and the instructions included in it are respected. The template and instructions are expected to evolve with time so please make sure always to use the latest versions.

The final Microsoft Word file should be sent to one of the editors, preferably the issue editor, by email.

The editors regret that LaTeX files can no longer be accepted: a majority of contributors now prefer Word and we simply do not have the resources to make the conversions that would be needed. Contributions received in LaTeX will now be returned to the authors for re-formatting.

In cases where an article is composed entirely of straightforward prose (no equations, figures, tables, special symbols, etc.) contributions received in the form of plain text files may be accepted at the discretion of the issue editor.

Each article should include the title, authors' names, affiliations and e-mail addresses.

7.1.4 Distribution

A complete archive of issues of this newsletter from 1995 to the latest issue is available at

<http://icfa-usa.jlab.org/archive/newsletter.shtml>.

This is now intended as the primary method of distribution of the newsletter.

Readers are encouraged to sign-up for electronic mailing list to ensure that they will hear immediately when a new issue is published.

The Panel's Web site provides access to the Newsletters, information about future and past workshops, and other information useful to accelerator physicists. There are links to pages of information of local interest for each of the three ICFA areas.

Printed copies of the ICFA Beam Dynamics Newsletters are also distributed (generally some time after the Web edition appears) through the following distributors:

Weiren Chou	chou@fnal.gov	North and South Americas
Rainer Wanzenberg	rainer.wanzenberg@desy.de	Europe ⁺⁺ and Africa
Susumu Kamada	Susumu.Kamada@kek.jp	Asia ^{**} and Pacific

⁺⁺ Including former Soviet Union.

^{**} For Mainland China, Jiu-Qing Wang (wangjq@mail.ihep.ac.cn) takes care of the distribution with Ms. Su Ping, Secretariat of PASC, P.O. Box 918, Beijing 100039, China.

To keep costs down (remember that the Panel has no budget of its own) readers are encouraged to use the Web as much as possible. In particular, if you receive a paper copy that you no longer require, please inform the appropriate distributor.

7.1.5 Regular Correspondents

The Beam Dynamics Newsletter particularly encourages contributions from smaller institutions and countries where the accelerator physics community is small. Since it is

impossible for the editors and panel members to survey all beam dynamics activity worldwide, we have some Regular Correspondents. They are expected to find interesting activities and appropriate persons to report them and/or report them by themselves. We hope that we will have a “compact and complete” list covering all over the world eventually. The present Regular Correspondents are as follows:

Liu Lin	Liu@ns.inls.br	LNLS Brazil
Sameen Ahmed Khan	Rohelakan@yahoo.com	SCOT, Middle East and Africa

We are calling for more volunteers as Regular Correspondents.

7.2 ICFA Beam Dynamics Panel Members

Name	eMail	Institution
Caterina Biscari	caterina.biscari@lnf.infn.it	LNF-INFN, Via E. Fermi 40, C.P. 13, Frascati, Italy
Yunhai Cai	yunhai@slac.stanford.edu	SLAC, 2575 Sand Hill Road, MS 26 Menlo Park, CA 94025, U.S.A.
Swapan Chattopadhyay	swapan@jlab.org	Jefferson Lab, 12000 Jefferson Avenue, Newport News, VA 23606, U.S.A.
Weiren Chou (Chair)	chou@fnal.gov	Fermilab, MS 220, P.O. Box 500, Batavia, IL 60510, U.S.A.
Yoshihiro Funakoshi	yoshihiro.funakoshi@kek.jp	KEK, 1-1 Oho, Tsukuba-shi, Ibaraki-ken, 305-0801, Japan
Miguel Furman	mafurman@lbl.gov	Center for Beam Physics, LBL, Building 71, R0259, 1 Cyclotron Road, Berkeley, CA 94720-8211, U.S.A.
Jie Gao	gaoj@ihep.ac.cn	Institute for High Energy Physics, P.O. Box 918, Beijing 100039, China
Ajay Ghodke	ghodke@cat.ernet.in	RRCAT, ADL Bldg. Indore, Madhya Pradesh, India 452 013
Ingo Hofmann	i.hofmann@gsi.de	High Current Beam Physics, GSI Darmstadt, Planckstr. 1, 64291 Darmstadt, Germany
Sergei Ivanov	ivanov_s@mx.ihep.su	Institute for High Energy Physics, Protvino, Moscow Region, 142281 Russia
Kwang-Je Kim	kwangje@aps.anl.gov	Argonne Nat'l Lab, Advanced Photon Source, 9700 S. Cass Avenue, Bldg 401/C4265, Argonne, IL 60439, U.S.A.
In Soo Ko	isko@postech.ac.kr	Pohang Accelerator Lab, San 31, Hyoja- Dong, Pohang 790-784, South Korea
Alessandra Lombardi	Alessandra.Lombardi@cern.ch	CERN, CH-1211, Geneva 23, Switzerland
Yoshiharu Mori	mori@kl.rri.kyoto-u.ac.jp	Research Reactor Inst., Kyoto Univ. Kumatori, Osaka, 590-0494, Japan
Chris Prior	c.r.prior@rl.ac.uk	ASTeC Intense Beams Group, Rutherford Appleton Lab, Chilton, Didcot, Oxon OX11 0QX, U.K.
David Rice	dhr1@cornell.edu	Cornell Univ., 271 Wilson Laboratory, Ithaca, NY 14853-8001, U.S.A.
Yuri Shatunov	Yu.M.Shatunov@inp.nsk.su	Acad. Lavrentiev, prospect 11, 630090 Novosibirsk, Russia
Junji Urakawa	junji.urakawa@kek.jp	KEK, 1-1 Oho, Tsukuba-shi, Ibaraki-ken, 305-0801, Japan
Jiu-Qing Wang	wangjq@mail.ihep.av.cn	Institute for High Energy Physics, P.O. Box 918, 9-1, Beijing 100039, China
Rainer Wanzenberg	rainer.wanzenberg@desy.de	DESY, Notkestrasse 85, 22603 Hamburg, Germany
Jie Wei	wei1@bnl.gov	BNL, Bldg. 911, Upton, NY 11973- 5000, U.S.A.

*The views expressed in this newsletter do not necessarily coincide with those of the editors.
The individual authors are responsible for their text.*